NORTHWESTERN UNIVERSITY

Processing and Characterization of Porous Ti-6Al-4V and NiTi

A DISSERTATION

SUBMITTED TO THE GRADUATE SCHOOL
IN PARTIAL FULFILLMENT OF THE REQUIREMENTS

for the degree

DOCTOR OF PHILOSOPHY

Field of Materials Science and Engineering

By

Scott Oppenheimer

EVANSTON, ILLINOIS

June 2007

ABSTRACT

Processing and Characterization of Porous Ti-6Al-4V and NiTi

Scott Oppenheimer

A series of investigations was undertaken to explore the processing and properties of porous titanium with 6 wt% Al and 4 wt% vanadium (Ti-6Al-4V) and an equiatomic nickel-titanium alloy (NiTi). In this study, porous materials were created in the solid state by entrapping argon in a powder compact, and subsequently expanding the entrapped gas through creep of the matrix.

The gas quantity entrapped was varied by altering the pressure of argon in the powder prior to compaction, which led to initial porosities between 0.2% and 5%. Isothermal creep expansion of both the Ti-6Al-4V and the NiTi was examined in relation to the initial gas quantity. It was found that the higher the initial porosity the faster the porosity increase. In Ti-6Al-4V, the effect of transformation superplasticity (induced by thermal cycling) on pore expansion kinetics was explored, and found to significantly increase the pore growth rate. Thermal cycling was also used in NiTi to produce graded porosity using the non-linear response of creep to temperature.

The porous metals created through the above method were characterized in a number of ways. The pore size distribution of the Ti-6Al-4V porous material was measured using imaging methods. The elastic response of all the samples was determined using ultrasonic testing. Transformation properties of porous superelastic NiTi under stress were examined using synchrotron x-ray analysis.

The growth of porosity was explored through simulation using numerical as well as analytical methods. An existing analytical method was modified to include corrections to the gas law, initial porosity changes due to argon density, and a surface tension pressure.

Acknowledgements

I would first and foremost like to thank my adviser Dr. David Dunand. In such a short space as this I can say but a small amount of gratitude I feel. As a role model for the modern scientist I could not have asked for better, David combines great eloquence with astounding intelligence, and a strong sense of personal integrity. I have been honored to have spent the last 5 years learning from him as well as working with him. The time spent in discussions, the advice, and kindness will always be remembered.

I would like to thank my committee members, Dr. Brinson, Dr. Faber, and Dr. Olson. Their comments, suggestions and corrections throughout my time here have made this into a work I am proud of.

I would like to thank Christian Greiner for his friendship and the amazing work he accomplished here at Northwestern, I have used his master's thesis more than any other reference document.

I would like to thank all of the collaborators on the foam project, in specific Tim Sargeant, Huanlong Li, Hui Shen, and John O'Dwyer. It is wonderful to work with such people and see a project such as this move forward on so many fronts.

I would like to thank the great undergraduate students who have helped with this work. Andrea Jung and Jordan Kwok were both great people who I was lucky to work with.

I would like to thank all of the people that made the research itself possible. Dr. Stair, Mark Sinew, Ben Myers, Jeff Sundwell, and Thang all made the work that was done here much easier than it should have rightfully been.

I would like to thank all of the Dunand group members past and present. In specific the 1021 fact checking team of Alan Brothers, and John DeFouw deserves extra thanks, without the two of you I would never have made it through classes, much less research.

I would like to thank all the other friends I have made here at Northwestern. I doubt I will ever again have the chance for either the lofty scientific discussions, or the odd random conversations of our lunches.

I would like to thank all of the staff here in Mat. Sci. I could never have ordered supplies, used the copy machine, run the paperwork gauntlet, or graduated without all of your help. I will miss the friendly atmosphere, and all of your kindness.

I would like to thank all of the teachers who have helped me along the way. Special thanks to Beth Modic, Robert Pompii, and Eric Cotts.

I would like to thank my parents for giving me the tools, and encouragement to archive this.

I would like to thank Diane Chin, who made all of this worth doing.

Finally I wish to thank the US National Science Foundation who funded this research through Grant DMR-0505772, and the U.S. Department of Defense for a NDSEG Fellowship.

Contents

List of Figures

List of Tables

CHAPTER 1

Introduction

Porous metals can be thought of as composites where the second phase (vacuum or gas) has zero strength. Depending on the foam architecture, the porosity can be closed or open to the surface, and interconnected or non-percolating. A subset of this group are cellular metals, consisting of struts connected at nodes, whereas porous metals can also consist of pores in a matrix. A second subset of porous metals with greater than 50% porosity is often called metallic foams, but for the purpose of this document the term foam will be used synonymously with porous metal. Metallic foams, which are light and yet strong, occupy an important niche in the material properties spectrum [**1**, **2**], and have been used in the aerospace sector for non-critical structural elements, such as floor boards [**3**, **4**]. In ground-based applications, they have been used, like their polymer cousins, as impact absorbers due to their large energy dissipation during crushing. In non-structural applications, their high surface area can be used for catalytic substrates or as heat exchangers [**5**]. Other possible uses include electromagnetic shielding, filtration, and as fluid distribution and control [**6**]. In each of these situations, a number of different specific material properties are needed from the foams themselves. Since many of their mechanical properties are dictated by their porosity, these materials can be tailored by design to fit any number of applications.

The drawback for these materials is often their expense, which limits them to specialized uses. The aerospace industry is a prime example because any material that can reduce weight will give higher performance, reducing fuel costs, thus reducing total costs in the long run. Another high-value area of application for metallic foams is in medicine, in specific for bone replacement. In this application, the cost of the implant is dwarfed by the surgery costs, so even a small improvement is economically viable. A porous metal prosthesis can be made to match the stiffness of bone through the inclusion of porosity, allowing for less stress shielding of the bone [**7**]. Increased stress on the bone helps implant longevity because bone that is not stressed tends to be adsorbed back into the body, causing a loosening of the implant. Surface texturing currently allows some bone ingrowth into the implant, but foams have the benefit of allowing for complete bone growth throughout the prosthesis, leading to improved attachment. With all of these benefits, there is significant push to see such third generation fully porous implants made available [**8**–**11**].

For many of the applications listed above, there are specific requirements that favor one metal over another. Aluminum foams are the most common due to their relative ease of manufacture, and therefore, highly competitive price [**12**]. While less expensive, Al foams are not particularly strong, and poor in any high temperature environment. To push the envelope of strength and density, titanium foams have been an area of high interest [**13**]. Titanium is strong for its density, and further reducing the density by foaming can lead to very lightweight, yet strong materials. In specific applications such as in the medical field, titanium has further proven itself as fully biocompatible [**8**–**10**]. Research has also found other interesting metals that could be improved through foaming. For example, near equiatomic nickel-titanium alloys (NiTi in the following) have been used for medical applications due to their excellent biocompatibility [**14**, **15**] as well as their ability to exhibit a superelastic, or shape memory response [**16**–**18**].

In this thesis, I present my work on the foaming of titanium and nickel titanium. In the background (chapter 2), general information on previous titanium and nickel-titanium foaming is discussed, as well as superplasticity and superelasticity. The specific methods and equipment used in the data collection for this thesis are put forth in the experimental procedures, chapter 3. The results of the tests are given and discussed in chapter 4, which is broken into two sections; one on titanium (subsection 4.1) and the other on nickel-titanium (subsection 4.2). Simulations of the various foaming process are found in chapter 5. Future research avenues that are pointed to through the work done here are found in 7. Lastly computer code used in simulations, can be found in the appendix .

CHAPTER 2

Background

2.1. Foam Processing

2.1.1. Titanium Foams

Titanium is difficult to process due to both its high melting point (1670°C) and its affinity for oxygen, nitrogen, carbon and other contaminents. Many of the standard methods for foaming other metals such as gas injection, adding a foaming agent to a melt, deposition and burnout, and casting methods lead to impurities in the titanium that cause significant weakening and embrittlement [**19**, **20**]. For this reason lower temperature solid state methods are preferred.

Sintering of titanium has been used in a number of studies with standard powders [**21**], spherical powders [**22**], cold pressed pre-forms [**23**], spark-plasma assisted sintering [**10**], and hollow sphere sintering [**24**]. These methods created porous structures with between 5% porosity for long sintering with standard powders to up to 73% porosity for short sintering times with hollow spheres. All of these methods have the drawback of creating small necks between powders which serve as stress concentrations and crack initiation sites, leading to reduced strength [**9**].

2.1.2. Nickel Titanium Foams

Equiatomic nickel titanium (NiTi) has many of the same contamination problems as stated above for titanium; in the case of NiTi there is slightly less affinity for oxygen which is helpful [**25**], but the mechanical properties are very composition sensitive [**26**]. Sintering does not work as well in NiTi as in Ti, since the NiTi powders do not dissolve their own oxide layer as completely, requiring longer sintering times at higher temperatures [**27**]. Another way to create a porous NiTi body is to use SHS (Self-propagating High-temperature Synthesis) [**28–31**], in which elemental nickel and titanium powders are mixed and reacted at high temperature. The reaction to form the intermetallic NiTi is exothermic and the reaction front moves through the powder, heating, converting and sintering in one step. While fast, there is little control over this method, resulting in unwanted off-stoichiometry phases, and poor performance without long high temperature solutionizing.

2.1.3. Pressurized Pores

A process was developed by Kearns et al. [**32, 33**] in which powders are placed in a steel can that is backfilled with argon and sealed. This can is then densified in a hot isostatic press (HIP) at high temperature and pressure. Kearns used Ti-6Al-4V backfilled with 8 to 380 torr (1.0 to $50 \cdot 10^3$ Pa) of argon. Under HIP conditions, the gas volume is dramatically decreased and forced into small isolated pores due to the densifying titanium matrix (greater than 99% of bulk Ti-6Al-4V density). When removed from the HIP, the powder particles have formed a continous Ti matrix with small, isolated, high-pressure argon pores. After removing the steel can, the titanium material can be exposed to high

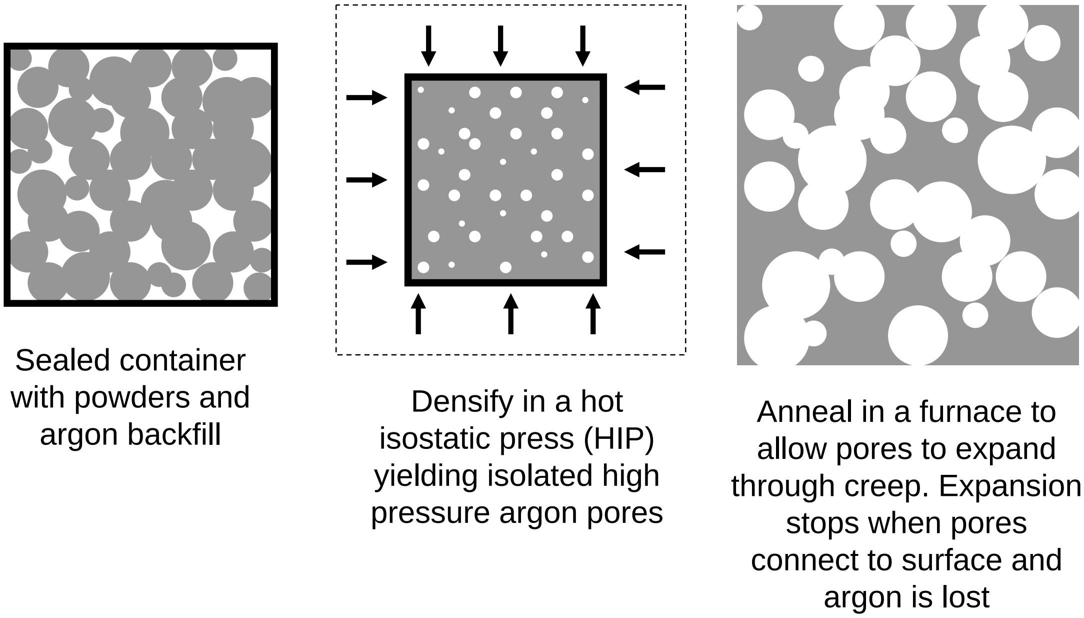

Figure 2.1. Pressurized pore foaming process.

temperature at low pressure to allow the growth of pores. A schematic diagram of this method can be seen in figure 2.1. During exposure, the pores expand by creep deformation of the matrix. With this method, Kearns was able to achieve porosities as high as 40% in Ti-6Al-4V after 50 hours at 1240 ^{o}C.

Queheillalt et al. [**34**] then modified the original Kearns process to create an in situ sandwich structure. In this version, the powders are placed inside a titanium can of the correct size and shape (in their case flat boxes to create panels). By HIP'ing and expanding with the Ti-6Al-4V can still attached, they created a sandwich structure with solid faces and a porous internal structure. The face sheets were thinned by hot rolling prior to expansion. The final structure after foaming had an internal core porosity of 23% and an overall porosity of 19%.

Murray and coworkers [**35**–**40**] expanded this process to commercial purity titanium. They also applied transformation superplasticity (discussed in section 2.2) to achieve similar total porosity to Kearns, but in less than 10% of the total time (5 hrs), and at a much reduced temperature (thermal cycling between 830^{o}C and 980^{o}C). Murray and Dunand also examined the effects of different powder sizes on foaming kinetics and microstructure [**40**]. Different initial porosities ranging from 0.06% up to 2.7% were produced by using differently sieved powders (30μm to 400μm).

A similar process has also been applied to NiTi production, where Lagoudas and Vandygrief [**41**] were able to achieve 50% porosity. This method is not directly comparable, as the can is not closed in the HIP. Rather, sintering of elemental nickel and titanium powders in a high pressure argon atmosphere (200 MPa) entraps the gas. When the pressure is released (while maintaining temperature), the structure expands. Mechanical testing of this material showed that, while it was porous, it had only mediocre superelastic properties, implying that this specific study had contamination issues (contamination in the argon, as well as 99% pure elemental powders).

2.2. Transformation Superplasticity

Superplasticity is the ability of a material to withstand tensile strains above 100% without fracture. Small grain size, pure diffusional creep, or superposition of stress states can all lead to superplasticity. Transformation superplasticity is the specific case where internal phase changes in a material cause a stress (through different phase volumes). This sets up internal stresses in the material that can be biased through applied stresses (in our case pressurized pores). Greenwood and Johnson first described this effect in 1965, when they noticed that the uniaxial strains per cycle for the allotropic metals Fe, Co, Ti, U and Zr are directly proportional to the uniaxial applied stress (corresponding to a stress exponent of 1 under thermally cycling conditions) [**42**]. In specific they found that:

$$\epsilon \approx \frac{5\sigma_z}{6Y}\left(\frac{\Delta V}{V}\right) \tag{2.1}$$

where ϵ is the uniaxial strain per phase change, σ_z is the applied uniaxial biasing stress, ΔV/V is the phase change volume, and Y is the yield strength of the weaker phase. On each phase change (both heating and cooling), strain is accumulated, so for a full cycle 2ϵ is gained. This cyclic phase change can proceed by temperature cycling as suggested by Greenwood and Johnson, by pressure cycling [**43**] or by composition cycling [**44, 45**]. Figure 2.2 shows a schematic for transformation superplasticity.

This effect has been noted in a number of metals and ceramics [**46**]; most important to this study is titanium. Commercial purity titanium has an allotropic phase change at 882^{o}C (hcp to bcc) with a corresponding change in volume of 0.48% [**47**]. Transformation superplasticity has been used to vastly speed up foaming in titanium [**35**]. Ti-6Al-4V also has the same phase change, but it takes place over the range 820-990^{o}C, and is kinetically controlled by diffusion. This kinetic control puts an upper limit on the speed at which one can cycle the material and still get the full transformation superplasticity (due to ΔV being proportional to transformation extent). Figure 2.3 shows work by Szkliniarz and Smolka [**48**] where the effect of heating rate on phase transformation was studied. These data were used along with further experiments and theory by Schuh and coworkers [**49–51**] to predict the superplastic creep rates of Ti-6Al-4V.

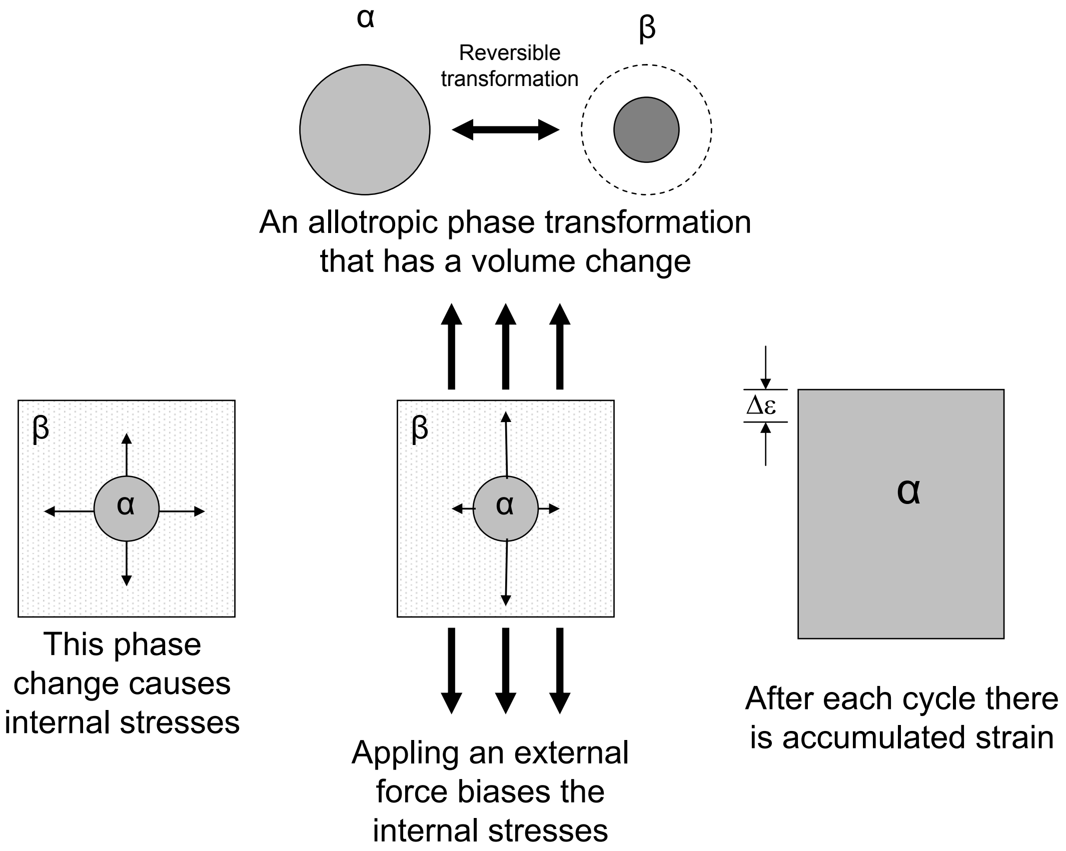

Figure 2.2. Schematic of transformation superplasticity.

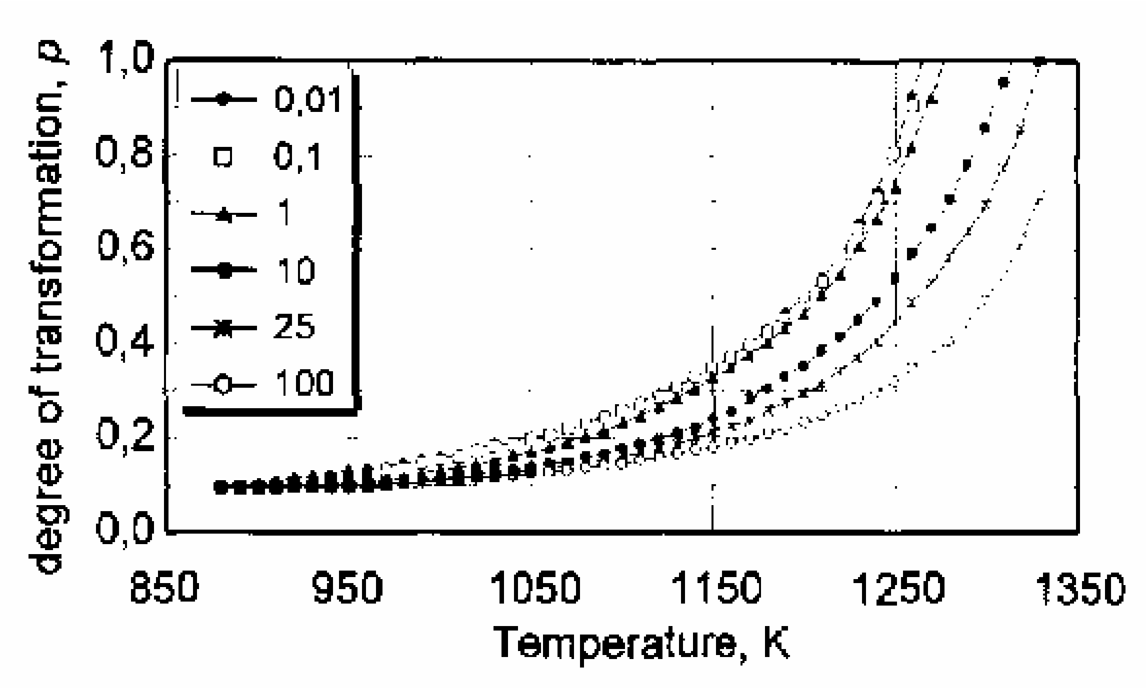

Figure 2.3. Transformation extent in Ti-6Al-4V as a function of temperature and heating rate (in K/s) [48].

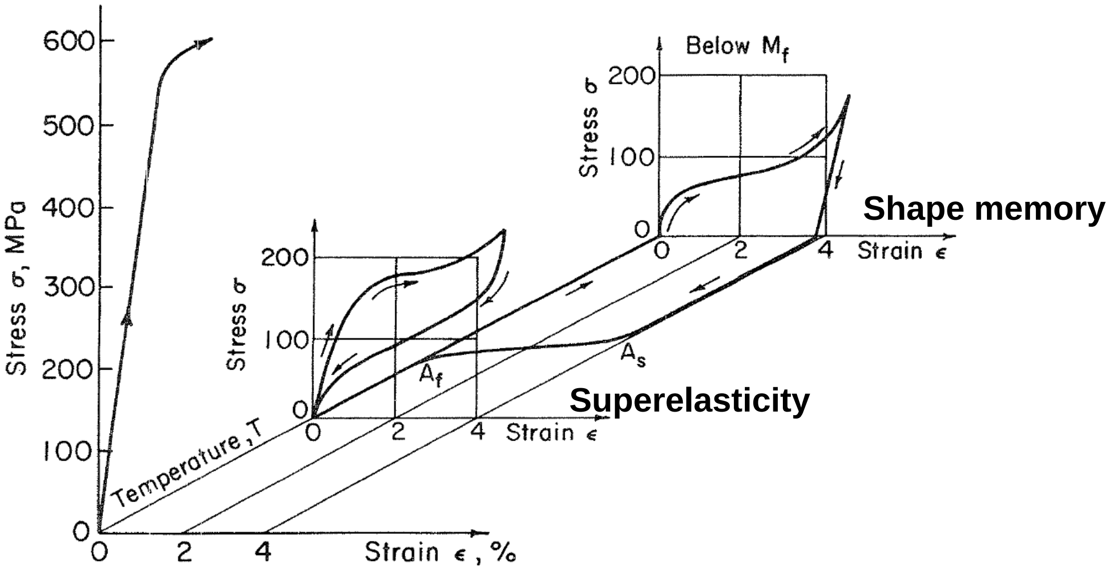

Figure 2.4. NiTi thermo-mechanical diagram showing shape memory and superelastic effect [79].

2.3. Superelasticity

Superelasticity and shape memory are linked phenomena; in each of them a phase change allows for the recovery of large strains. Superelasticity occurs when there is a reversible, non-diffusional, stress-induced, phase change. The shape memory effect occurs through twinning under stress and corresponding de-twinning upon a thermally caused phase change. Figure 2.4 shows the complex thermo-mechanical response of NiTi. In the superelastic case (higher temperature) the material is fully austenitic, and stress induces martensite. In the shape memory case (lower temperature) the material is fully martensitic (below M_f) and twins upon stress. When heated, it transforms into austenite, recovering its previous shape and on re-cooling, the non-twinned metal is formed, maintaining its recovered shape.

For NiTi, this transition temperature and critical stress can be changed by composition or by heat treatment. Small amounts of additional nickel lower the martensite transition temperature significantly. Contamination such as oxygen will preferentially bind with the titanium, changing the effective stoicheiometry and shifting the transition temperature, altering the associated mechanical properties. For superelasticity, heat treatment is also significant, because the stress-induced phase change will only happen above a given stress (dependent on temperature and composition), but if slip can occur below this critical stress there is plastic deformation instead of stress-induced phase change. By heat-treating to precipitate Ti_3Ni_4, the slip is inhibited, allowing for superelasticity. This effect can be seen in figure 2.5.

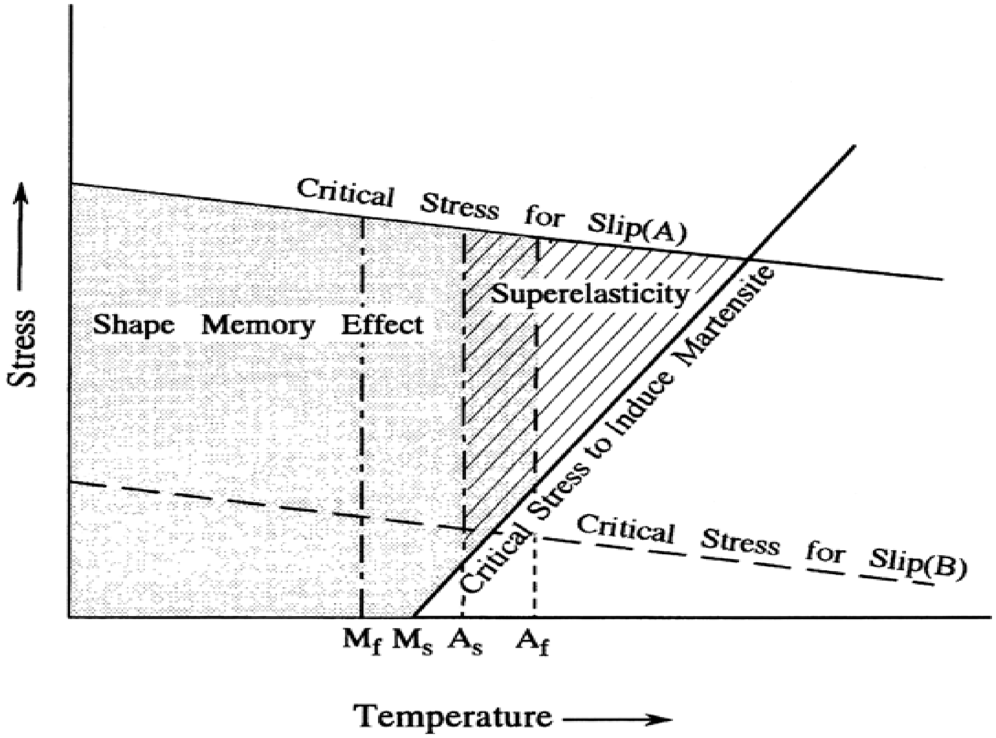

Figure 2.5. Precipitation strengthening enhancing superelastic effect [79].

CHAPTER 3

Experimental Procedures

3.1. Density and Porosity

Three different densities are important in the discussion of porous metals. First is open porosity, which occurs when pores have a path to the surface of the specimen. The second is closed porosity, where pores are enclosed by matrix. The third is total porosity, or envelope porosity, which includes both open and closed pores. Experimentally only the closed porosity and total porosity are easily measured directly from which open porosity is calculated.

In all of the porosity determinations, volume and mass are the measured quantities. The density ρ_{exp} is calculated from the ratio of the mass to volume. The porosity is then calculated by taking the known bulk density, ρ_{bulk} and determining the volume fraction of pores, P. In previous studies this was calculated as:

$$P = \frac{\rho_{metal} - \rho_{exp}}{\rho_{metal}} \tag{3.1}$$

This equation implicitly assumes that the pores have zero density, but in fact, at least for as-HIP samples, this oversimplification results in significant error. A more accurate equation that takes into account the density of the compressed argon in the pores ρ_{Ar} is:

$$\frac{\rho_{metal} - \rho_{exp}}{\rho_{metal} - \rho_{Ar}} = P \tag{3.2}$$

For all the experiments previously done with commercial purity titanium [**37**, **39**, **40**], equation 3.1 was used, leading to an underestimation of the porosity by around 8% of the porosity listed. This change, while small, can have a significant impact on the porosity evolution (see section 5).

Gas pycnometry is able to find the volume of a sample by comparing the amount of gas in a chamber with, and without a sample. Since this method uses a gas, it will infiltrate all pores that have a path to the surface finding only the volume that gas cannot get to (closed pores and the material itself). For this reason, helium pyccnometry was used to find the closed porosity of samples. In specific, pycnometry is performed by putting a known pressure of a gas in a first chamber and then allowing the gas to expand into a second chamber of known volume. A pressure drop is measured and the volume of the first chamber can be calculated. A sample is then introduced in the first chamber and the process repeated, but with the sample in the chamber there is less initial volume for the helium. This is detected when the gas expands into the second chamber and a lower pressure is recorded than when there was no sample. By calibrating the system with a standard volume, the sample volume can be calculated.

Each measurement of volume is composed of 10 individual pressurization and equilibration steps. Because of the number of trials all of the experimental error in this method is traced from the change in volume of the chamber upon opening and closing (differing O-ring compression, seating etc.). This accounts for approximately ±0.002 cm^3, resulting in less than 1% absolute error in porosity calculations for typical foamed samples of 0.25 cm^3. For very small samples or very small porosities, this method is not as useful however, as 1% absolute error is larger than the porosity itself.

Total porosity was found through mass difference in and out of water (Archimedes method). In order to prevent infiltration of the water and get a true envelope volume measurement, a small amount of vacuum grease (typically less than 2mg) was used to seal the outer pores. A high precision balance measured the mass of the sample in air and water, the difference via the Archimedes principle is the buoyancy force which is equal to the density of the liquid times the volume of the sample. De-ionized water was used and the temperature measured for accurate water density, from which the volume of the sample is calculated. As previously stated, the volume is used to calculate the density, and the density is used to calculate the porosity (equation 3.2).

In the water displacement measurement, the most significant error source is the surface tension of the water on the hanging wire. This error can be minimized through careful hanging of the basket and amounts to around ±5mg error, or in terms of volume, $\pm 0.005 cm^3$ error. Errors appear to be random and therefore accuracy can be improved through repeated runs. For this reason, at least 5 density measurements were made every time porosity was required. For samples with low porosity, and for the solid standard, at least 20 measurements were made on large samples to reduce relative error. Due to the random nature of the errors, the standard deviation overestimates the errors, for this reason the error range stated represents a 95% confidence interval calculated as:

$$Error = \bar{f} \pm 1.96\left(\frac{StDev}{\sqrt{n}}\right) \tag{3.3}$$

3.2. Microscopy

All of the samples were polished using the same method. Each specimen was mounted in phenolic resin at 180^{o}C and 25 MPa pressure (20 kN force) for 4 minutes and then cooled for 4 minutes with running cold water. Samples of over 35% porosity were only pressed at 12 MPa (10kN) for 6-8 minutes in order to prevent collapse of the pores. Next, a series of progressively finer polishing agents was used to smooth the sample on a four sample Buehler autopolisher. The first step was to grind samples flat with 320 grit SiC paper (5 min., 6lbs/sample, 240-320 RPM contra rotation). Next, 9 μm diamond suspension on ultrapol cloth was used (4 min., 2-6 lbs/sample, 120-150 RPM, complementary rotation). Lastly, they were polished on microcloth using 0.05 μm alumina suspension (5 min., 1-2 lbs/sample, 120-150 RPM, complementary rotation). Optical images were taken using a Nikon inverted microscope with a Diagnostic Instruments digital camera. Scanning electron microscope images were taken with the Hitachi 3500, and Hitachi 3400 at the EPIC facility.

3.3. Furnace

The vacuum furnace used in all of the isothermal and thermal cycling studies was manufactured by Centorr. Early experiments used a turbomolecular pump, with later experiments using a small air-cooled diffusion pump. In both cases, vacuum was maintained below 10^{-5} Torr, and typically around $4{\cdot}10^{-6}$ Torr measured at the chamber. Temperature was measured by a type K thermocouple coated with boron-nitride. All of the active and structural parts in the hot zone were made of molybdenum (Mo). The heating elements themselves were Mo mesh, the heat shielding was layers of Mo foil and wire. Cooling of the walls was performed by chilled water pumped through copper plates on the back and door of the chamber. Samples were held on a Mo plate supported by three molybdenum posts. For all the isothermal anneals, a 25.4 mm outer diameter, 100 mm high titanium tube was placed around the sample to act as a getter. Tests found there was no measurable temperature difference inside and outside the tube. An image of the open furnace can be seen in figure 3.1.

3.4. Foam Preform Creation

Using the Kearns argon entrapment method described in the introduction (section 2.1.3) a number of samples were made. These samples are broken down into two major groups, the first group is those samples where the powders were sent alone to be processed by the HIP companies. Typically powders were sent when larger billets were required. Previous researchers in our lab have sent commercial purity titanium (CP-Ti) and Ti-6Al-4V to the HIP companies where they were put into mild steel cans, backfilled with argon, sealed and HIP'ed. NiTi powders were also sent for HIP'ing during the current investigation. A number of differently sieved powders were often layered in a single can. Information on the purity, manufacture, and shape of the powders can be found in table 3.1. Tables of each section of the samples have been compiled, CP-Ti in table 3.2, Ti-6Al-4V in table 3.3 and NiTi in table 3.4.

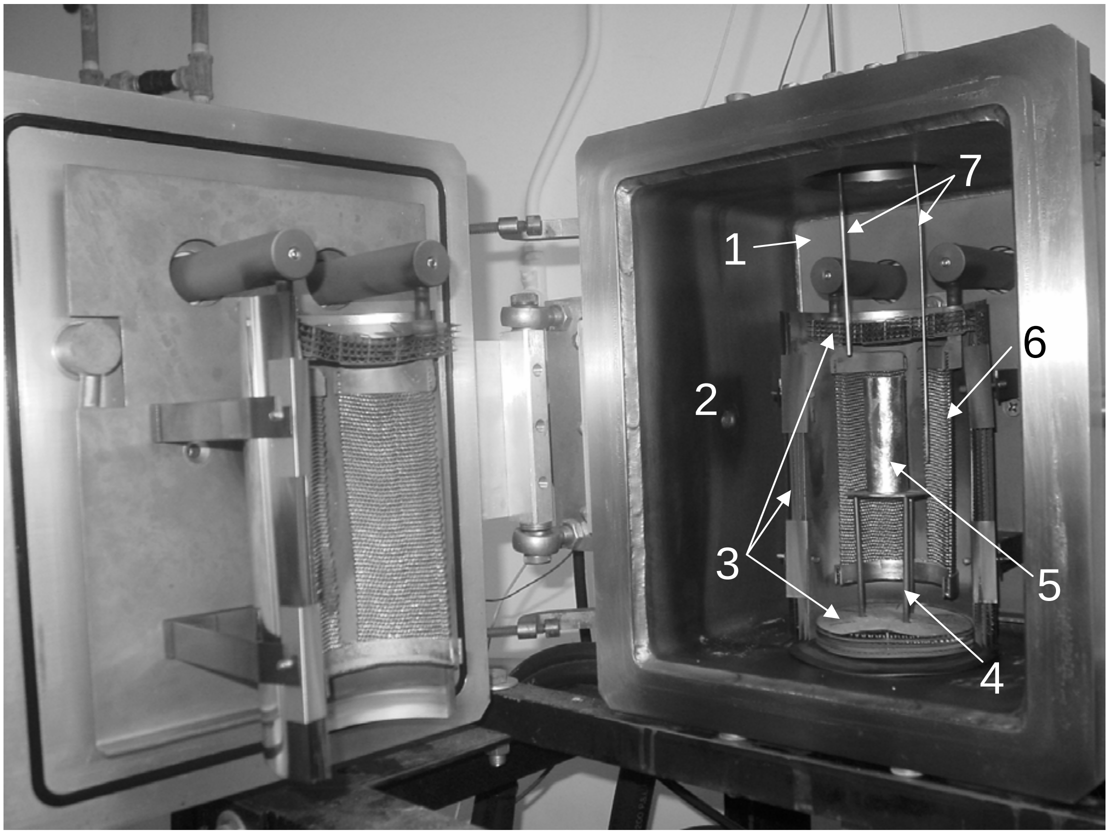

Figure 3.1. Vacuum furnace showing: 1)copper heat exchanger, vaccuum inlet is behind this plate, 2)Vacuum gauge port, 3)Molybdenum heat shielding, 4)Molybdenum stand, 5)Titanium getter around sample, 6)Molybdenum mesh heating elements, 7)Thermocouples.

The second group of samples are those that were canned, and backfilled in our lab and sent to the HIP company only for the final densification step. Samples of Ti-6Al-4V were created with pre-alloyed, grade 5, Ti-6Al-4V powders from Starmet corp that had been sieved to between 125μm and 149μm. Nickel titanium samples were created using pre-alloyed martensitic NiTi powders (Ni 50.6 at.% Ti, 99.9% purity, from Specialty Metals Corp., NY) that were mixed with small quantities of elemental nickel powders (99.9% purity, size between 44 and 177 μm, from Specialty Metals Corp., NY), to create

Powder Type	Purity	*Manufacture Company*	Shape
Ti-6Al-4V	Grade 5	Starmet (Concord, MA)	Spherical
CP-Ti	Grade 2	Starmet (Concord, MA)	Spherical
NiTi	99.9%	Specialty Metals (Concord, MA)	Spherical
Ni	99.9%	Specialty Metals (Concord, MA)	Spherical

Table 3.1. Properties of powders used in HIP'ing.

Sample	Powder Size (μm)	*Argon Backfill* Press. *(MPa)*	HIP Company
1	unsieved (<177)	0.33	UltraClad (Andover, MA)
3	62-88	0.33	Conaway Technologies (Hilliard, OH)
5	105-125		
7	149-177		
9	25-37	0.33	Bodycote (Andover, MA)
11	355-500		
9a	25-37	0.71	Bodycote (Andover, MA)
11a	355-500		
TiWires	250 (wire)	0.71	Bodycote (Andover, MA)

Table 3.2. CP-Ti HIP'ed at 890^{o}C, for 120 minutes, at 100 MPa [60].

a composition of 51.0at.%Ni-Ti. A second set of NiTi samples using the same pre-alloyed powders but, less nickel was added in order to create samples that would exhibit superelastic properties at body temperature. Through a mistake in calculations, the composition was 49.0% Ni instead of 50.4%, which crated a material that is more aptly called a shape memory material with an austenitic onset temperature of 94^{o}C. While the composition will most definitely change the uses and room temperature mechanical properties, this small change in composition should be inconsequential for the foaming and creep studies at high temperature.

For the samples created in our lab, the powders were canned in thick wall 9.53 mm outer diameter, 7.04 mm inner diameter, low carbon, steel tubes purchased from McMaster

Sample	Powder Size (μm)	*Argon Backfill* Press. *(MPa)*	HIP Company
2	unsieved (<177)	0.33	UltraClad (Andover, MA)
4	62-88	0.33	Bodycote (Andover, MA)
6	105-125		
8	149-177		

Table 3.3. Ti-6Al-4V HIP'ed at 950^{o}C, for 240 minutes, at 100 MPa.

Sample	Powder Size (μm)	*Argon Backfill* Press. *(MPa)*	HIP Company
A	44-177	0.21	UltraClad (Andover, MA)
B	44-177	0.45	Bodycote (Andover, MA)

Table 3.4. 51.0 at. % nickel-titanium HIP'ed at 1066^{o}C, for 240 minutes, at 100 MPa.

Carr. The tubes were cleaned with a soap water solution and throughly rinsed with water, and then rinsed twice with acetone, and dried at 120^{o}C overnight. When cut, each of the tubes was around 50cm long, and was crimped and welded at the bottom. Pre-measured powders were then added via a funnel into the tube and packed by hand with a steel rod. The tube containing powders was attached to a 3 way valve for both argon and vacuum. Each tube was alternately evacuated and backfilled with argon at least five times in order to remove reactive atmospheric gases. The tube was then backfilled with 99.999% pure argon gas and crimp-welded using specially modified bolt cutters that had their faces ground flat. The two flat faces of the bolt cutters were separated by 1.25 times the wall thickness of the tubes (3mm). Crimp-welding is performed by first heating the tube with an oxy-acetylene torch to orange heat and then pressing the hot zone with the modified bolt cutters. Initial problems with the top not being fully welded were attributed to metal powders clinging to the side walls. In order to prevent this, small amounts of steel wool were forced into the tube to clean the wall and prevent the powder from moving. Once sealed these tubes were then sent to be HIP'ed at UltraClad corp. (Andover, MA).

The general procedure above was enhanced using a novel method for including more argon. In the old method, there was a maximum pressure that could not be exceeded due to the heating and welding at the top. Too much pressure at the weld point would lead to blistering and loss of argon. In the new method, the bottoms of the tubes were immersed in liquid nitrogen to condense the argon (liquid nitrogen boils at 77K, argon freezes at 84K [**52**]). This allowed for large quantities of solid argon to be entrapped in the tube while keeping the pressure at the weld point low. A schematic diagram of this method can be found in figure 3.2. There is no way to directly measure the pressure of the argon trapped inside the tube, but the system volumes can be solved for and the amount of gas can be calculated. A list of all the high pressure samples along with their HIP processing conditions can be found in table 3.5.

For the large HIP'ed billets, samples were cut using electro-discharge machining (EDM). Before use in thermal foaming experiments the sides were lightly polished with 400 grit SiC paper to remove the EDM damaged layer. For the samples created in tubes lathing was used only on the first few samples. Mechanically removing the steel was found lacking in that it wasted material (HIP tubes are often slightly flattened), was time intensive, and due to NiTi's hardness expensive in terms of tooling. It was instead found that it was simpler and more efficient to dissolve the steel in an electro-chemical reaction. Immersing the as-received tube in a bath of 10% acetic acid, salt, and water with a voltage of less than 2V preferentially removed the steel. Both NiTi, and Ti-6Al-4V are less reactive than the low carbon steel can, and therefore the can is preferentially dissolved. After

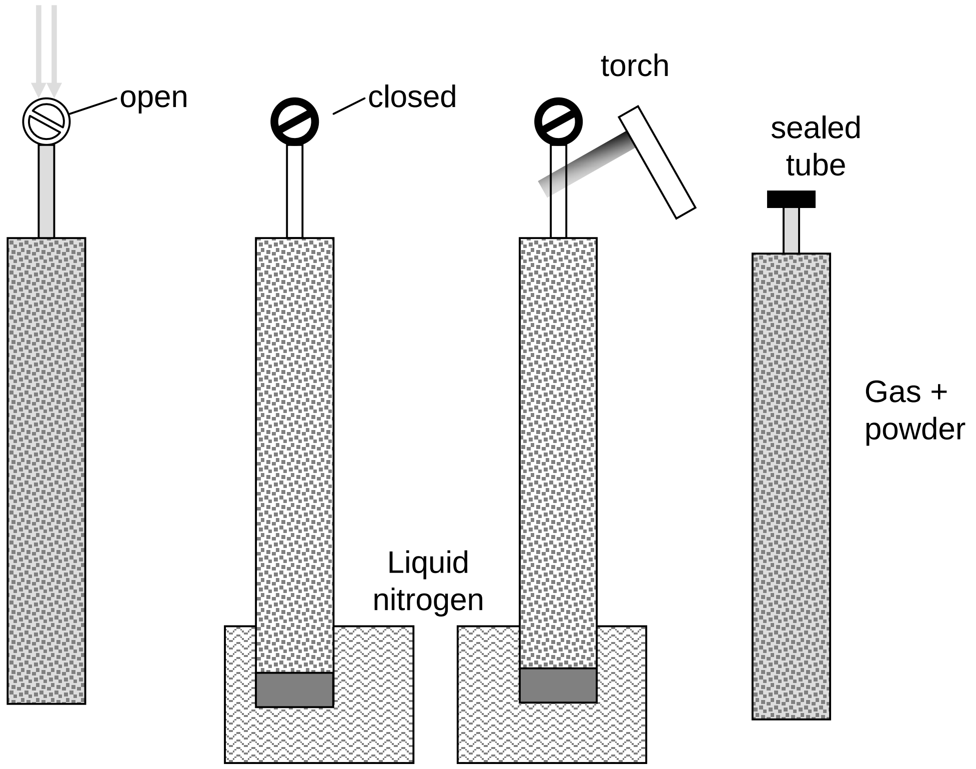

High pressure (> 5 atm) Argon gas is put into the tube along with the powder

Placed into liquid nitrogen the argon condenses at can bottom leaving low pressure at the top pipe (< 1 atmosphere), allowing the tube to be welded shut

Taken out of the liquid nitrogen, the solid argon vaporizes re-pressurizing the can

Figure 3.2. Novel method for trapping high pressure argon in tubes.

approximatly three days the steel had been fully removed and the samples were sanded to remove any oxide layer, and finally sectioned on a diamond saw. From expected chemical dissolution reactions, post-removal material foaming, and visual examination, no damage to the NiTi was found through use of this steel removal method.

Sample	*Effective Backfill Press. (atm.)*	*Material*	Powder Size (μm)	*HIP Temp. (^oC)*	*HIP Time (min.)*	*HIP Press. (MPa)*
Ar1	2.9	Ti-6Al-4V	120-140	980	240	100
Ar2	0.3					
Ar3	3.3					
Ar4	5.5					
NiTi1	0.9	NiTi	44-177	1065	240	207
NiTi2	1.4					
NiTi3	2.5					
NiTi4	5.3					
NiTi5	6.7					
NiTi6	33					
NiTi7	24					
NiTi8	11					

Table 3.5. High pressure NiTi (49 at.% Ni), and Ti-6Al-4V samples created through Ar condensation method and HIP'ed at UltraClad (Andover, MA)

NiTi Sample Designation	*Initial Porosity (%)*	*Ti-6Al-4V Sample Designation*	*Initial Porosity (%)*
NiTi1	0.09	Ar1	0.21
NiTi2	0.25	Ar2	0.31
NiTi3	0.43	Ar3	0.50
NiTi4	0.98	Ar4	0.59
NiTi5	1.34	4	0.41
NiTi6	6.26	6	0.38
NiTi7	3.92	8	0.40
NiTi8	2.26		
A	0.40		
B	0.77		

Table 3.6. Initial porosity of all samples used.

3.5. Ultrasonic Modulus Measurement

The elastic properties of a material can be found by measuring the speed of sound through the material [**53**, **54**]. The basic equations relating the velocity of the ultrasonic propagation to the elastic constants are:

$$V_s = \sqrt{\frac{E}{2\rho\left(1+\nu\right)}} \tag{3.4}$$

$$V_l = \sqrt{\frac{E}{\rho}\frac{\left(1-\nu\right)}{\left(1+\nu\right)\left(1-2\nu\right)}} \tag{3.5}$$

where ρ is the density, ν is Poison's ration, E is Young's modulus, V_l is the longitudinal velocity and V_s is the shear wave velocity. By measuring both shear and transverse velocities the two unknown elastic parameters can be calculated.

The velocity determination can be done in two ways. The first is in pulse-echo mode where only one transducer both excites and records the mechanical impulse. If the sample is low damping, this can often create many pseudo-independent signals as the sound travels back and forth through the sample, giving large amounts of information. If the sample has high dampening (either intrinsically to the material, or a large sample), the echo can be so weak as to be lost in the noise. Transmission testing uses two transducers, one which excites the sample and the second which records it. In this case, the signal has to pass through less material which gives a stronger signal, but at the expense of multiple reflections which can improve accuracy.

The frequency of the piezo-electric exciter and receiver has to be carefully chosen when used on porous materials. In an ideal situation, the wavelength should be 10 times larger than the internal feature size (in our case pores) while at the same time being 10 times smaller than the sample dimensions [**55**]. This gives a factor of 100 between pore dimensions and sample size. Another problem is that the signal drops quickly with increasing sample size which places a limit on how large the sample can get (a significant problem for pulse-echo). A factor of 3 (feature size 3x smaller than wavelength, sample sized 3x larger than wavelength) was considered the minimum for reliable data. From the available transducers it was determined that the 5Mhz frequency would be best. Table 3.7 shows the expected wavelength in fully dense, 25% and 50% porous Ti-6Al-4V, and fully dense, 10% and 20% porous NiTi calculated by using estimated mechanical parameters, equations 3.4 and 3.5, and the wave equation ($V = \lambda\nu$). The elastic modulus was estimated by using the Gibson and Ashby modulus-density relationship [**1**]:

$$\frac{E}{E_o} = \left(\frac{\rho}{\rho_o}\right)^2 \tag{3.6}$$

where E and E_o are the Young's moduli of the foam and the fully dense metal, ρ is the density of the foam, and ρ_o is the full metal density. All of the samples tested were between 5 and 10 mm total height, and the typical pore size was less than around 300 μm for Ti-6Al-4V and less than 100 μm for NiTi. As can be seen in table 3.7, the wavelengths calculated fall within the requirements for accurate measurement.

Samples were mechanically coupled with high viscosity fluid (molasses) to the transducer(s). A digital oscilloscope was then used to record the signal. Previous measurements

Material	*Porosity (%)*	*Density* (kg/m^3)	*Test Modulus (GPa)*	V_l *(m/s)*	*Wavelength (mm)*
Ti-6Al-4V	0	4500	125	6300	1.25
	25	3225	70	5400	1.09
	50	2250	31	4300	0.87
NiTi	0	6500	70	3800	0.76
	10	5850	57	3600	0.72
	20	5200	45	3400	0.68

Table 3.7. Transducer wavelength properties in different porosities of Ti-6Al-4V and NiTi.

had used the pulse-echo technique, but damping became a significant problem, and so the transmission method was used. Matec software was used to create a pulse and record the output of the second transducer. Using the time for the pulse to travel through the sample, measured sample dimensions, and equations 3.4 and 3.5, the Young's modulus, could be calculated.

Error in modulus is due to errors in measurement of the velocities. Repeated measurements of time of flight through the samples showed less than a ± 0.01μs difference. A slightly more significant problem was the very small changes that indicate "first" signal on the receiving transducer. Reasonable arguments could be made for a systematic difference in the measured time of flight and the true time which could be as high as ± 0.1 μs. Even for the shortest time of flights (smallest samples, with least porosity) the random error in velocity is only 0.4% and largest systematic errors possible are 4%. The errors here are the maximum possible, but from the agreement with bulk properties, and theoretical predictions the expected error is in all likelihood significantly less.

3.6. Mechanical Testing

Mechanical testing was done on an Instron-type screw driven testing machine. A compression cage with carbide inserts was used to keep the platens aligned. Crosshead displacement was monitored and corrected by the machine compliance. Load was measured by a 300 kN load cell in the loading train. Due to the thermally sensitive nature of the NiTi phase transition, cyclic loading tests were done with strain rates lower than $3{\cdot}10^{-5}$/s. This was determined to be a reasonable strain rate by testing strain rates up to $5{\cdot}10^{-3}$/s and finding no measurable temperature increase.

3.7. NiTi Creep

A Centorr vacuum furnace with a hydrolic pressure load train was used to compress NiTi samples at high temperature. Machined flat and parallel 2.54 cm sections of 1.27 cm round bar stock NiTi (50.8 at.% Ni) from Nitinol Devices and Components (Freemont, CA) were compressed at four different temperatures (950, 1000, 1050, 1100 ^oC) with stresses from 3-11 MPa. The samples were contained in a tungsten-carbide-cobalt (WC-Co) cage with a hole for a thermocouple to be inserted. Pressure was applied by a load train consisting of nickel superalloy holders connected to WC-Co rods. Crosshead displacement and time were monitored and output. The machine compliance was not corrected for due to the constant stress nature of creep experiments.

3.8. Heat treatment

Three different heat treatments were examined in NiTi: homogenized, homogenized and age, and furnace cooled. Homogenization was performed in a graphite crucible inside an infra-red radiation furnace. The focus of the heating lamps was in the middle of a quartz tube that was under mechanical vacuum (1x10^{-3} torr). After 4 hours at 1000^{o}C, the quartz tube was backfilled with 99.999% pure argon and the sample quenched in ambient temperature water. Aging of the sample was performed by a thermal soak at 400^{o}C in air for 4 hours, in a standard laboratory furnace, and water quenched.

Samples that were tested in the furnace-cooled state, were not heat-treated after annealing in the vacuum furnace. A temperature vs. time curve on cooling is shown in figure 3.3.

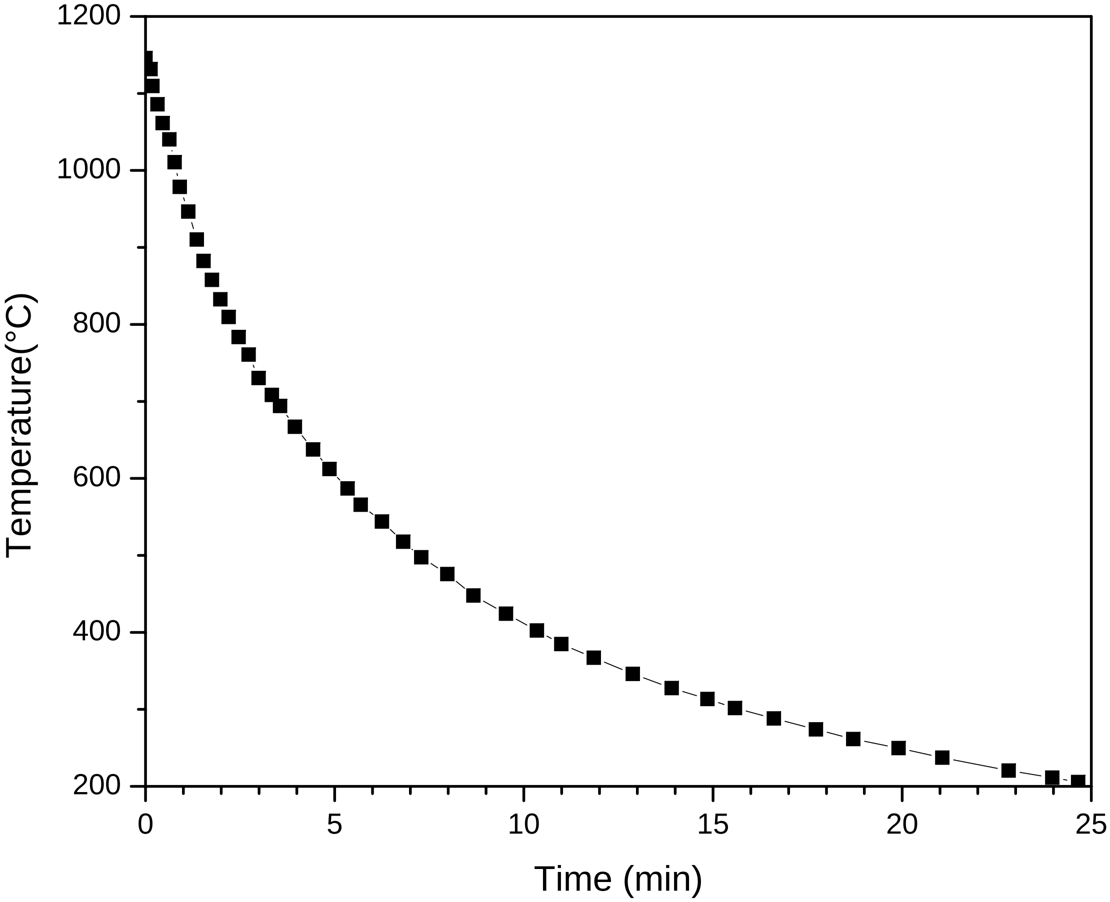

Figure 3.3. Typical cooling curve for vacuum furnace.

3.9. Image Analysis

Porosity distributions were determined by digital image analysis. In this method, scanning electron microscope images were taken with the Hitachi 3500, and 3400 systems. The flat gray section of the metal was then selected with the "wand" function of Photoshop. Modifying the selection through successive dilations and contractions eliminated noise and converted the image to a binary black and white image. ImageJ was then used to analyze the binary images produced, providing a list of every pore, its area in square pixels, and the total area fraction of pixels. Next the pores were binned into 15 bins in order to use Saltykov analysis [**56**, **57**]. Each of the i bins was found by the equation $\mathrm{D}_{max} \times 10^{-0.1(i-1)}$, where D_{max} is the largest pore measured (which is then assumed to be the largest pore size). From this calculation, the three dimensional pore radius distribution is created. Due to the successive nature of this method there are cases where calculations indicate small numbers of pores with negative sizes, these were discarded as artifacts of this method. A series of images demonstrating this method can be seen in figure 3.4.

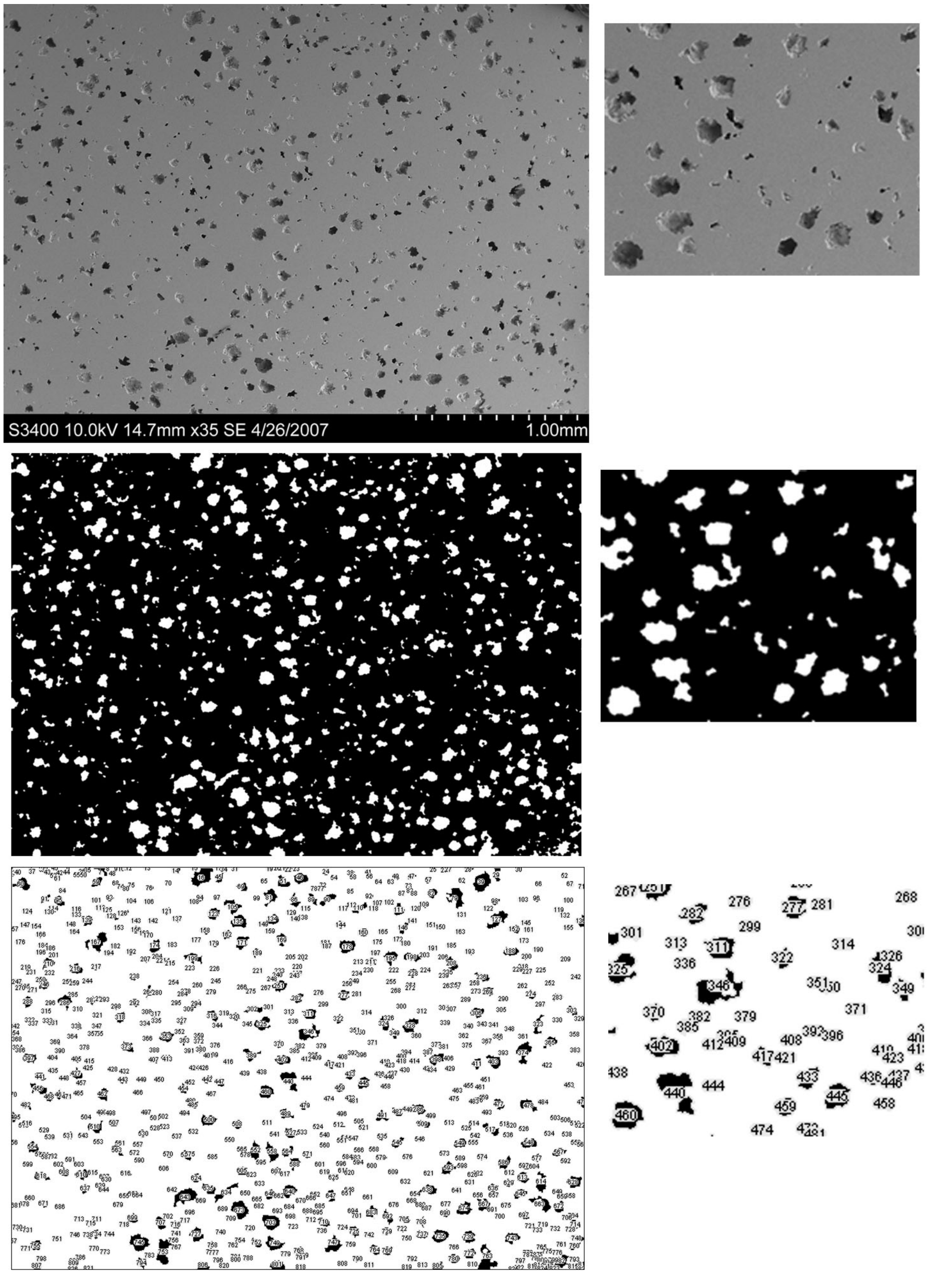

Figure 3.4. Series of steps in digital image analysis.

3.10. Synchrotron X-Ray

Synchrotron X-ray analysis of the samples were performed at beamline 1IDC at Argonne National Labratory's Advanced Photon Source (Argonne, Il). A heat treated and aged, NiTi sample of 2.5 X 2.5 by 5 mm dimension was placed in a screw driven mechanical testing rig. Strain was measured with compliance compensated crosshead displacement, as well as glued Omega pre-wired strain gages. The strain rate was less than $5{\cdot}10^{-4}$ per second. The mechanical testing rig with the sample was placed in the path of a synchrotron x-ray beam of 100 μm X 100 μm at 80.72 keV. The sample was actively moved for between 20 and 50 seconds while images were captured to improve ring uniformity by sampling more grains. The temperature was nearly constant over the course of the experiments, varying only between 22 and 25^oC. This temperature range is well within the fully austenitic region, and small enough to have little effect on mechanical properties. An image plate (Mar345) with a 345 mm diameter, operating in full mode and providing 100 μm pixel size with 16 bit dynamic range was 1.1 m from the sample and was used to capture the diffracted x-ray image. A photograph of the setup can be seen in figure 3.5.

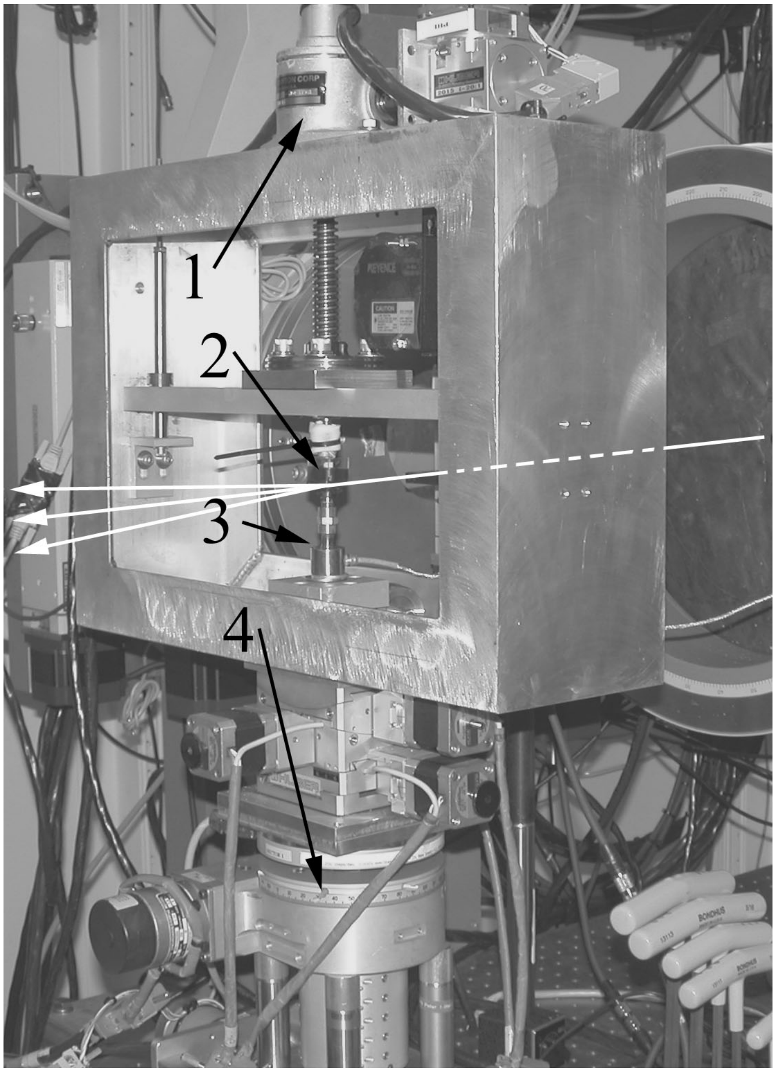

Figure 3.5. Image of the synchrotron setup at the Advanced Photon Source showing: 1)Screw driven mechanical testing frame, 2)Sample position, 3)Load cell, 4)Positioning motors. The white arrows show the beam path before and after diffraction form the sample.

CHAPTER 4

Experimental Results and Discussion

4.1. Titanium

4.1.1. Foaming

The foaming kinetics and foam morphologies of commercial purity titanium (CP-Ti) were the main focus of research in our lab before my arrival and are reported in [**36**,**38**–**40**,**58**–**61**]. The current study extends this work to Ti-6Al-4V as well as enhancing the processing itself. The first expansion on previous work done was to perform the foaming step in a vacuum furnace (as described in section 3.3), as opposed to flowing argon. Changing the high temperature anneal atmosphere has two effects. First, there is a reduction in contamination which improves hot ductility and allows for higher porosity before the internal pores connect and release their argon. Figure 4.2 shows the qualitative difference in surface contamination, with samples in the new system being much less oxidized. Secondly, by using vacuum instead of higher purity argon, the pressure difference between the pores and the outside environment is increased. The foaming rate is then enhanced in both isothermal and thermal cycling experiments. A direct comparison was done on CP-Ti; figure 4.1 shows the porosity vs. time curves of both thermal cycling and isothermal experiments. More rapid foaming is seen in both cases in vacuum, but due to the small initial porosities, neither of the isothermal specimens fully foamed. It is expected that less contamination would have allowed higher terminal porosity, but it is not proved.

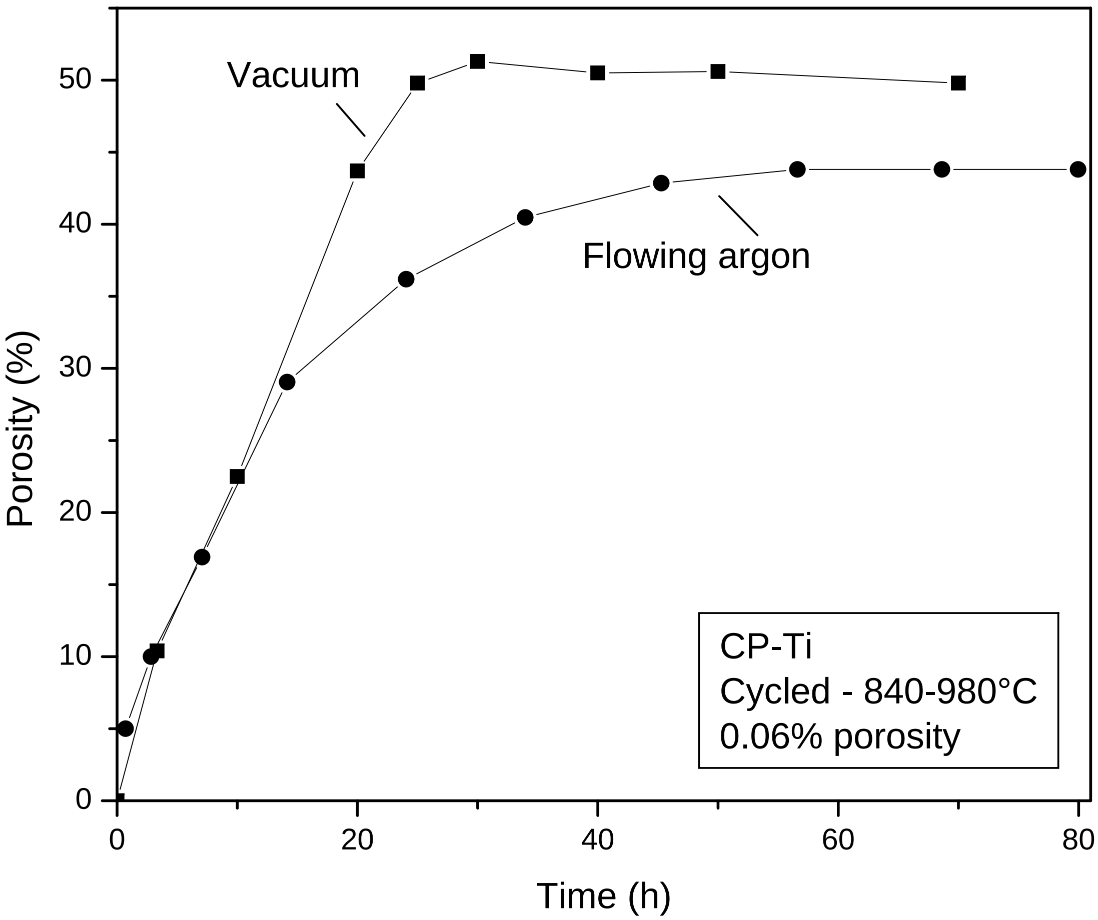

Figure 4.1. Porosity evolution of CP-Ti samples with 0.06% initial porosity foamed under vacuum (square) and flowing argon (circle). Open symbols represent isothermal anneal at 990°C, solid symbols are used for thermal cycling 840-980°C with 4 minutes per cycle.

A second major processing change was the method for increasing the amount of argon that could be trapped in the HIP can using the high pressure argon condensation method (described in section 3.4). Previously, the initial porosity was controlled by changing the powder size used, which alters the amount of empty space before compaction. Changing the powder size can easily change other variables, such as number density of pores, pore

Figure 4.2. Image of CP-Ti samples foamed under high vacuum (left) and flowing argon (right) showing contamination.

morphology and oxygen content. An alternative approach used by this study is to directly control the amount of argon put into the system. By increasing the argon content, it is also possible to foam to higher total porosity in the isothermal case. Figure 4.3 shows isothermal expansion of Ti-6Al-4V samples. It can easily be seen that increasing the backfill pressure increases the rate of foaming significantly. Samples A1 and A2 were created with the old method of canning while samples labeled B-E were created with the new high pressure method.

The last major processing change was, as stated before, the material itself. Ti-6Al-4V has a more complex transformation profile and therefore more complex transformation superplasticity. Ti-6Al-4V, unlike CP-Ti, has a broad phase change, where α-Ti gradually changes to β-Ti over a 300^{o}C range (as seen in figure 2.3). Unlike CP-Ti the phase change is also diffusion controlled so the heating and cooling rate can change the fraction that transforms in a given time (also seen in figure 2.3). For these reasons, there is not just a simple strain per cycle, but instead a strain per cycle that is based on the cycling rate

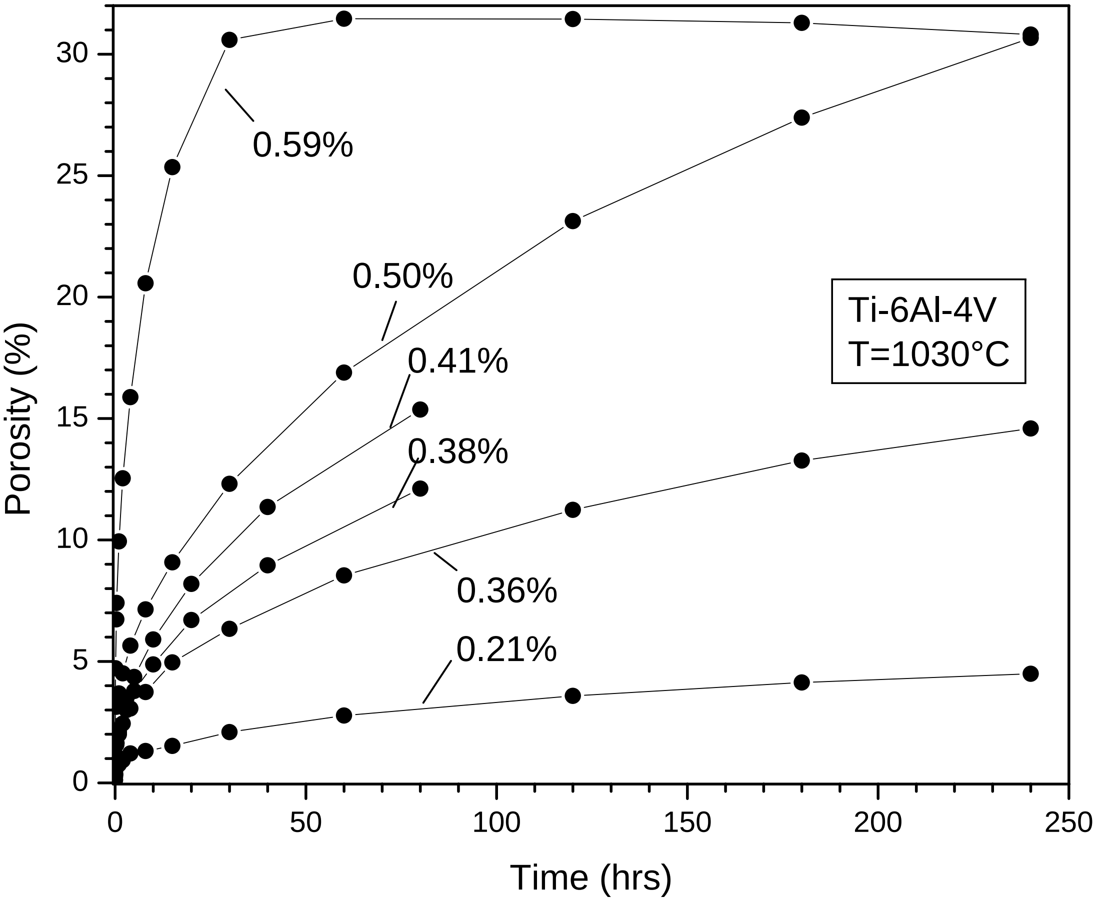

Figure 4.3. Ti-6Al-4V samples foamed at 1030^{o}C with different backfill pressures.

and temperature range. Cycling too fast does not allow full transformation and therefore the overall rate of pore growth is not enhanced as much as in CP-Ti. Figure 4.4 show the results of different cycling rates on the growth of the pores. It was expected that doubling the cycling rate should have doubled the foaming rate, which is not what was seen. It is then just chance that all three cycling rates gave the same foaming kinetics.

Looking at the same data plotted against the number of cycles, figure 4.5, shows the difference in strain per cycle. Referring back to figure 2.3 the different heating rates and

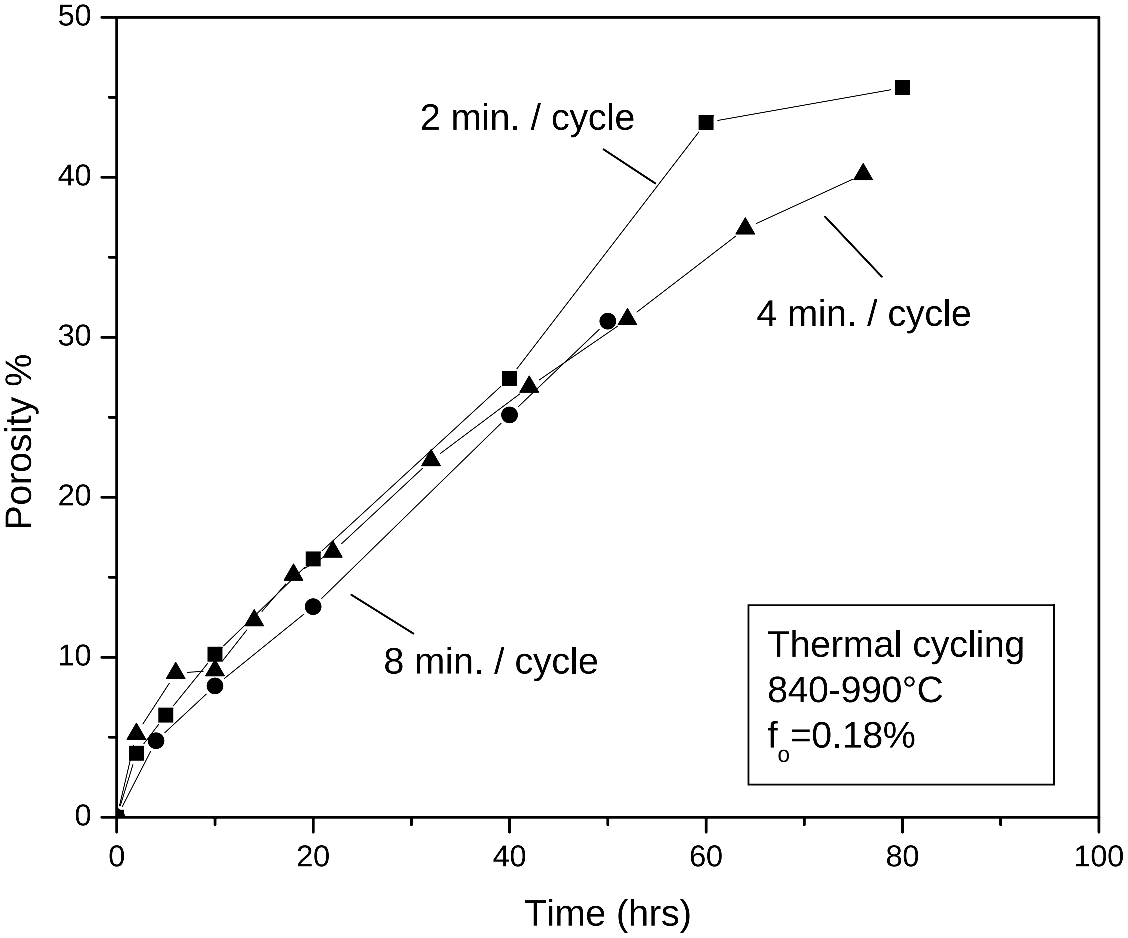

Figure 4.4. Cycling rate dependent foaming, Ti-6Al-4V cycled between 840 and 990^{o}C.

cooling rates show that different amounts of total transformation occur. At low porosities (under 10%) creep of the matrix can account for some of the difference in strain per cycle, but at higher porosities the contribution of isothermal creep is very small (as could be seen in the isothermal expansion). It is to be expected that the faster cycling rates would have less transformation, and therefore less strain per cycle.

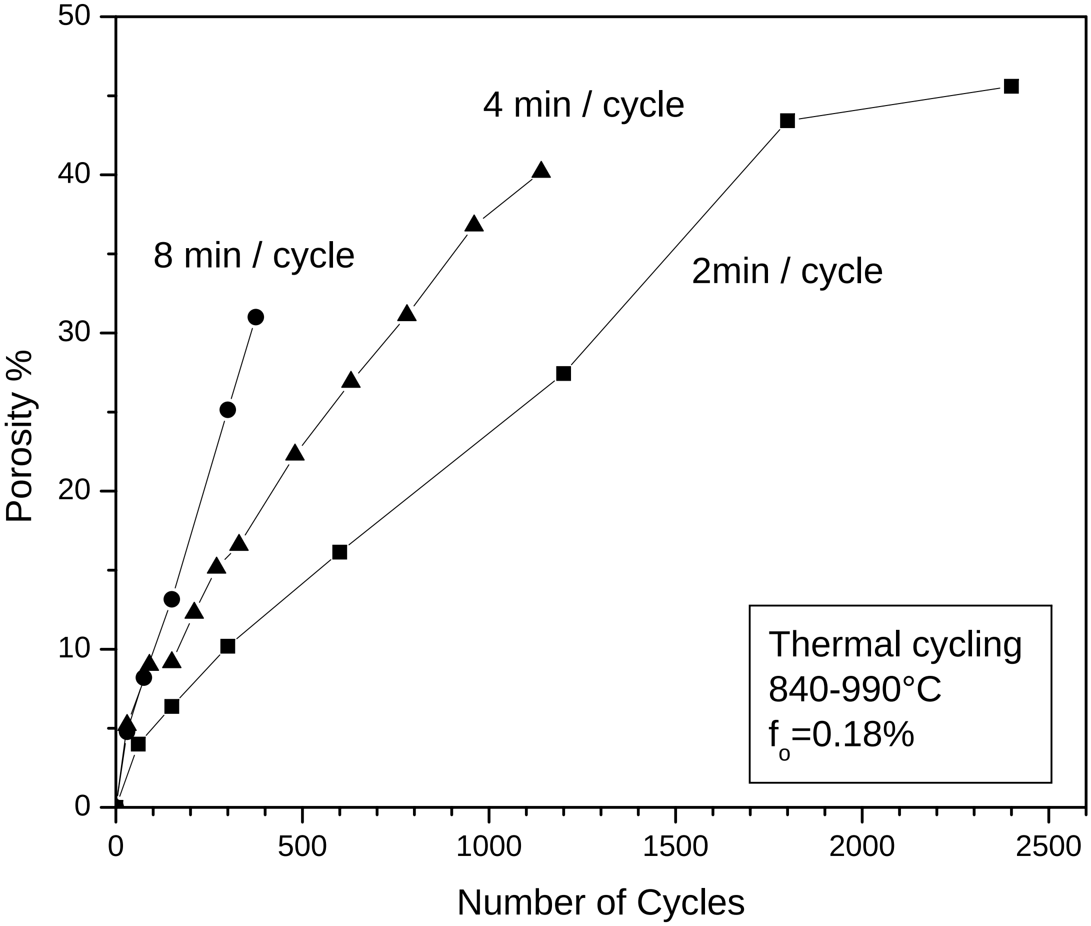

Figure 4.5. Foaming rate as a function of number of cycles for Ti-6Al-4V cycled between 840 and 990^{o}C.

A cycle time of 8 minutes was chosen as the shortest time in which the majority of the transformation is complete. Cycles were between 840 and 1030^{o}C, which based on published transformation kinetics gave us full transformation at 8 minute cycles (see section 2.2). The same series of samples that was tested isothermally was also tested in a cycled anneal and the results can be found in figure 4.6. The same trend for higher initial porosity and backfill pressure giving faster foaming holds true.

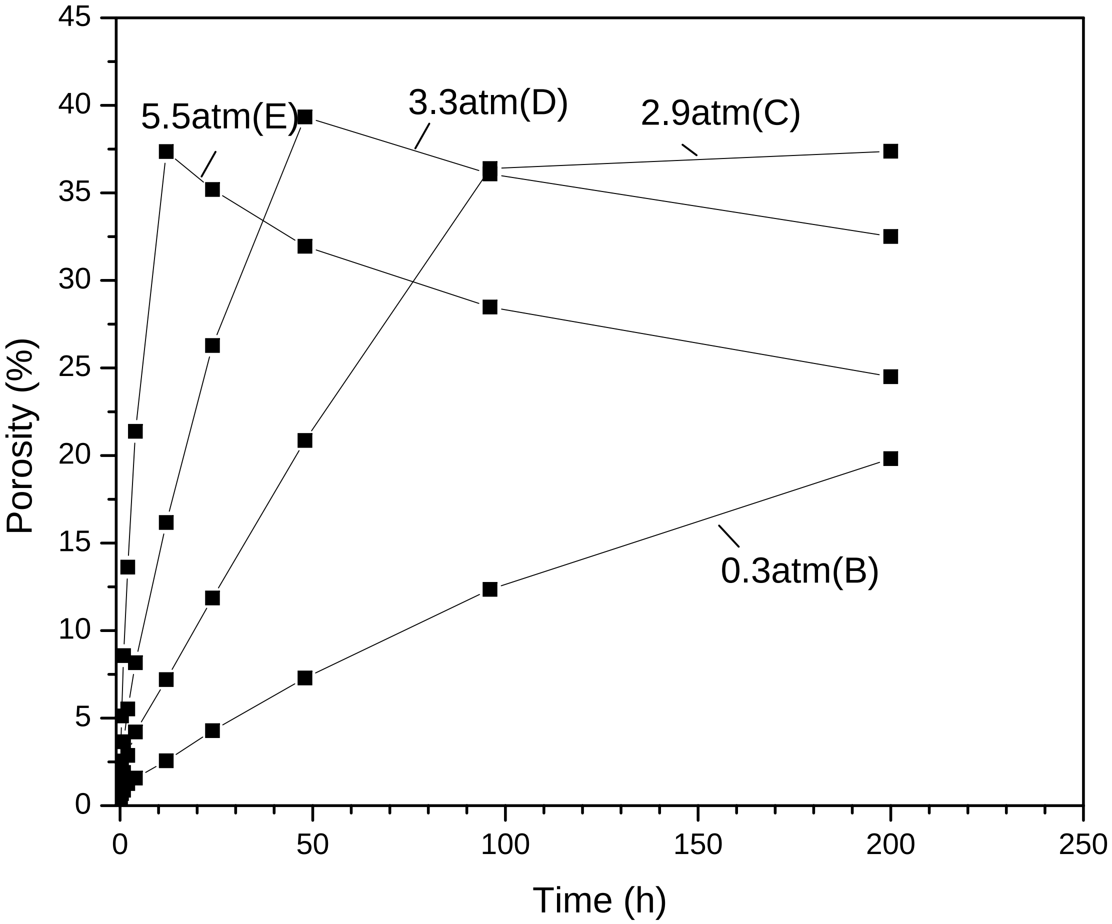

Figure 4.6. Porosity evolution for Ti-6Al-4V cycled between 840 and 1030^{o}C, with different backfill pressures.

The two foaming conditions are compared in figure 4.7, which shows the highest and lowest pressure samples (E and B, respectively) both isothermally (1030^{o}C) and thermally cycled (840 to 1030^{o}C) on the same graph. It can be easily seen that thermally cycling gives higher peak porosity as well as significantly faster foaming to peak porosity. For the initial expansion there is little difference in the expansion of the samples, as the internal pressure is high and the standard power-law creep is fast. As the pores grow the internal

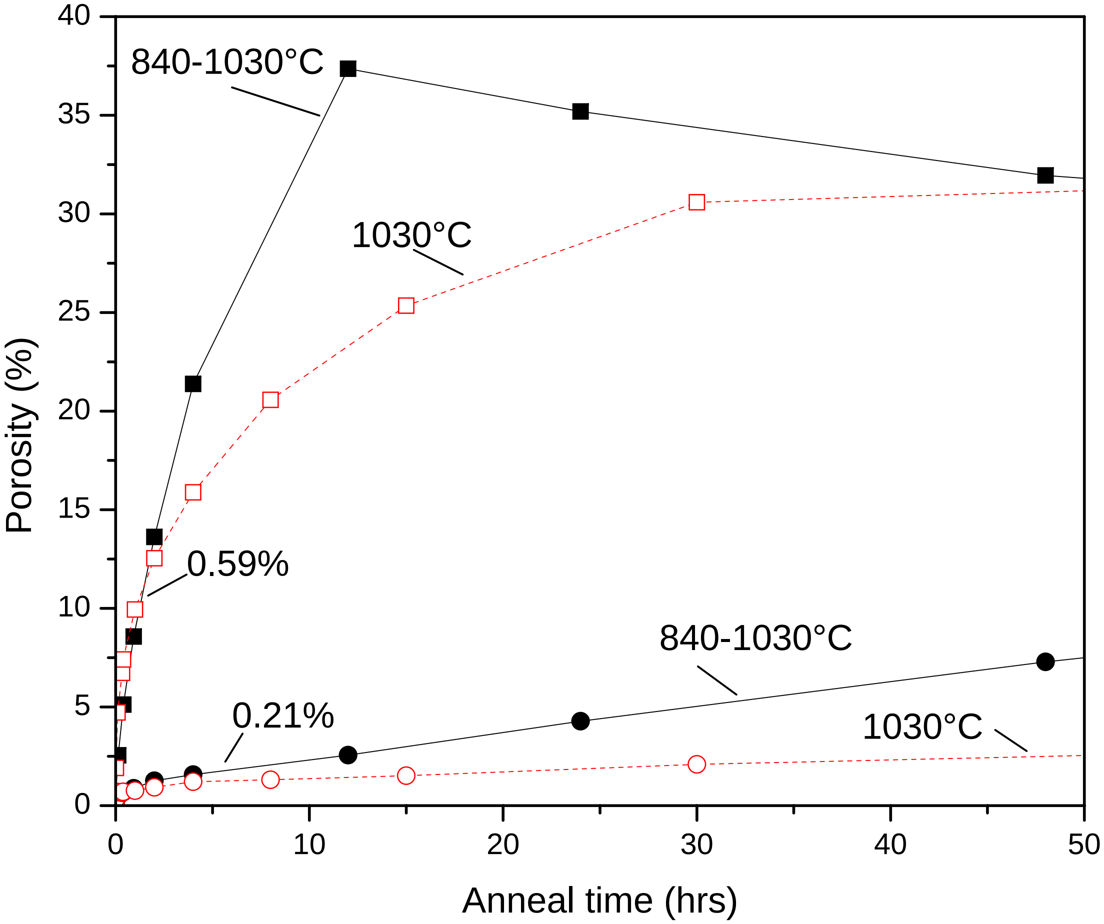

Figure 4.7. Comparision of foaming for thermally cycled Ti-6Al-4V (840 and 1030^{o}C) and isothermal foaming (1030^{o}C) for the highest and lowest backfill pressures.

pressure drops off rapidly. In the low pressure regime the superplastic creep in each cycle becomes the dominant deformation mechanism.

This study is the first in which there was a large enough initial porosity to foam a sample isothermally until the pores percolated and connected to the surface. In the thermally cycled case, there was a higher total porosity at surface connection than the isothermal study for the highest porosity sample. Superplasticty allows very high strains so it is not surprising that the superplastic samples should connect later, allowing more growth of porosity. Due to sintering after the loss of argon, there is never a point at which there is 100% open porosity. Figure 4.8 shows the evolution of the ratio of closed porosity to the total porosity. All of the foaming proceeds in the same general manner. First, there is a growth section where the isolated pores grow and porosity increases. Next the pores start to connect to each other and then to the surface introducing open porosity. From there the porosity closes back off and starts to sinter, reducing overall porosity.

For the thermally cycled samples pores connecting could start as low as 22%, but from sample C it is expected that it is a faster cascade type process that occurs around the terminal porosity of 35%. The walls of the higher porosity thermally cycled samples should be thinner based on geometric considerations. In the case of connecting pores, if there are two pores with a very thin wall separating them and one connects to the surface the change in pressure could cause the second pore's wall to break, leading to a rapid chain that releases a large portion of the gas quickly. In the isothermal case there are thicker walls holding nearly the same pressure which can lead to a slower gas release.

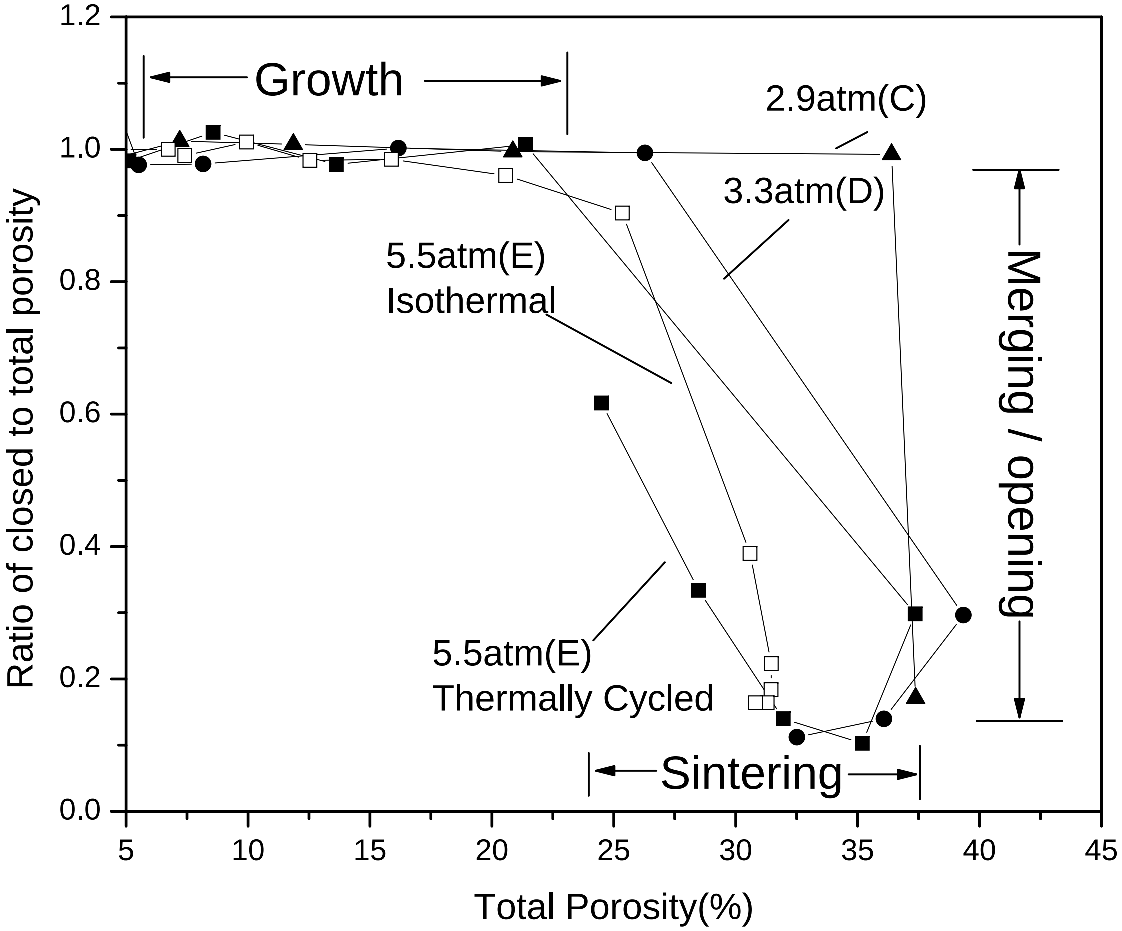

Figure 4.8. Opening of the porosity as a function of the total porosity showing growth, connecting and opening and finally sintering.

4.1.2. Metallography

A series of images were taken in different stages in the foaming process using sample Ar-1 with 0.59% initial porosity. The first set of images were taken at different points in the thermal cycled curve. Figure 4.9 shows four different samples at differing stages of expansion. Figure 4.10 shows a similar four SEM images from isothermally aged samples. For both images, the as-HIP porosity is only 0.54%.

The three high pressure Ti-6Al-4V samples were foamed to around 10% porosity, and the lower pressure sample was foamed to 19% for image analysis. The porosity distributions were found and plotted in figure 4.11.

In both of the melographic series there is growth of the pores. In the thermally cycled samles there was much higher final porosity at the point where the pores started to connect. In both cases at the highest porosities the previous powder particles can be loosely identified, implying that there is some amount of clustering.

One other important result was that by foaming a large billet at once very high final porosities were achieved. A sample 4 cm in diameter, and 2 cm tall of Ti-6Al-4V with 0.41% initial porosity was foamed to a total porosity of 52.5% after 180 hours of thermal cycle foaming (8 minutes per cycle from 890-1030 C). A 1 cm cube sub-sample cut from the billet had a total porosity of 52.6% with 14.2% closed porosity. Figure 4.12 shows the foamed billet. The final porosity was much larger as compared to the fully foamed 1 cm cube which had only 42% total porosity. This shows the effect of frustrating the pore connection to the surface by significantly decreasing the surface to volume ratio. The fully foamed 1cm cube had a surface to volume ration of 6 cm^2/cm^3, while the foamed billet had 1.6 cm^2/cm^3.

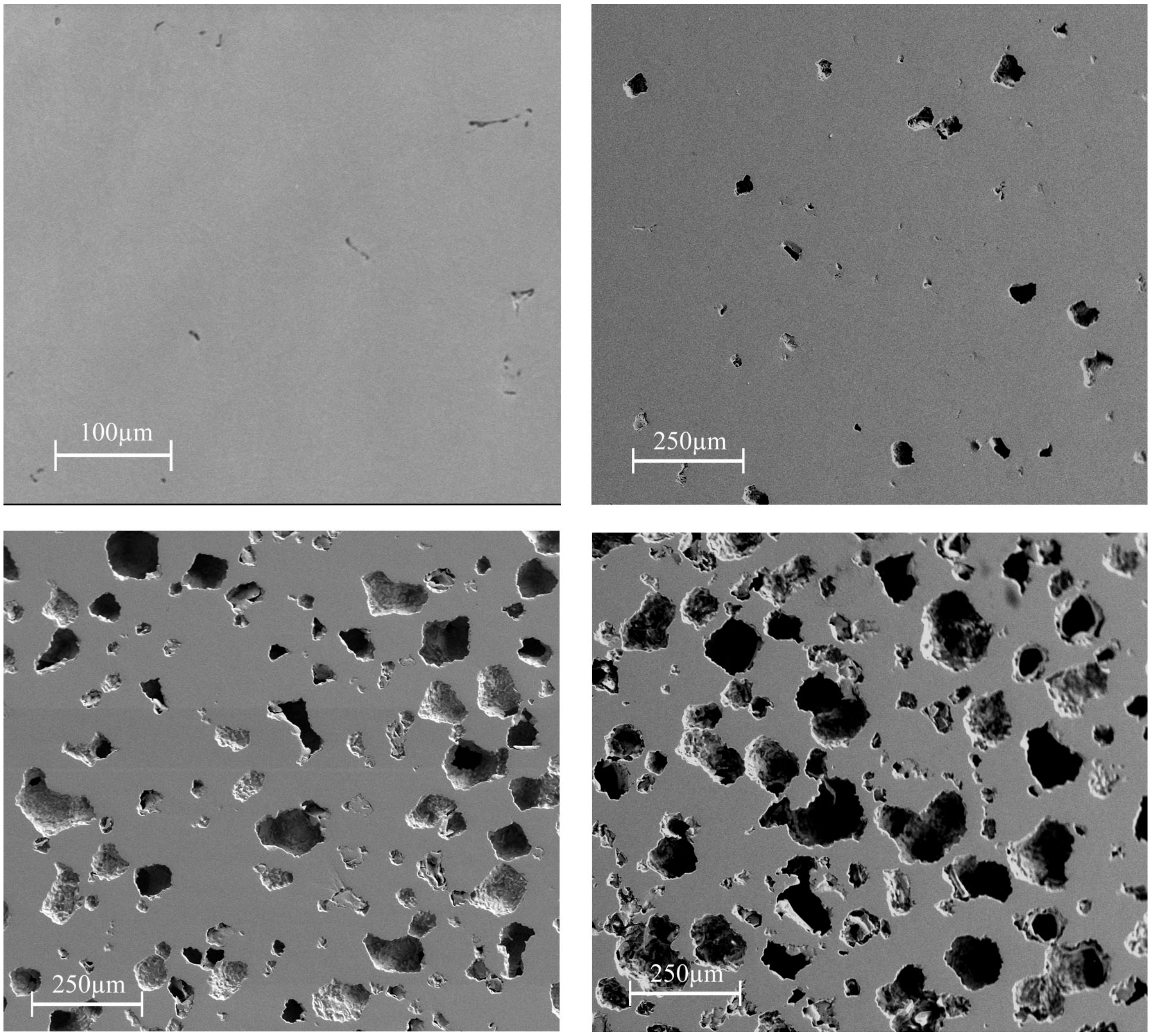

Figure 4.9. Ti-6Al-4V, 0.59% initial porosity samples showing as-HIP state, 8% porosity at 56 minutes, 24% porosity at 3.5 hours and 41% porosity at 10 hours of thermal cycling.

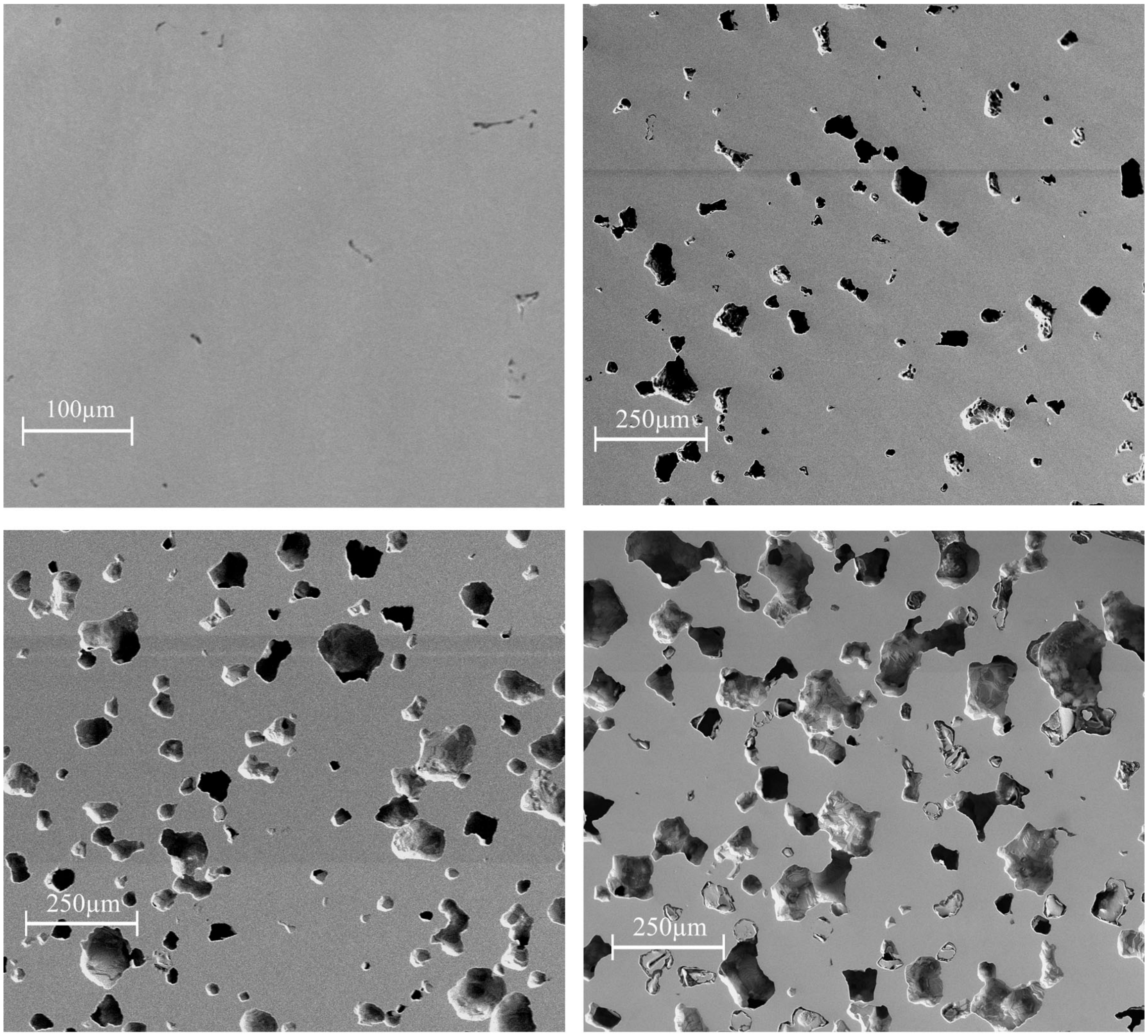

Figure 4.10. Ti-6Al-4V, 0.59% initial porosity samples showing as-HIP state, 9% porosity at 60 minutes, 21% porosity at 8 hours and 29% porosity at 60 hours of isothermal annealing at 1030^{o}C.

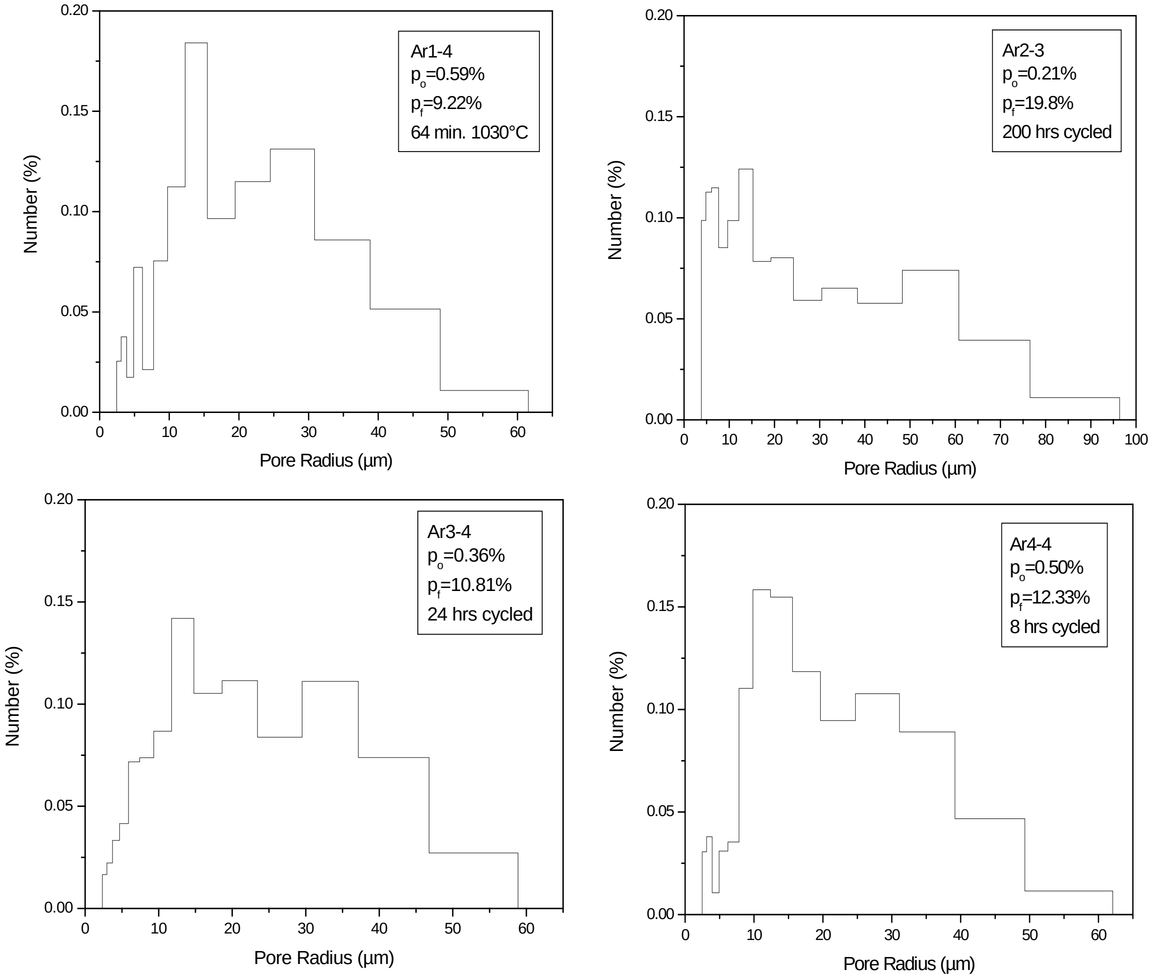

Figure 4.11. Pore size distributions for each of the four Ti-6Al-4V pressures tested.

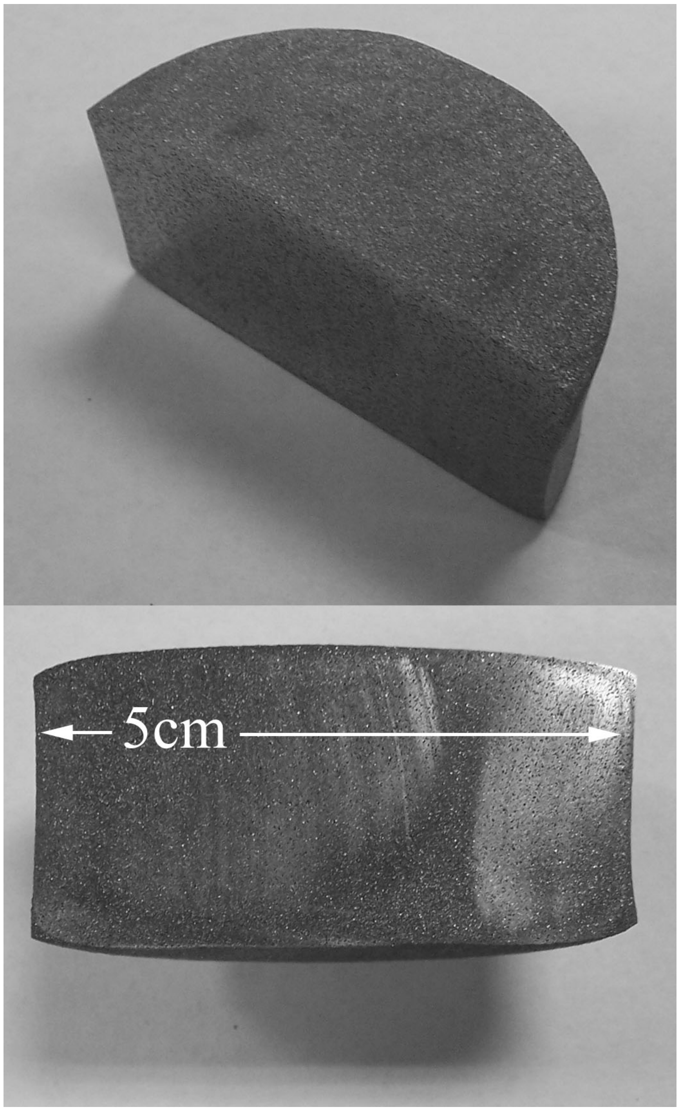

Figure 4.12. Ti-6Al-4V foamed to 53.5% porosity for use in animal studies.

4.1.3. Mechanical Properties

For applications in bone replacement it is desirable to match the Young's modulus of the bone itself. This prevents stress shielding and bone desorption, and leads to longer implant life [**1**, **62**]. For this reason, a good first-order mechanical test for the usefulness of a foam is its ultrasonic elastic response. As porosity increases, the modulus drops with the square of relative density. The goal is to be near the Young's modulus of bone which is 10-20 GPa depending on bone type and location [**62**].

In order to determine the elastic properties, transmission ultrasonic tests were performed on both the isothermally aged as well as the thermally cycled samples using the methods described in section 3.5. A plot of all of the results can be seen in figure 4.13.

The results were fit to two well-known analytical equations. The first was the Gibson-Ashby relationship [**20**], and the second was an alteration to the Gibson-Ashby relationship made by Wanner where the exponent is allowed to change [**63**]. The original equation as well as the alteration are:

$$\frac{E}{E_o} = \left(\frac{\rho}{\rho_o}\right)^2 \tag{4.1}$$

$$\frac{E}{E_o} = \left(\frac{\rho}{\rho_o}\right)^\eta \tag{4.2}$$

where E is the measured foam Young's modulus, E_o is the Young's modulus of the fully dense material, ρ is the measured density, ρ_o is the bulk density, and η is the exponent

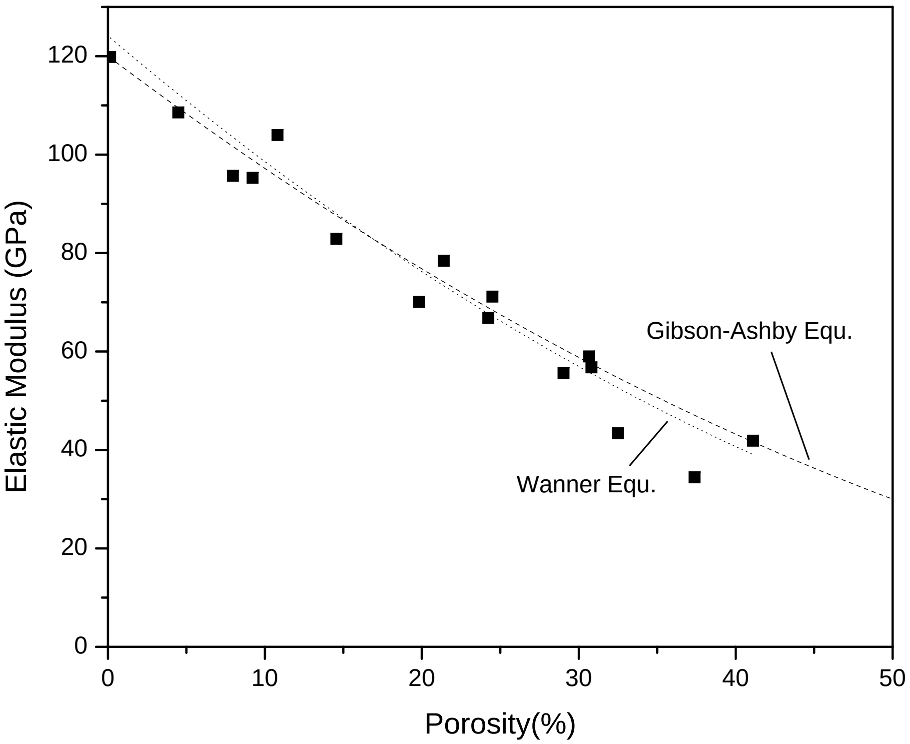

Figure 4.13. Ultrasonic Young's modulus measurements as a function of porosity, dashed lines indicate Gibson-Ashby [1] model, dotted line indicates Wanner model [63].

used to account for shape and orientation effects. Both equations fit well, since η was found to be 2.18. Furthermore both find the modulus of bulk Ti-6Al-4V to be between 120 and 125GPa which is well within the range expected for Ti-6Al-4V [**64**].

All of the foams produced have a higher Young's modulus than would be ideal for an exact match with bone (10-20 GPa [**62**]). If the equations that describe the data can be extrapolated, achieving the high Young's modulus bone (20 GPa) would require a porosity of around 60%. Even though we are not able to archive the specific target Young's modulus, when compared to fully dense titanium that is currently used, the addition of porosity offers a significant improvement.

4.2. Nickel Titanium

4.2.1. Creep Properties of Bulk NiTi

4.2.1.1. Introduction. In 1968, Mukherjee [**65**] was the first to measure the creep properties of NiTi. The tensile flow stress was measured over six temperatures spanning 700-1000C (corresponding to homologous temperatures of 0.61-0.80, using the melting point of 1310C for equiatomic NiTi) at three constant strain rates spanning two orders of magnitude. The stress exponent and activation energy for creep were discussed in the light of then-recent theories of viscous creep. Three decades later, Kato et al. [**66**] published an extensive study of tensile creep in NiTi wires between 628 and 888C. Both constant creep rate and constant load experiments were performed. The creep exponent was determined using two different methods: first by performing strain-rate jumps and measuring flow stress, second by using the reduction in gauge area occurring during deformation to access many different stresses in a single constant-load experiment. The former, more standard method gave a stress exponent more than twice that of the latter method. Eggeler and coworkers [**67**, **68**] published two studies where tensile creep was measured at lower temperatures (470-560^{o}C), at which Ti_3Ni_4 precipitates formed during heating to the test temperature and coarsened during creep testing. The evolving microstructure resulted in two sets of results: an initial minimum creep rate which was up to two orders of magnitude slower than the subsequent plateau (steady-state) creep rates. The respective stress exponents and activation energies were also different. These authors studied the dislocation structure developed after creep deformation, and the effect of prior creep upon the

Investigation	*Year*	*Sample Diam. (mm)*	*Ni Content (at. %)*	*Processing*
Mukherjee [**65**]	1968	6.35	50.6	Hot-swagedrod, annealed at 1000^{o}C
Kato [**66**]	1999	0.9	49.5,50,50.5	Drawn wires, annealed at 900^{o}C
Eggeler [**68**]	2002	13	50.7	Solutionized at 850^{o}C, percipitation and coarsening during creep
Kobus [**67**]	2002	-	50.7	Annealed at 500-560^{o}C
Lexcellent [**69**]	2005	18.5	50.0	Hot drawn bars
Present Study	2007	12.7	50.8	Bars, annealed at 950-1100^{o}C

Table 4.1. Summery of prior and present study NiTi sample preparation.

Investigation	*Temp* (^oC	*Strain Rate* (s^{-1})	*Stress (MPa)*	*n(-)*	*Q* ($\frac{kJ}{mol}$)	*Grain size* (μ m)
Mukherjee [**65**]	700-1000	$6{\cdot}10^{-5}$ - $6{\cdot}10^{-3}$	6-178	3±0.2	251±13	-
Kato [**66**]	628-888	$1{\cdot}10^{-5}$ - $2{\cdot}10^{-2}$	11-81	1 and 5.9 (2.5±0.2*)	230-253	15
Eggeler [**68**]	470-530	$2{\cdot}10^{-9}$ - $8{\cdot}10^{-6}$	90-150	2	334	35
Kobus [**67**]	500-560	$2{\cdot}10^{-7}$ - $3{\cdot}10^{-5}$	120-180	5	421	-
Lexcellent [**69**]	597-897	$3{\cdot}10^{-3}$ - $4{\cdot}10^{-2}$	10-35	3	222±30	-
Present Study	950-1100	$1{\cdot}10^{-6}$ - $1{\cdot}10^{-5}$	4.7-11	2.7±0.2	155±14	48-140

* Single sample method

Table 4.2. Summary of creep conditions and creep parameters measured in prior and present studies.

phase-transformation of NiTi near ambient temperature. Finally, in a recent study, Lexcellent et al. [**69**] measured the creep rate of NiTi between 600 and 900^{o}C and obtained an activation energy higher than the tracer diffusivity activation energy of Ni in NiTi. This information is summarizied in tables 4.1 and 4.2.

In the present study, we measure the creep rate of near-equiatomic NiTi for a so-far unexplored combination of high temperatures (950-1100^{o}C) and low stresses (3-11 MPa). Our study is also the first to use compression and to report grain size before and after creep deformation. The results are compared to those of the previous NiTi creep studies reviewed above.

4.2.1.2. Experimental Method. A nickel-rich, superelastic NiTi rod (50.8 at.% Ni, 12.7 mm diameter, produced by Nitinol Devices and Components) was cut into 25.4 mm high cylindrical specimens whose ends were ground flat and parallel. Compressive creep experiments were performed under constant load in vacuum (0.5 mTorr residual pressure) in a hydraulic testing machine. The samples were placed in a WC-Co creep cage, consisting of a sleeve and two pistons, with Mo foils as spacers. Each sample was heated to a particular temperature (950, 1000, 1050 or 1100^{o}C) at a rate of 10^{o}C/min and annealed for 1 h. The sample was then subjected to a constant stress until a constant strain rate was achieved. This procedure was repeated in a series of increasing stress values spanning 3-11 MPa until a total strain of 12% had been accumulated.

4.2.1.3. Results and Discussion. The secondary strain rates , which were achieved after a short primary creep period, are plotted as a function of stress σ in Figure 4.14 for the four temperatures T studied here. The power-law creep equation:

$$\dot{\epsilon} = A\sigma^n exp\left(-\frac{Q}{RT}\right) \tag{4.3}$$

where R is the gas constant, was used to fit the creep data simultaneously for the Dorn constant A, stress exponent n and activation energy Q. The overall best-fit lines (with

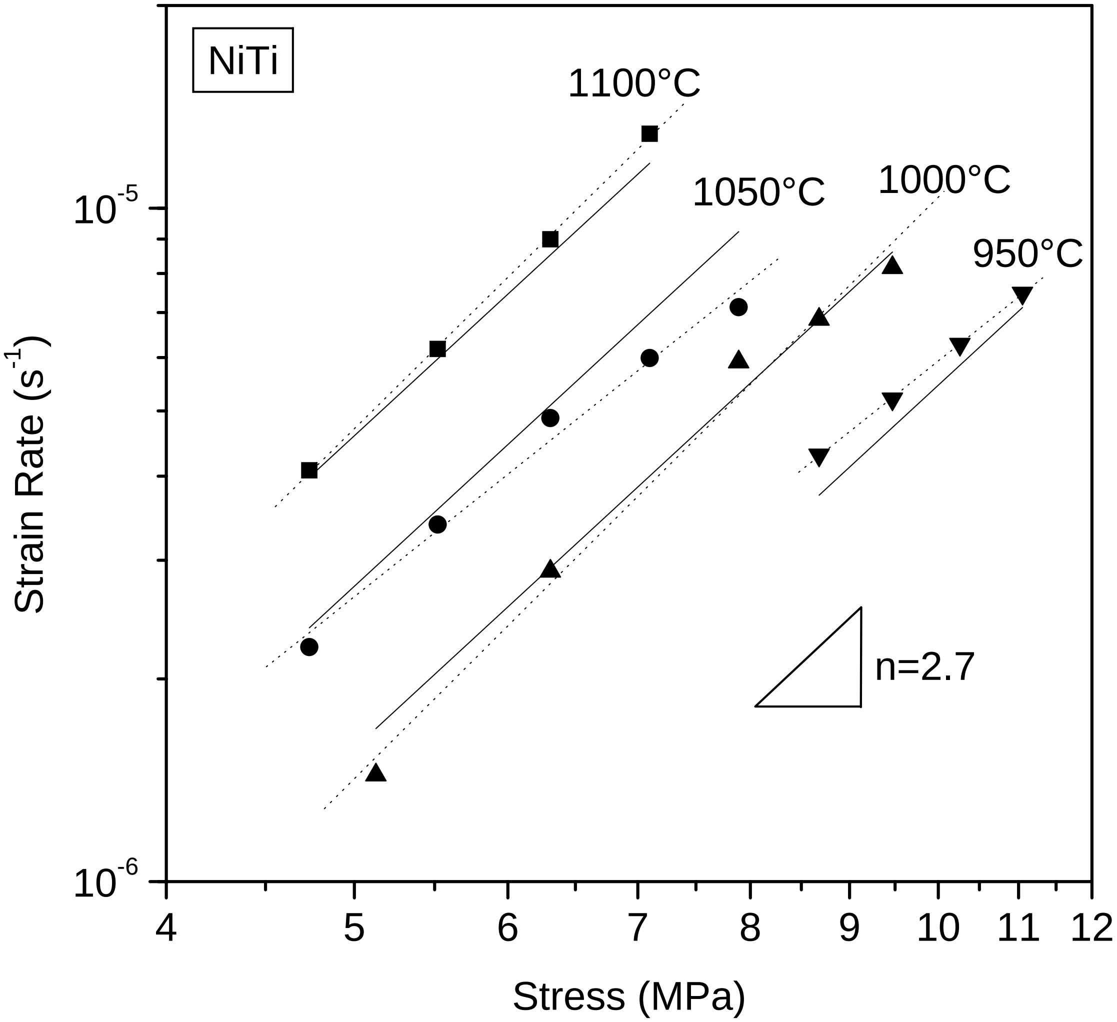

Figure 4.14. Plot of compressive strain rate vs. compressive stress for NiTi measured in the present study, showing best-fit for each temperature (dashed lines) and overall best-fit for all four temperatures (solid lines) with n=2.7.

A=0.05±0.04 MPa^{-n}s^{-1}, n=2.66±0.23 and Q=155±14 kJ/mol) are shown in Fig. 4.14, together with best-fit lines for each temperature, with n varying between 2.3 and 2.9.

Metallography was performed on diamond-polished cross-sections which were etched with a modified Kroll's reagent (5% HNO3, 10% HF, balance water). Grain boundaries were imaged with an optical microscope and standard line analysis (ASTM E112) was used to determine the average grain size which was found to be 48 ± 5 μm for as-received NiTi, and 140 ± 13 μm for a sample which had been crept for 12 h at 1050^{o}C. Figure 4.15 summarizes the creep data from the current study (Fig. 4.14) and from the five previous creep studies reviewed above. In some cases (e.g. Lexcellent et al. [**69**]), the individual creep data leading to values of n or Q were not reported by the authors and are thus not plotted in Fig. 4.15. The stress in Fig. 4.15 is not normalized by the shear modulus, since a study by Hasiguti and Iwasaki [**70**] has shown that the shear modulus of NiTi remains near-constant up to 800 ^{o}C, reaching a maximum value at 550^{o}C (higher by only 20% than the room temperature value) and then decreasing slowly (with the shear modulus at 800^{o}C being nearly identical to the room temperature value).

It is apparent from Fig. 4.15 that discrepancies exist between the six studies, preventing the determination of overall values for A, n and Q. The two studies by Eggeler and coworkers [**67**, **68**] examined NiTi containing fine precipitates whose presence affect A, as well as Q and n if a threshold stress is present [**71**]. The effect of precipitate growth at low temperature is visible in the vast difference observed between the initial minimum creep rates and the subsequent plateau (steady-state) creep rates, as discussed in detail by Eggeler et al. [**68**] Thus, these two studies [**67**, **68**] cannot be compared to the other four creep studies performed at higher temperature, for which it can be safely assumed that precipitates are dissolved or coarsened to the point that they do not significantly affect creep rates.

These four high-temperature studies remain however inconsistent with each other. In particular, it is apparent that three of the studies (Refs. [**65**, **69**] and the present study)

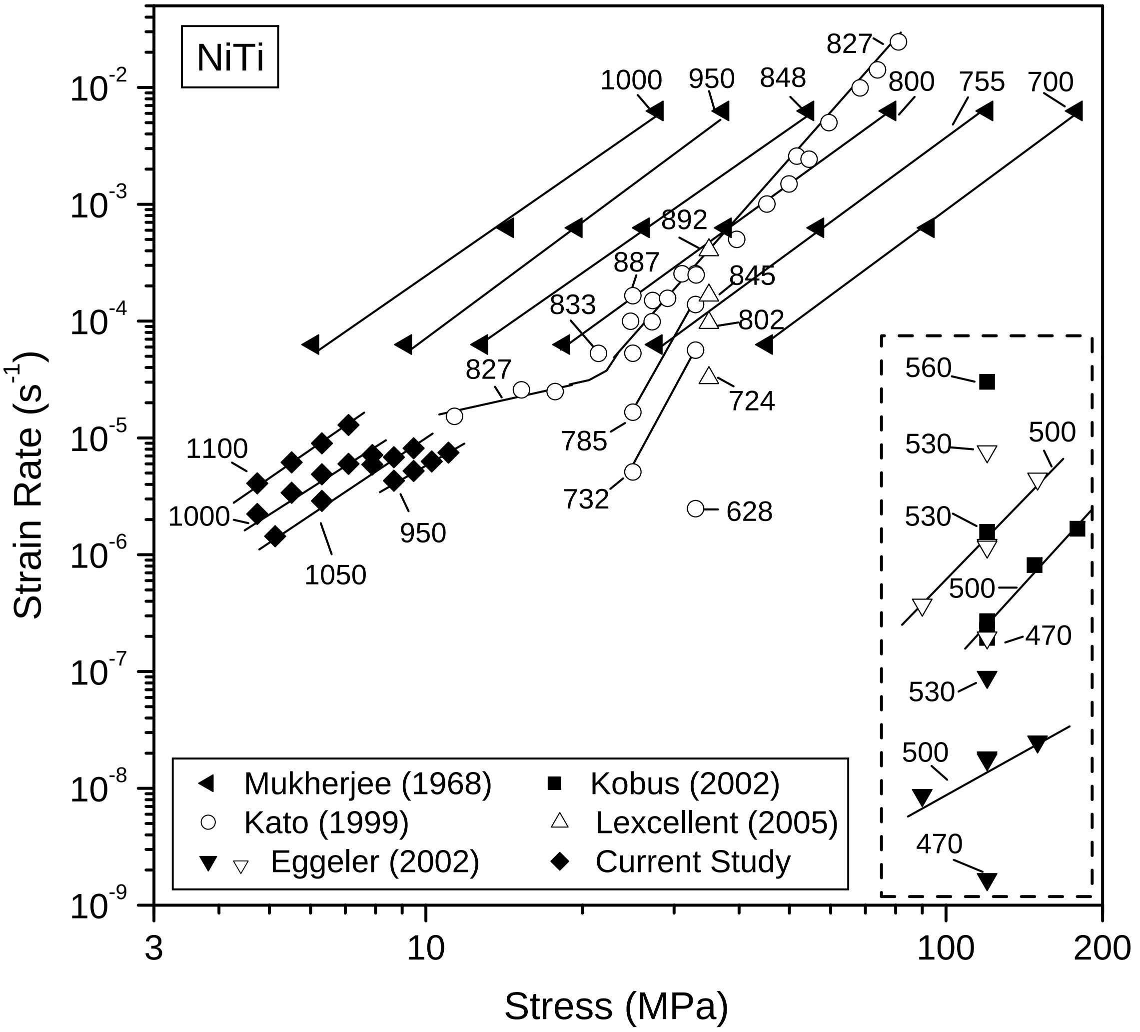

Figure 4.15. Plot of strain rate vs. stress for NiTi summarizing present study and previous literature data. Data within the dashed box is for NiTi with Ti_3Ni_4 precipitates. Steady- state and minimum rates are shown with different symbols for the study by Eggeler et al. [68]. Test temperatures are given in ^{o}C.

report a stress exponent of about 3, while the fourth by Kato et al. [**66**] lists values of n=2.5 or 5.9, depending on the technique used (denoted by an asterisk in table 4.2).

The latter value was obtained at a single temperature (827^{o}C) for three slightly different compositions. Also, considering the activation energy, the present study finds a value (Q=155 kJ/mol) significantly lower than those of the other three studies [**65**,**66**,**69**] (Q 250 kJ/mol, as summarized in Table 4.2). Some possible reasons for these discrepancies in n and Q values among the four high-temperature studies are discussed below. A first possible reason is that all previous studies used tensile stresses, whereas the current tests were performed under compression. Two possible sources for tension/compression asymmetries exist. First, cavitation can occur in tension but usually not in compression, thus lowering the cross-sectional area and producing stress concentrations that lead to higher strain rates and higher sensitivity to both stress and temperature (i.e., higher A, n and Q) [**71**]. Second, some intermetallics are known to show an intrinsic tension/compression asymmetry even in the absence of cavitation, as shown by NiAl (with the same B2 crystal structure as NiTi) where both n and Q are different in tension and compression [**72**]. This effect could be examined in NiTi by carrying out tensile and compressive tests on specimens produced from the same ingot.

A second possible source for discrepancy is variation in grain size between studies. At a given temperature, fine-grained NiTi may exhibit diffusional creep with lower n and Q than coarse-grained NiTi creeping by dislocation motion (climb or glide). Among the four high-temperature studies, only Kato et al. [**66**] and the present study provide initial grain sizes. Kato et al. report an initial grain size of 15 μm, which is quite small for a metal, and may be responsible for the three data points at their lowest stress showing n=1 (Fig. 2), typical of diffusional creep. Kato et al. however do not report the grain size after creep testing. In our experiments, the grain size increased from 48 μm prior to testing to 140 μm after testing, indicative of moderate grain growth which may have occurred during the 1 h. anneal period or during testing. The discrepancy between our results and those of Mukherjee (e.g., extrapolating our data at 1000^{o}C to higher strain rates produces an overlap with his data at 755 ^{o}C) may be due to anomalously fast creep in Mukherjee's experiment due to small grains. This explanation is speculative since Mukherjee did not report a grain size, but small grain size in his material is credible since it had been hot-swaged prior to testing, and was thus very likely recrystallized [**65**]. A further confounding effect is the value of the stress exponent n=3, which may represent viscous glide of dislocations in one case, or transition between diffusional creep (n=1-2) and dislocation creep (n=4-6) in another. A future study on NiTi creep would have to use coarse-grained samples with a grain size that does not evolve during the experiment.

Third, it is possible that deviation in the stoichiometric NiTi composition may affect creep response, even in the absence of precipitates, through concentration-dependence of the diffusion coefficient (as reported in NiAl [**73**] with the same B2 structure as NiTi) or through decrease of the solidus temperature. Kato et al. [**66**] showed that creep rates at 827 ^{o}C were faster by a (relatively small) factor of two for equiatomic NiTi, as compared to Ni-49.5%Ti and Ni-50.5%Ti. Here too, a systematic study of NiTi composition on creep behavior would be needed.

Fourth, some intermetallics (e.g., B2-FeAl [**74**]) show a transition between low-temperature and high-temperature creep behavior, characterized by creep activation energy on the order of the activation energy for bulk diffusion at high temperatures, and much higher values at lower temperatures. Our study, performed at the highest temperatures, also exhibited the lowest activation energy (which is equal to that for Ni diffusion in NiTi [**69**]) and may thus represent high-temperature creep behavior.

Finally, the presence of texture may also have affected the various creep rates of NiTi compiled in Figure 2, as reported in B2-NiAl [**75**]. All NiTi specimens were subjected to various thermo-mechanical processes (i.e., swaging and drawing, Table 4.1) expected to produce texture, which may have been retained partially or fully despite the subsequent heat-treatment and creep testing. A future study would have to test texture-free materials with equiaxed grains to ascertain the true creep behavior of NiTi.

In conclusion, nickel-rich, near equiatomic NiTi with grain size 48-140 μm was deformed in compression between 950 and 1100^{o}C over a stress range of 3-11 MPa, resulting in strain rate spanning $1.4{\cdot}10^{-6}$-$1.3{\cdot}10^{-5}$ s^{-1}. Best-fit of the creep data to a power-law equation results in a stress exponent $n=2.7\pm0.2$ and an activation energy $Q=155\pm14$ kJ/mol. Only five previous studies on the creep of NiTi exist, and it is impossible to harmonize data among the different studies to achieve a single constitutive power-law equation.

This is most probably due to additional variables affecting creep of NiTi, including tension/compression asymmetry, presence of precipitates, deviation from stoichiometry, presence of texture, and dominance of different creep mechanisms (i.e., diffusional and dislocation creep) due to different grain size and testing temperatures.

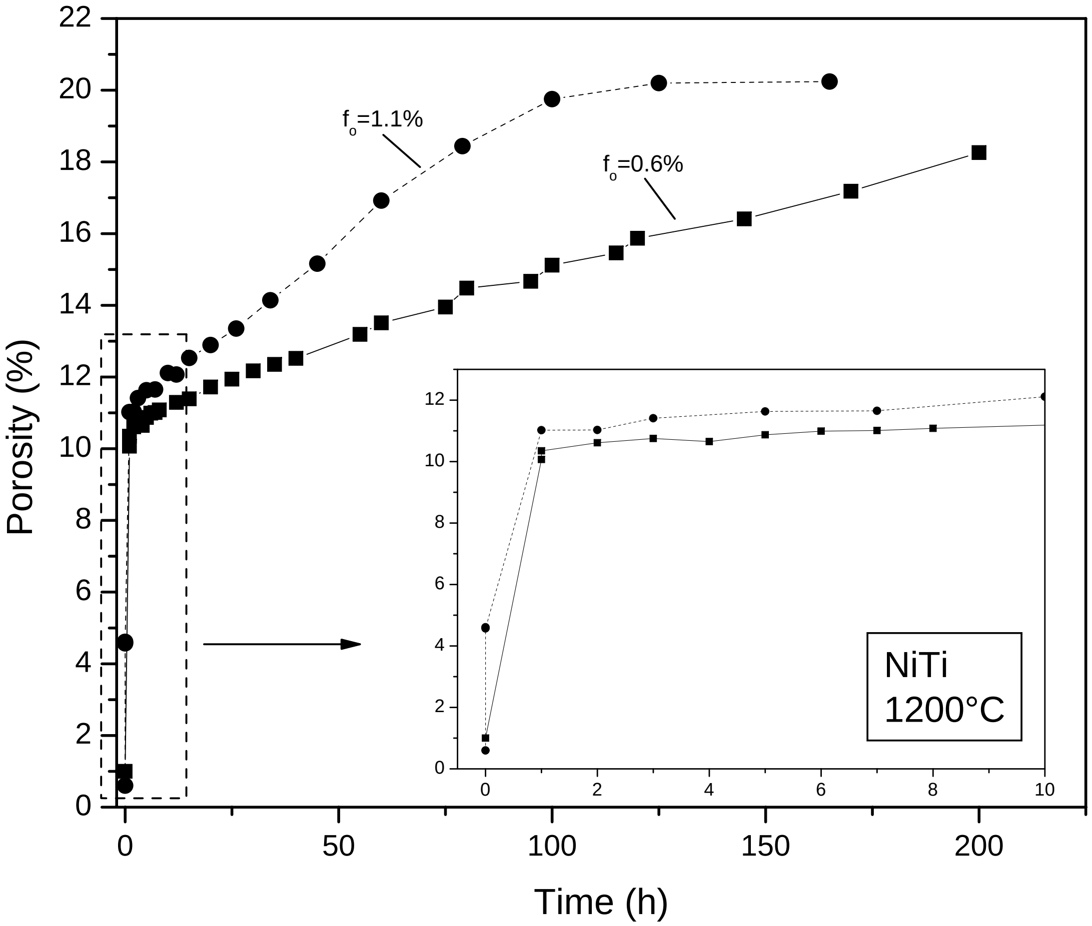

Figure 4.16. Foaming of NiTi at 1200^{o}C, with inset showing rapid initial growth.

4.2.2. NiTi Isothermal Foaming

Porous NiTi performs were first created through the standard can and HIP method described in section 3.4. Initially high temperatures were used to overcome the natural creep resistance of the NiTi. Work performed in collaboration with Christian Greiner is shown in figure 4.16. It shows a fast initial increase in porosity then a long slow tail. At no time was measurable open porosity found in the sample.

It was hypothesized that the slow porosity growth was due to the higher creep resistance of NiTi and therefore the alternate method for adding argon was created (see section 3.4 for details). This new method allowed much higher possible backfill pressures, and correspondingly larger initial porosities. Figure 4.17 shows this relationship, and includes the samples created with the old, which were HIP'ed at a lower pressure (samples A and B).

In order to put the previous low pressure work in context, initial experiments on the new high pressure samples (5,7 and 8 from figure 4.17 were carried out at 1150^{o}C. The foaming of these samples happened so rapidly that, after only 5 minutes the samples were nearly fully open and showed between 8% and 12% total porosity. When put back in for another 10 minutes at 1150^{o}C, there was significant sintering in all of the samples which closed off the porosity. A third run for 15 minutes sintered nearly all of the porosity closed. This initial rapid growth in porosity was previously seen in figure 4.16, but it was expected that the porosity had not connected to the surface due to no measurable open porosity. Instead it is now believed that the the majority of the gas had rapidly expanded and escaped, but sintering closed off the small release openings. Due to size variation there should have been some very small pores that would not have connected to the surface as rapidly, but connected into the old network and re-pressurized the existing pores. The small amount of gas then slowly foamed the structure, and increased the overall porosity (1-200 h in figure 4.16). A schematic diagram of this is seen in figure 4.18.

In order to examine the growth of the pores in more detail, the creep temperature was reduced. High pressure samples were foamed at 900^{o}C. In this case, the expected smooth

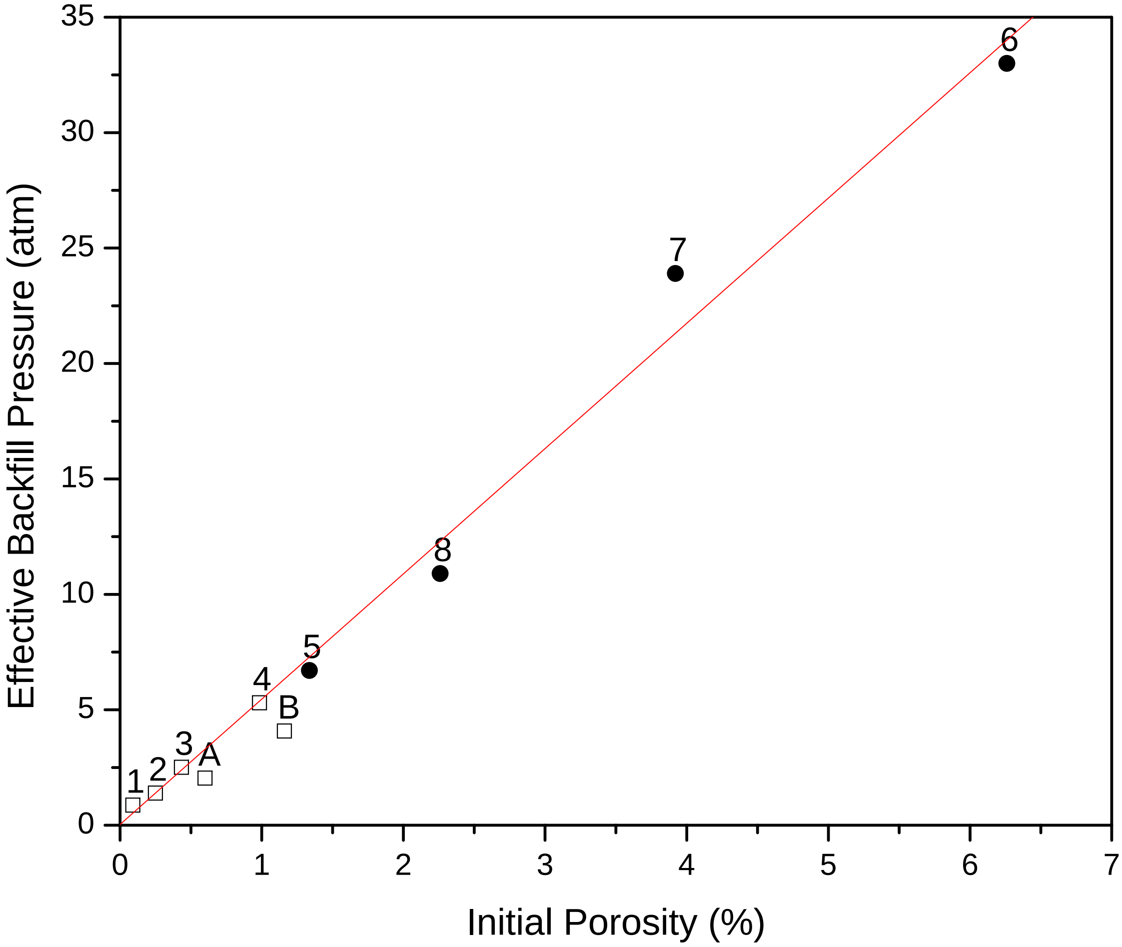

Figure 4.17. The relationship between backfill pressure and initial as-HIP porosity in NiTi. High pressure samples are solid, while samples made using the old method are open. Samples A and B were HIP'ed under lower pressure yielding higher porosity.

growth curve was found, and the porosity did not resinter as quickly or completely. The expansion curves can be seen in figure 4.19.

All of the samples begin to have open porosity around 10% total porosity, and for the samples that fully open there is little to no closed porosity after 14% total porosity. This

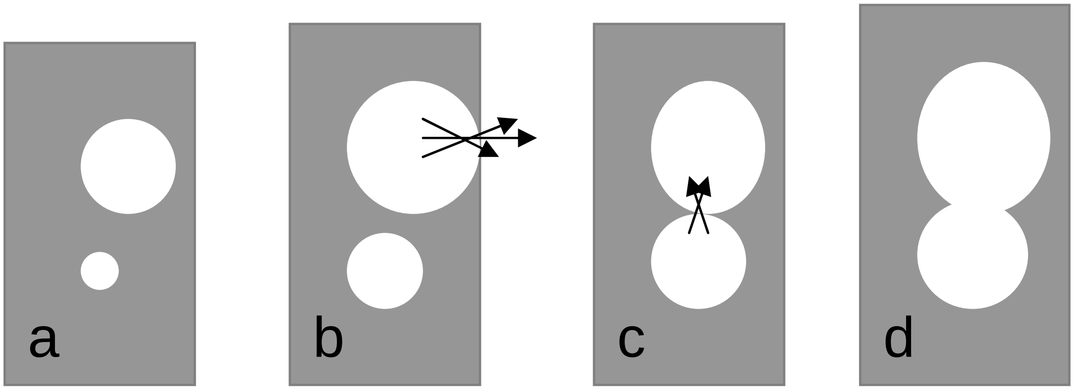

Figure 4.18. Schematic diagram of resintering and re-pressurization in NiTi showing: (a) independent high pressure pores that expand at different rates (b) and connect to the surface losing the gas inside, but are then sintered closed and re-pressurized from gas trapped in smaller pores (c), which then grow together (d).

early connecting to the surface shows that there are significant differences between the titanium foaming shown in section 4.1.1 and NiTi foaming.

Samples were sent to Dr. Jan Frenzel at the Ruhr-Universität in Bochum for chemical analysis to check for contamination caused by the foaming heatings. Three samples that all used the same pre-alloyed NiTi powder were sent and the results can be found in table 4.3. No significant change in the oxygen content was found even after foaming. An increase in carbon contamination was found, but the total amount is small and not expected to be significant. One possible source of carbon contamination is the grease used in density measurements, which may have left residue that would have, upon heating formed small amounts of TiC on the sample surface.

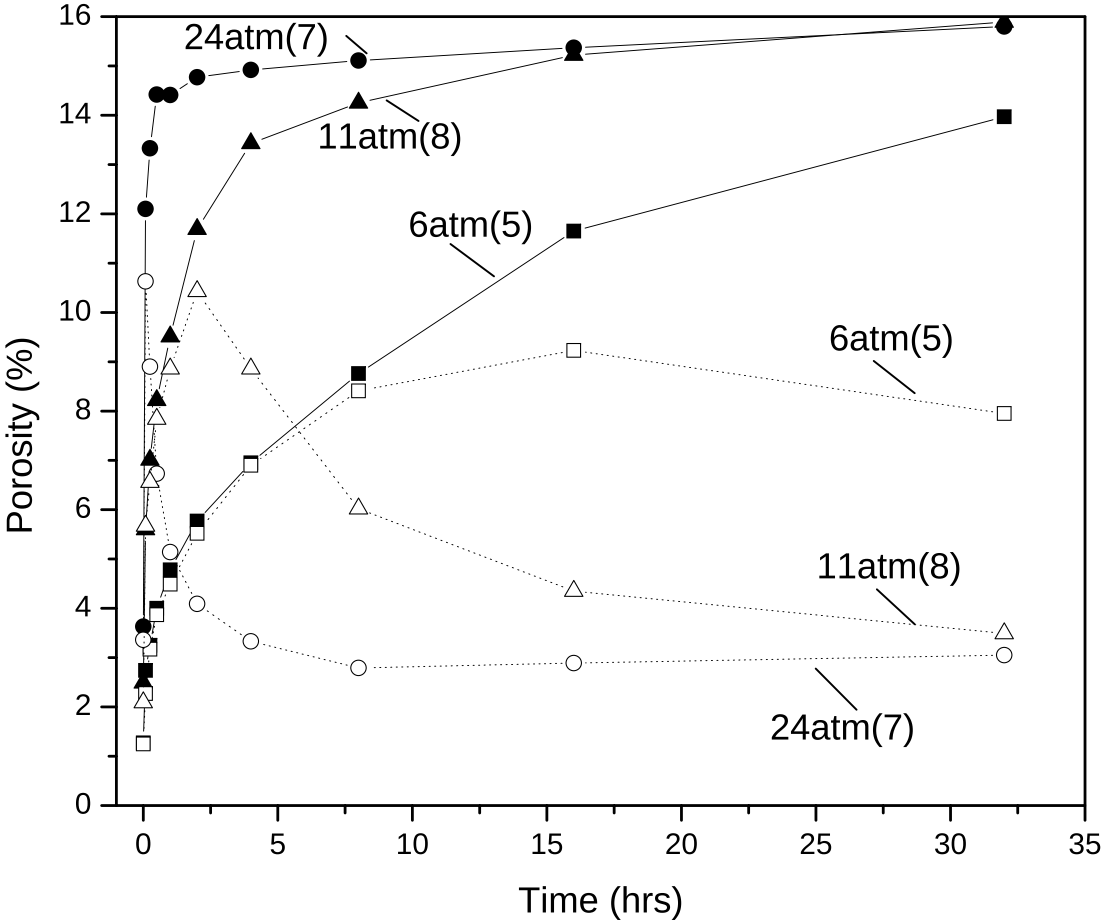

Figure 4.19. Foaming curves for NiTi samples foamed at 900^{o}C, solid lines and symbols represent total porosity, dotted lines and open symbols represent closed porosity.

Sample	*Processing*	*wt% O*	*wt % C*
Pre-alloyed powder	As received powder	0.1	0.003
NiTi Billet	As received after HIP	0.075	0.015
NiTi foamed	47 hours cycled between 600 and 1000^{o}C in vacuum furnace	0.1	0.029

Table 4.3. Chemical analysis of NiTi samples.

4.2.3. Rapid Thermal Cycle Graded Porosity

An attempt was made to use rapid cycling to achieve graded porosity. This process rests on the fact that a sample at the average temperature in a given cycle will creep more slowly than the integrated creep rates over the whole cycle. Calculating the total creep expected over a single cycle, an average creep rate can be determined. This equation is shown below:

$$\bar{\dot{\epsilon}} = \frac{1}{\Delta T} \int_{T_1}^{T_1 + \Delta T} \dot{\epsilon} dT \tag{4.4}$$

where the creep rate is a function of temperature:

$$\dot{\epsilon} = k\sigma^n exp\left(-\frac{Q}{RT}\right) \tag{4.5}$$

The temperature where the isothermal creep rate $\dot{\epsilon}$ is equal to thermally cycled average creep rate $\bar{\dot{\epsilon}}$ is the effective temperature. Due to the exponential increase of creep rate with increasing temperature, the effective temperature is always higher than the average temperature.

By cycling the surface temperature as high as possible, there is a high effective temperature. As the heat diffuses into a medium the amplitude of the cycle drops, lowering the effective temperature. By cycling, a gradient in the effective temperature is set up which can then lead to a porosity gradient. The mathematical analysis used to describe the diffusion of a cyclic temperature gradient is the same equation used for the cyclic heating and cooling of geologic features [**76**]:

$$\Delta T_{depth} = \Delta T_{surface} e^{-y\sqrt{\frac{\omega}{2\kappa}}} \tag{4.6}$$

where y is the depth into the sample, ω is the cycling rate ($\omega = 2\pi f$, where f is the cycle frequency), and κ is the thermal diffusivity. From the above equation, it is easy to see that to maximize the graded porosity it helps to have fast cycles, large samples, and a material with low thermal diffusivity.

The first attempt using this method was on titanium, in hopes that the phase change would magnify the temperature gradient and influence the superplastic expansion. A 17mm tall, 5.75mm diameter sample with 0.5% initial porosity, was put in the furnace with the bottom 14mm in a block of alumina-silica insulation which acted as a thermal barrier. The sample was then thermally cycled as rapidly as the vacuum furnace was able: a sample temperature measured at the top of the sample vs. time cycle can be found in figure 4.20. The results after 50 cycles and 86 minutes showed that the top and bottom had the same porosity of around 2%, implying that the cycling had no effect. Initially this was quite surprising as the top would be expected to be around 7-8% porous while the bottom less than 3%. The diffusion based kinetics of the phase transformation had, like an ice cube, acted as a thermal sink and prevented a local phase transition. Furthermore by inhibiting the phase transition the sample was kept in the alpha, for much of the cycle and therefore little to no expansion was found.

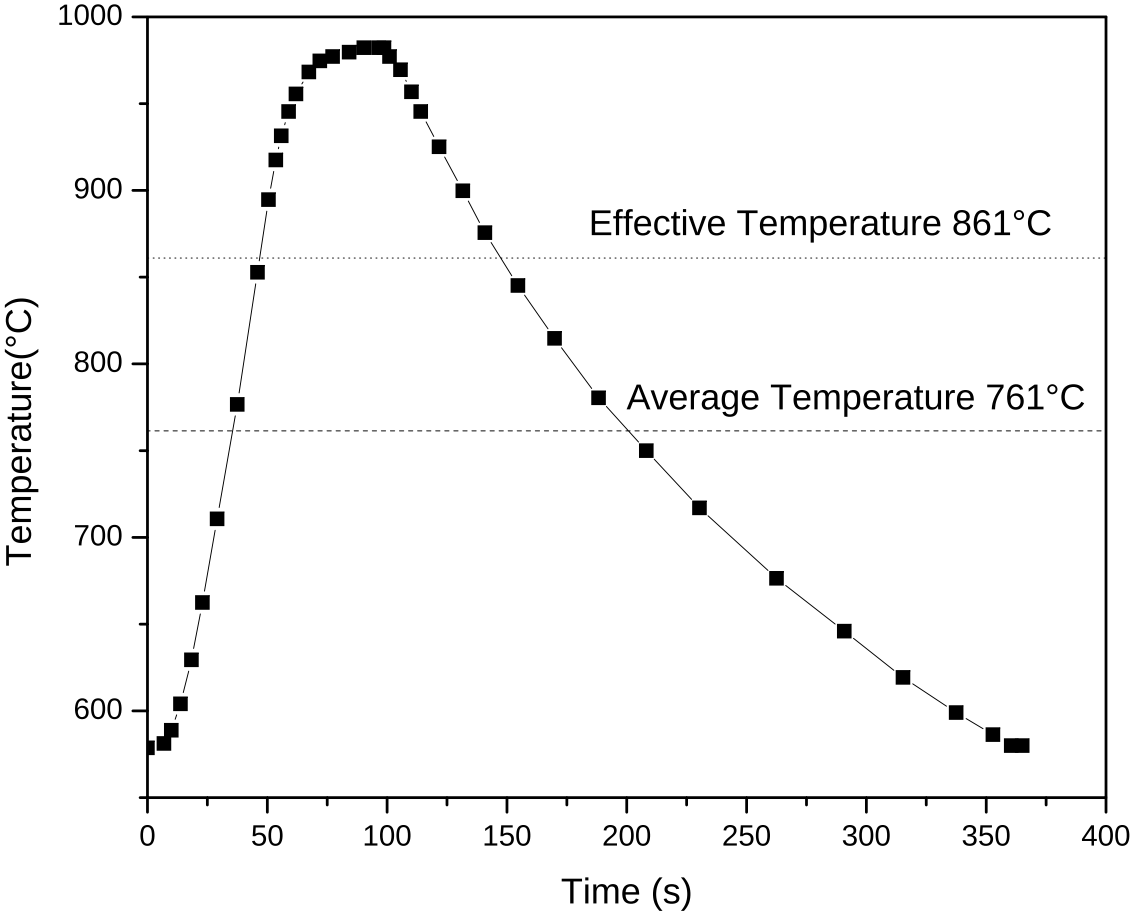

Figure 4.20. Temperature profile of a rapid cycle used in creating graded porosity, dashed line indicates the average temperature over the cycle.

A 32 mm tall, 5 mm diameter NiTi sample was tested in the same setup and showed differential foaming rates. After 47 hours of cycling (approximatly 400 cycles), the total porosity of the sample was measured to be 4.64%. The sample was then cut into three sections of around 10mm each, one that was fully in the insulation, one that was half inside and half outside, and the last piece that was fully out of the insulation. The porosities of these subsections was measured and found to have 4.36±0.03%, 4.83±0.02% and 5.35±0.04% porosity, respectively. While the absolute difference is not very large, the relative creep rates implied in the sections is significant. If one assumes that the foaming followed the 900^{o}C curve shown in figure 4.19 it would imply that the top had been in the furnace for 1.5 hour while the bottom section had only been in an equivalent 0.75 hour. Further simulation on this system using the average, and effective temperature is done in section 5.2.

This test shows promise for creating a graded porosity structure based on rapid thermal cycling, but due to the problems with foaming NiTi (low terminal porosity, and the mixed oxide layer), this test does not fully illustrate the possibility of this method. A better experiment would be with a metal that does not undergo a phase transition in the desired creep range, and can be foamed to a higher terminal porosity. Ideally, the material would also have a low thermal diffusivity, and be able to be rapidly cooled. In theory one could also use the speed of cycling to change the desired porosity-depth profile. Cycling faster would enhance the foaming of the surface, while slower heating and cooling rates would increase the extent of the porosity at depth. A combined isothermal and thermal cycle could be used to create tailored porous structures.

4.2.4. Metallography

Images of the as-HIP'ed samples show increasing porosity with increasing backfill pressure (figure 4.21). Once the foaming starts, there is an obvious difference from the titanium. Instead of spherical pores, the NiTi pores follow prior powder boundaries and form elongated pores. This then allows the pores to link up much faster and connect to the surface releasing the gas. Since the openings have small elongated shapes, it is not surprising that there is rapid sintering once the gas is vented and surface tension effects can take

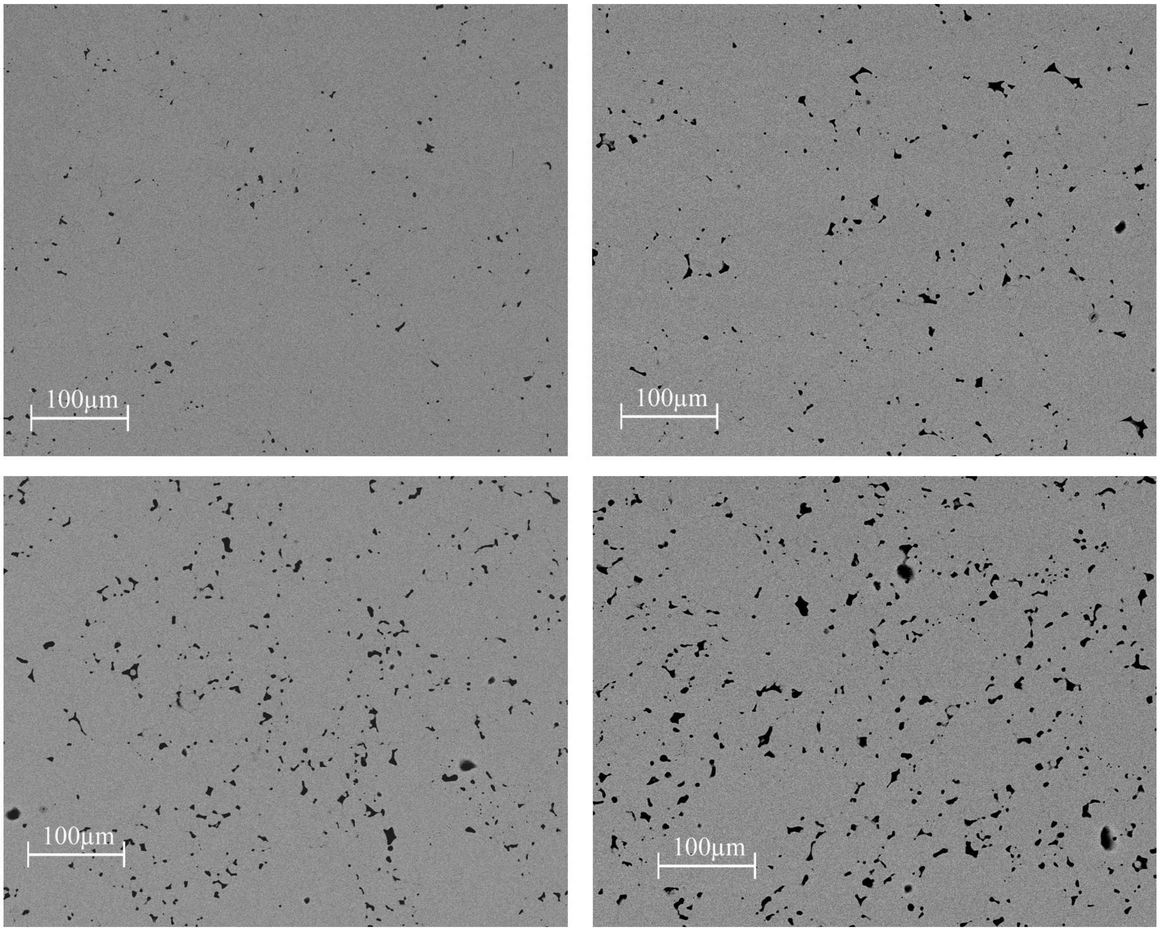

Figure 4.21. Micrographs of as-HIP'ed NiTi showing increasing porosity (f_o=0.43%, 1.34%, 2.26% and 3.92%) with increasing backfill pressure.

over. This can then explain the rapid re-closure of the surface porosity, unlike the slower re-sintering found in Ti-6Al-4V.

In samples foamed at 1200°C for 200 hours (figure 4.22 bottom), the pores were nearly spherical and growing very slowly at long times. This was attributed to the late connecting and re-pressurization of the internal porosity due to size differences in the initial pore distribution. In the case of the high pressure samples foamed for a very short amount of time, there is much less time to spheridize the pores. While the total porosity

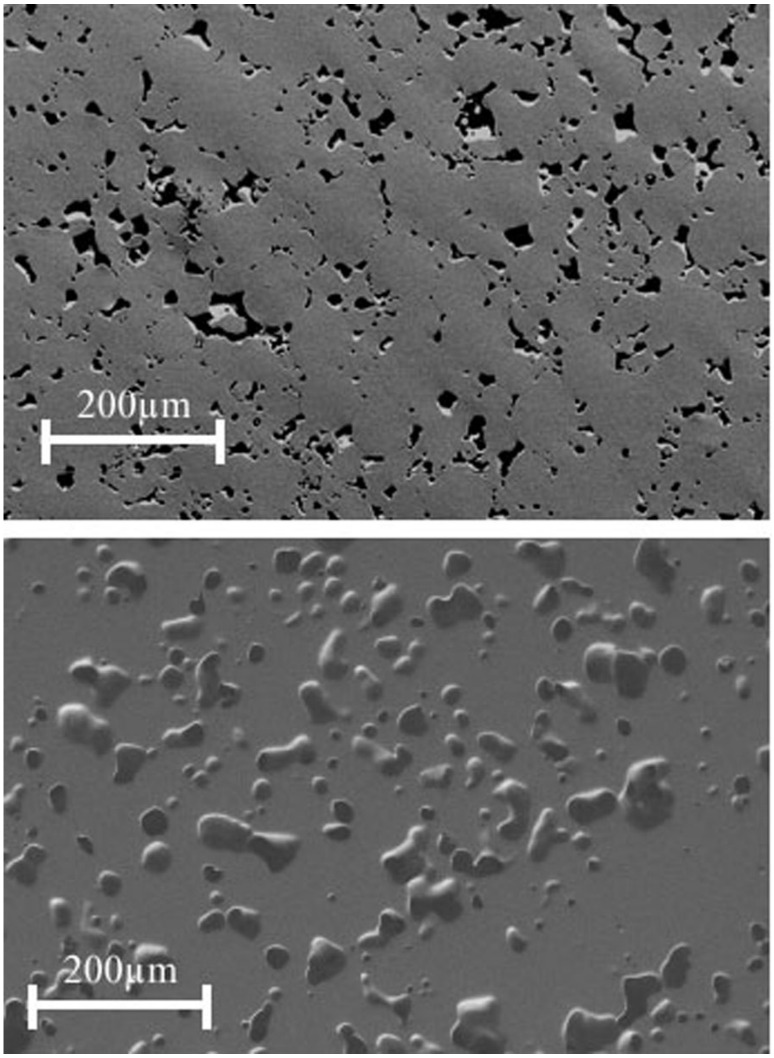

Figure 4.22. NiTi (ρ_o=3.92%) foamed to 14% after 30 minutes at 1150^{o}C (top). NiTi (ρ_o=0.6%) with 17% porosity foamed at 1200^{o}C for 200 hours (bottom).

is similar, the morphologies are very different. This contrasts with high pressure samples that have been foamed at a lower temperature for less time, which are not as round (figure 4.22 top). In both cases these the previous powder particles are easily seen (figure 4.24).

One significant feature of the NiTi foams is the large non-foaming regions that correspond to materials in the original powders far from the initial entrapped pores. Figure

4.23 shows a fully open 14% NiTi foam with such non-foaming areas highlighted on the bottom. This shows that while the whole foam is gaining porosity, there are large sections that do not participate in the foaming process. While the shading is done in a heuristic manner, it is clear that as compared to a relatively modest total sample porosity of 16%, porosity in foaming sections show locally much higher porosity, on the order of twice the overall porosity.

The reason for early connecting and the high local porosity network, can be explained by the weak interface between pressed particles. Titanium can dissolve its own oxide so such interfaces do not exist. NiTi will instead form complex mixed oxides that are stable. Figure 4.24 shows the interface between two such powders taken where the darker bands indicated by arrows are expected to be a mixed oxide second phase. Due to the small size, determination of the specific phase was not possible, but it was found through energy dispersive x-ray spectroscopy (EDS) that the dark spots pointed at by arrows in figure 4.24 are titanium rich as would be expected with titanium's higher affinity for oxygen. Figure 4.25 shows two EDS spectra, both normalized to the titanium peak, the lower relative amount of nickel (smaller nickel peak) in the interface spectra shows titanium enrichment, and implies oxygen contamination.

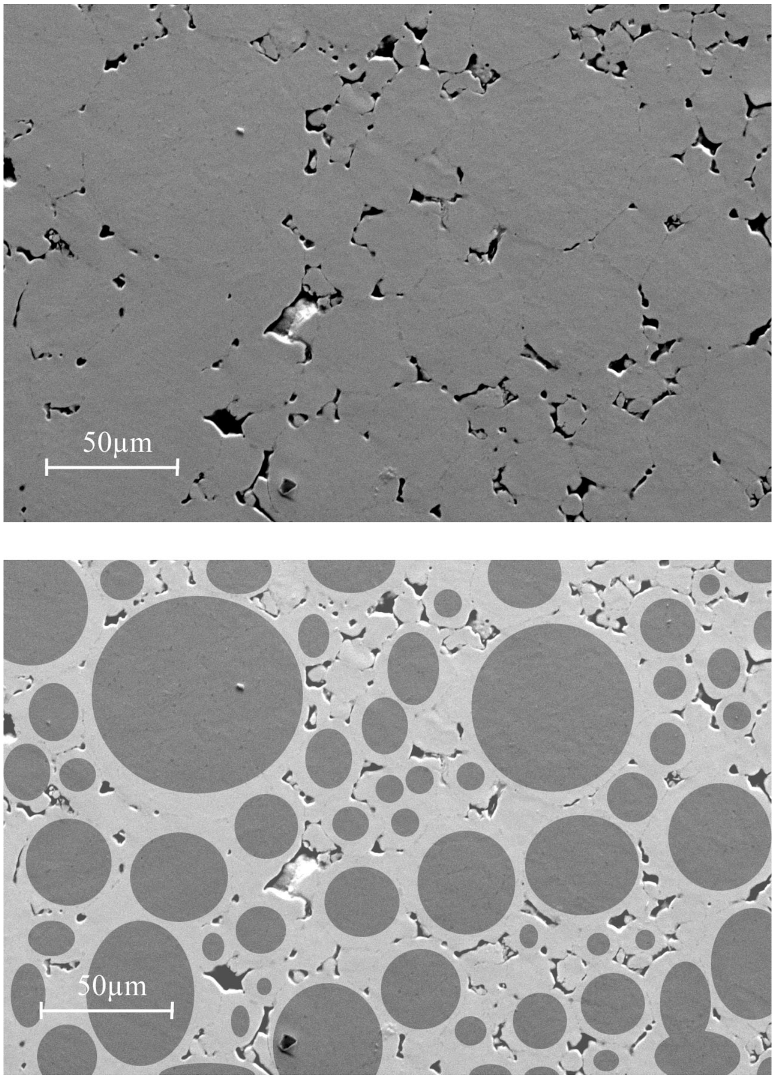

Figure 4.23. NiTi (ρ_o=1.34%) foamed to 14% after 32 hours at 900^{o}C showing the pore morphology and a false color on the bottom highlighting foaming regions.

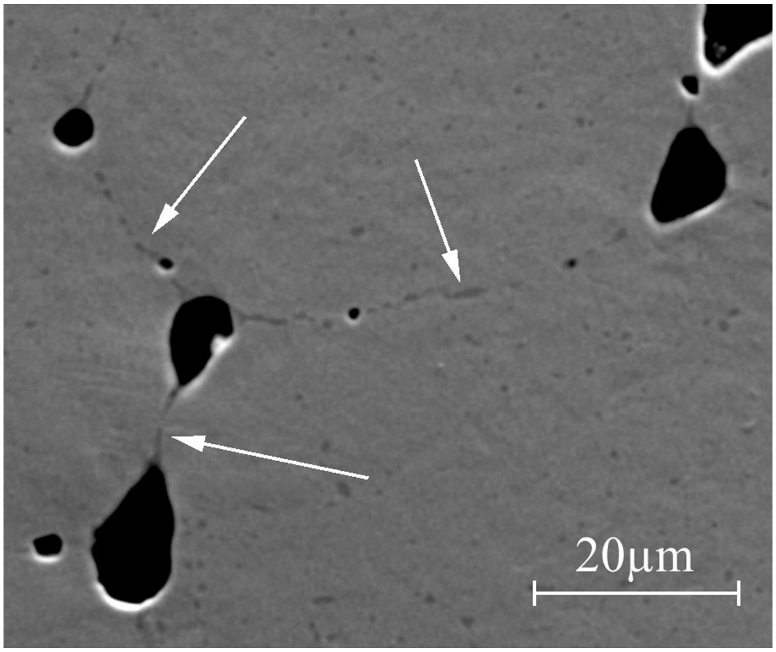

Figure 4.24. High magnification image of NiTi foam showing the interface between previous powder particles, arrows indicate likely oxide phase.

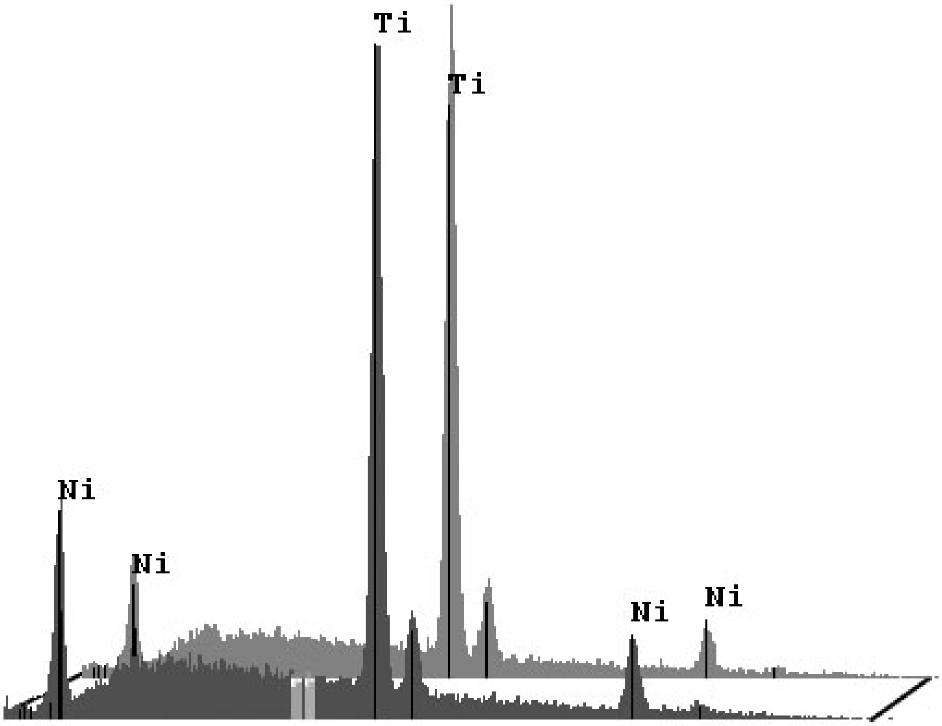

Figure 4.25. EDS patterns of the matrix (front) and interface (back), showing titanium enrichment at the interface.

4.2.5. Mechanical Properties

Transmission ultrasonic tests were performed on all of the foamed NiTi samples as well as a section of solid NiTi HIP'ed without gas. A plot of all of the results can be seen in figure 4.26. In the same manner as for the titanium samples (figure 4.1.3) the porosity and modulus data were fit to the Gibson-Ashby, and the Wanner equations (eqs. 4.1 and 4.2). In this case, η was found to be 2.85 for the current study, and 2.57 for Greiner samples, which is much higher than for the nearly spherical Ti-6Al-4V pores for which η equaled 2.18. For NiTi, there is much stronger agreement with the Wanner model due to the non-spherical nature of the pores.

In order to reach the target of 10-20 GPa modulus for bone, NiTi porosity would have to be about 35%. However, in the case NiTi, the ultrasonic modulus is not relevant to the macroscopic stress-strain curve. Transformation superelasticity effectively lowers the slope of the stress-strain curve, leading to an apparent elastic slope which is much smaller than the Young's modulus, as has been seen in previous studies [**77**]. Figure 4.27 shows mechanical tests that give a 24 GPa apparent elastic slope which is near the upper range for bone (20 GPa).

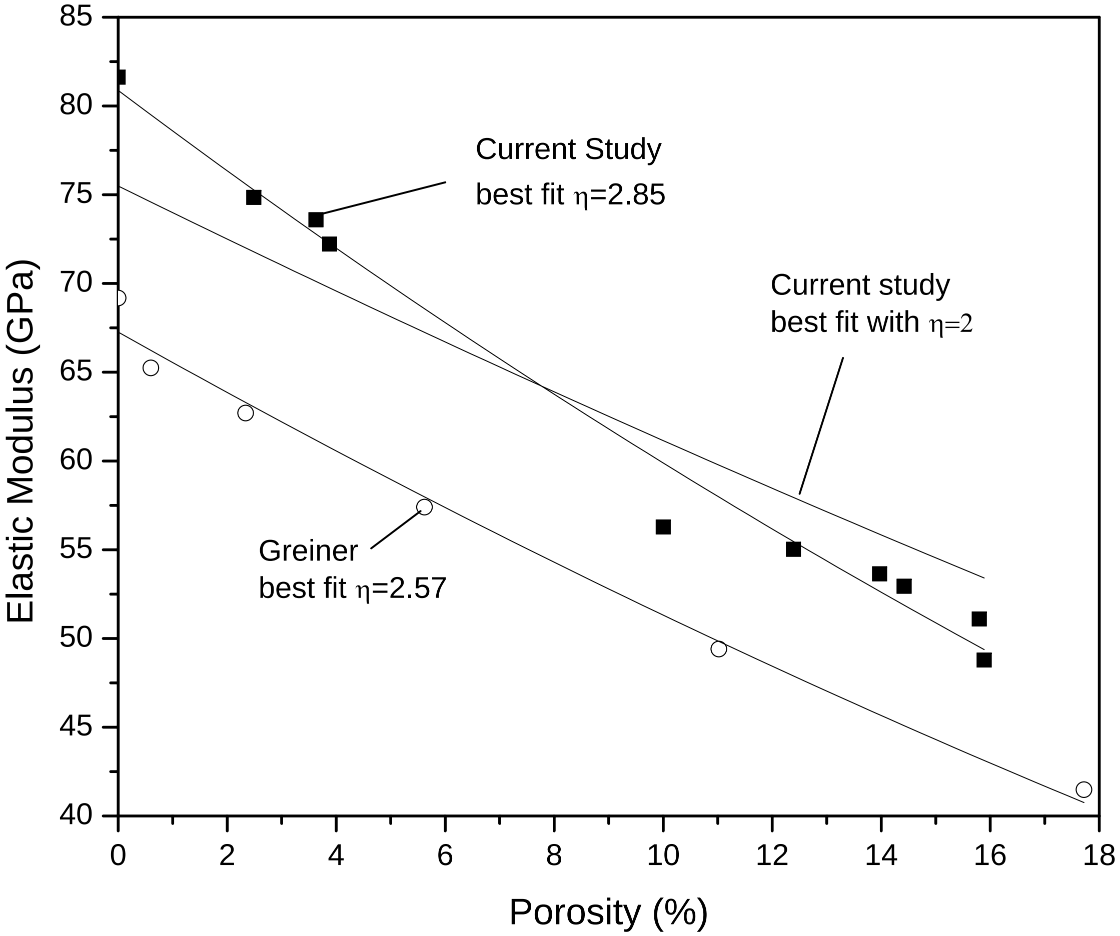

Figure 4.26. Ultrasonic Young's modulus measurements as a function of porosity, for both Greiner 51 at% Ni, and current study 49 at. % Ni foams. Lines show best fit of Wanner equation, as well as a fit of the Gibson-Asbhy equation (η=2) to current study data.

4.2.6. Synchrotron X-Ray Measurement

Figrue 4.27 shows the stress strain curve of a foamed NiTi sample. The specific sample used in the x-ray analysis was a B sample with a 2 atmospheres of argon backfill pressure, and initial porosity of 0.6%. After foaming for 170 hours at 1200^{o}C a final porosity of 17.1% was found. The foamed sample was then cut into compression specimens 2.5mm square by 5mm tall, and heat treated to be superelastic as described in detail in section 3.8. This sample has very similar microstructural features to the bottom image of figure 4.22.

Due to limitations with the testing apparatus, the load and crosshead displacement had to be recorded by hand, and as such it is not as smooth as would be preferred. The strain was then calculated by correcting the crosshead displacement by subtracting the system compliance. The lowest stress tested was around 50MPa and this was due to the nature of the loading rig, which had significant play at low stresses. Figure 4.27 shows the stress strain curve recorded, with open squares denoting stresses at which diffraction patterns were recorded. Also on this figure are curves from Greiner [**77**] for 16% NiTi, and solid NiTi explored by Vaidyanathan [**78**]. There is significant strain recovery on unloading, indicating that the NiTi is superelastic. The elastic modulus (39 GPa on unloading) is less than ultrasonic measurements would predict (47 GPa), which is expected due to the transformation.

Figure 4.28 shows a diffraction pattern of the NiTi foam under very low stress (50MPa, fully austenitic). The grain size found by Christian Greiner, for an equivalently aged and heat treated sample, was 36μm, while the beam size was 100x100μm. The sample was 2.5mm deep which gives an interaction volume corresponding to hundreds of grains

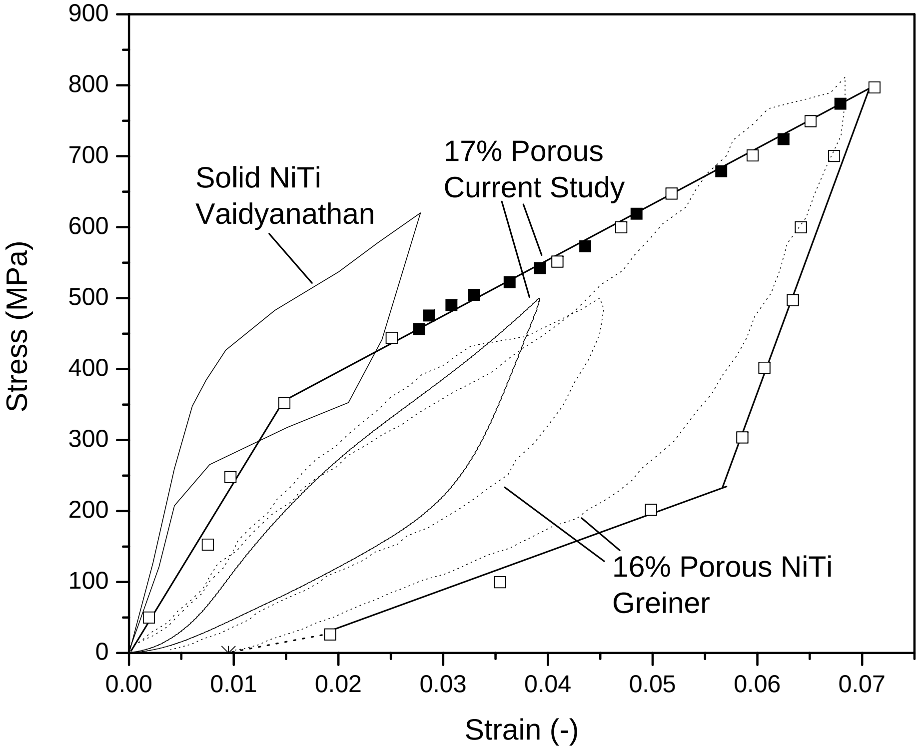

Figure 4.27. Stress-strain curves of heat-treated superelsatic NiTi of 17.1% porosity, (current study), 16% porosity (Greiner), and solid (Vaidyanathan). Open squares represent points at which a diffraction patterns were taken, the star represents post stress dimension measurements of permanent strain.

sampled. With this relatively few grains, there were very strong spots in the diffraction ring, which over-saturated individual pixels in the detector (leading to incorrect peak areas). In order to keep the rings smooth by diffracting off as many grains as possible, the sample was scanned over a 2 x 4mm area for a total volume of interaction that included thousands of grains. Even with this sampling method, larger individual grains can be seen in the zoomed-in inset of figure 4.28. As stress is applied, the diffraction pattern becomes much more complex as the martensite phase is created. Figure 4.29 shows many more peaks as well as broader peaks. There is also significant texture as the material is stressed and forms twinned martensite. Texturing can be seen in preferential orientation of some of the rings one of which is highlighted in the inset of figure 4.29.

In order to measure the phase fraction of the two phases upon loading, the intensity of the diffraction rings were integrated. This allowed for a single intensity as a function of diffraction angle (theta). Two integrated diffraction spectra are found in figure 4.30. Due to the large number of overlapping peaks, it was difficult to find a suitable pair of rings for phase fraction analysis. The highlighted box shows the two peaks that were isolated enough to be used for phase fraction analysis. The martensite peak chosen corresponds to the (010) reflection (also seen in the inset of figure 4.28), while the austenite peak chosen is a double lattice reflection of the (110).

The two peaks used in analysis are plotted on loading, figure 4.31, and on unloading, figure 4.32. It is easily seen that the austenite peak gets smaller with increasing stress while the martensite peak gets larger.

From the diffraction patterns, it is easy to visually determine that the phase fractions are changing, but in order to determine precise phase fractions the areas of the peaks needs to be calculated. This was accomplished by first subtracting out the background and cropping to just the peaks of interest. The areas were then found by integrating each peak separately (figure 4.33 illustrates this method).

A plot of the areas can be seen in figure 4.34, and shows that, as expected, the martensite peak grows with increased stress and the austenite peak is reduced. Plotting the austenite peak area vs. the martensite peak area results in a linear relationship (figure

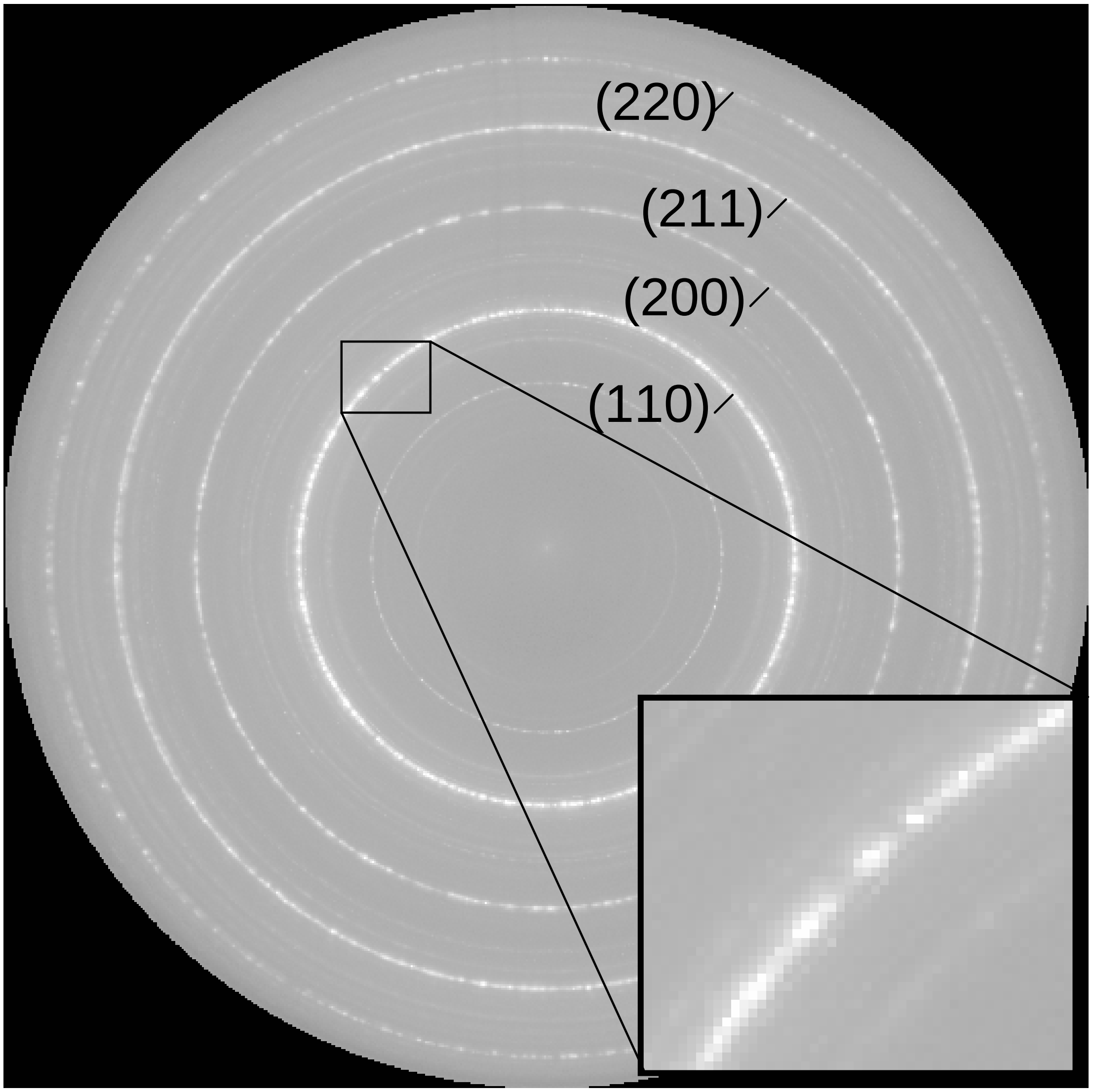

Figure 4.28. NiTi X-Ray diffraction images of 17.1% NiTi foam captured by the MAR detector, at 50MPa stress. Inset shows spots of individual grains. The main austenite rings are identified.

4.35). The end points (lowest and highest stresses) are close enough to the best fit line that they are used as anchor points to determine phase fractions. From the area analysis performed, 23% of the sample was still austenitic at the highest stress. By normalizing

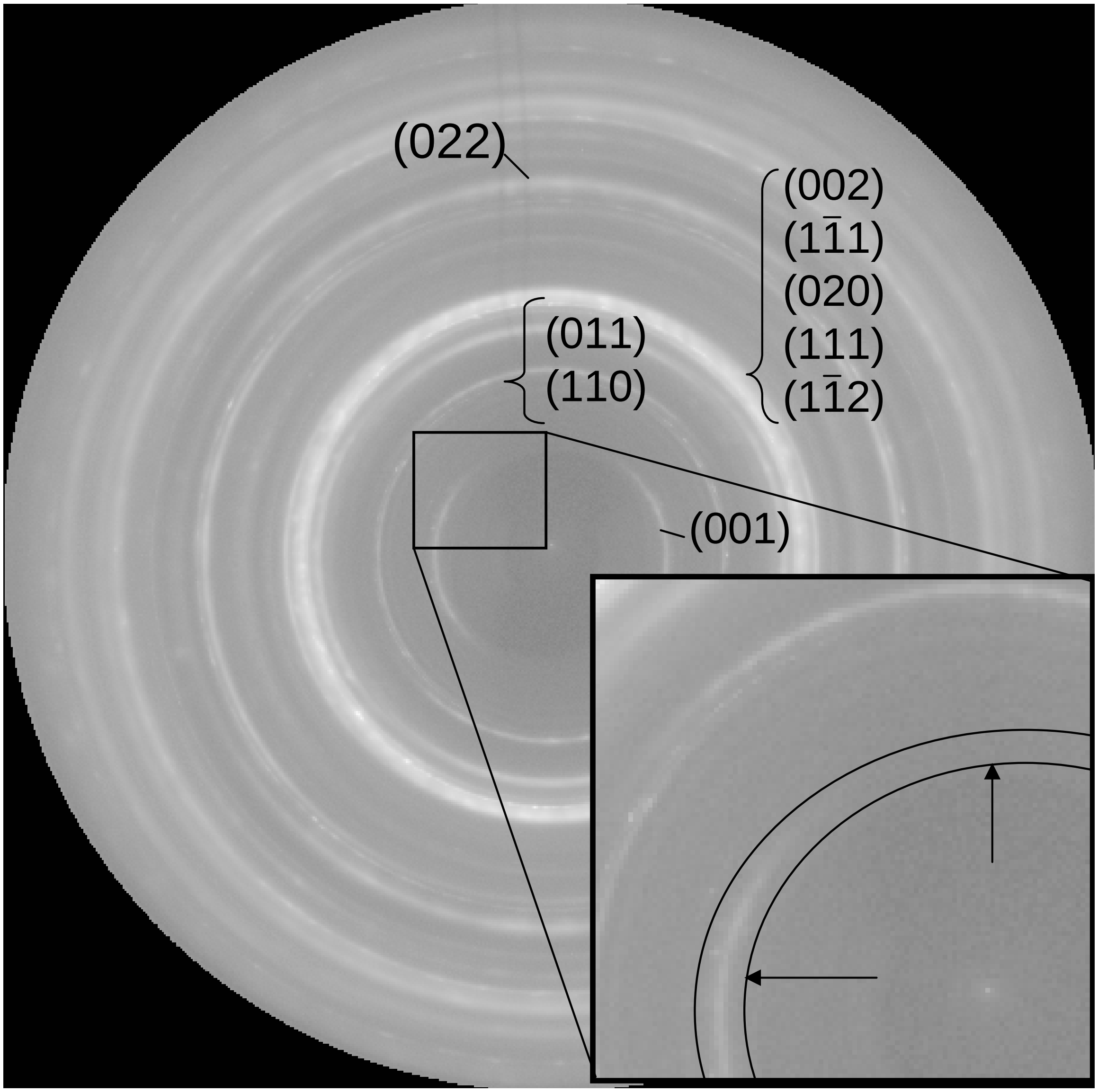

Figure 4.29. NiTi X-Ray diffraction images of 17.1% NiTi foam captured by the MAR detector, at 800MPa stress, with major martensite rings identified. Inset shows magnified view of an (001) martensite ring with arrows showing preferential orientation of grains (texturing).

the peak areas to the maximum expected volume fraction of each phase and using the linear relationship seen in figure 4.35 the phase fraction for each phase is determined. The stress vs. phase fraction can be seen in figure 4.36.

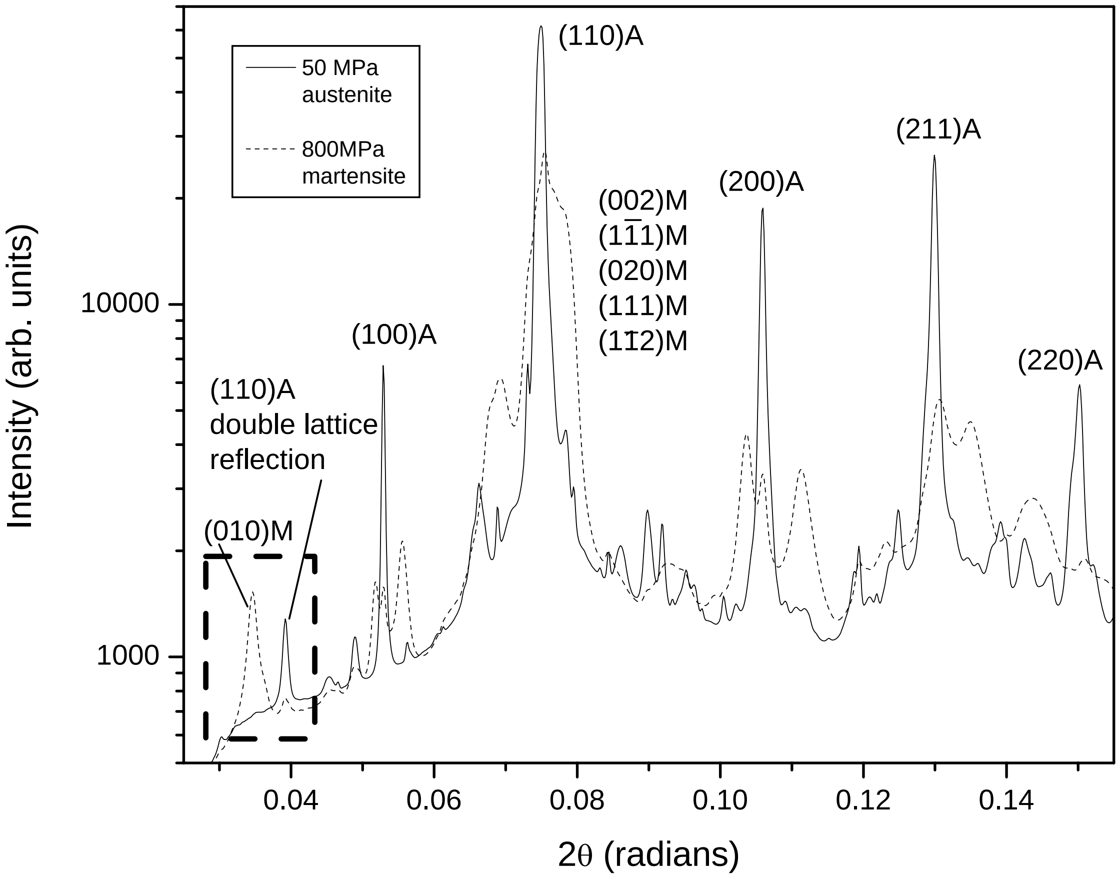

Figure 4.30. Integrated diffraction plot showing 50 MPa and 800 MPa stress patterns (austenite, and martensite respectively), the box denotes peaks used in phase fraction analysis.

Figure 4.37 shows the transformation extent as a function of strain. This strain is the sum of the elastic strain, the transformation strain, and the plastic strain (due to dislocation motion). The anelastic strain is found by removing the elastic strain (determined by the 42.5 GPa Young's modulus measured by ultrasonic measurements) from the total strain. Plotting the transformation extent vs. this anelastic strain (figure 4.38) shows two effects. First, the slope of the curve on loading is much lower than for non-porous NiTi measured by neutron diffraction [**78**], for which transformation strain only contribute to

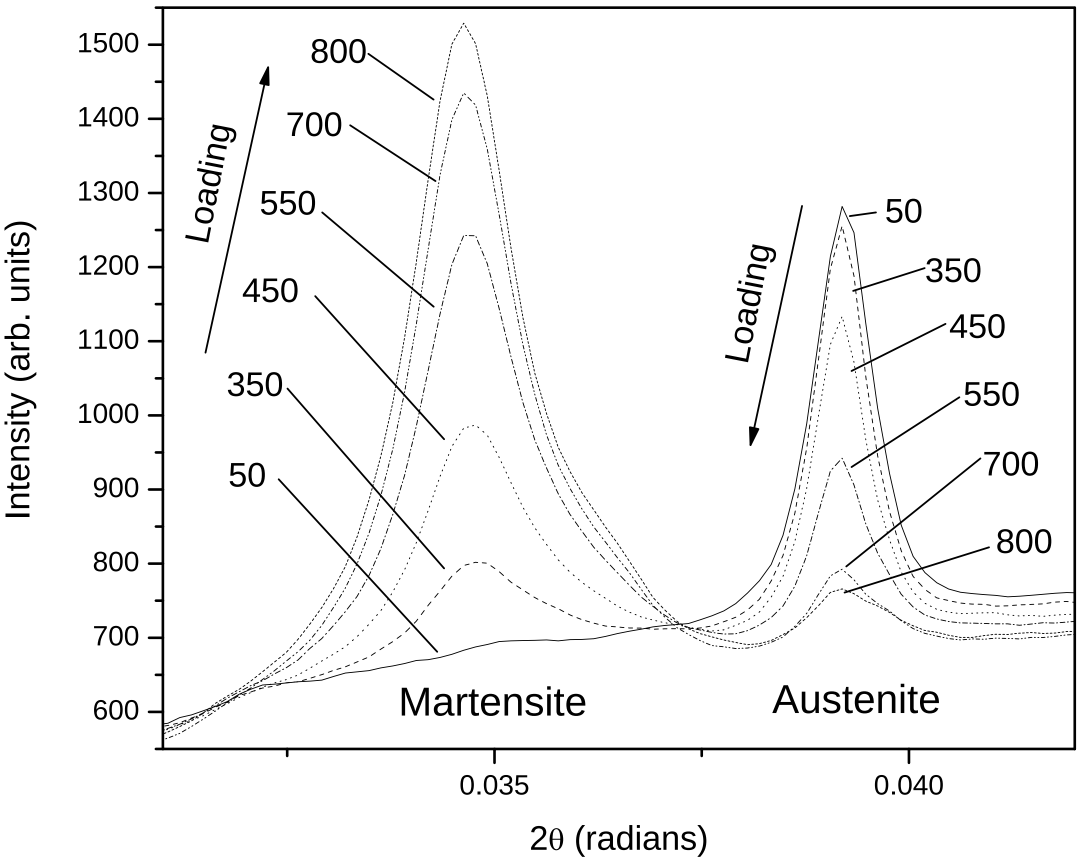

Figure 4.31. Series of diffraction plots showing the effect of loading on two peaks belonging to the martensite phase, and the austenite phase. Numbers indicate stress in MPa.

the anelastic strain. The Gibson-Ashby and Wanner relationships for how the Young's modulus changes with porosity gives a starting point for analyzing the transformation elasticity. The dotted line shown in figure 4.38 shows the slope NiTi transformation slope modified by the Gibson-Ashby equation 4.1, and is very nearly the initial slope found in the experiment.

Second, on unloading, a large hysteresis is found, unlike the prior data on non-porous NiTi. Both effects can be explained by the onset of plastic strain in the foam at stress

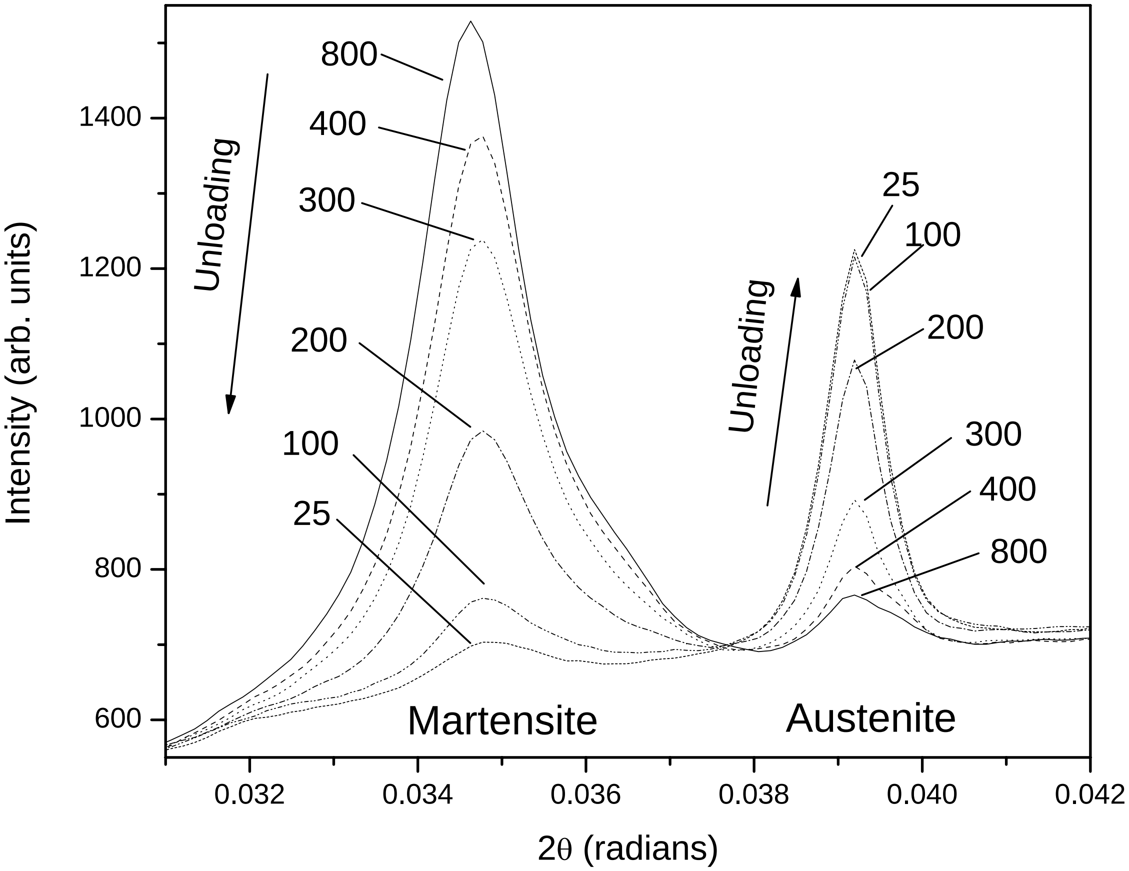

Figure 4.32. Series of diffraction plots showing the effect of unloading on two peaks belonging to the martensite phase, and the austenite phase. Numbers indicate stress in MPa.

concentrations near the pores, which will cause plasticity at low applied stresses on loading. On unloading, these strain hardened regions are then unable to back transform, as reported in prior work on cold-worked non-porous NiTi [**79**].

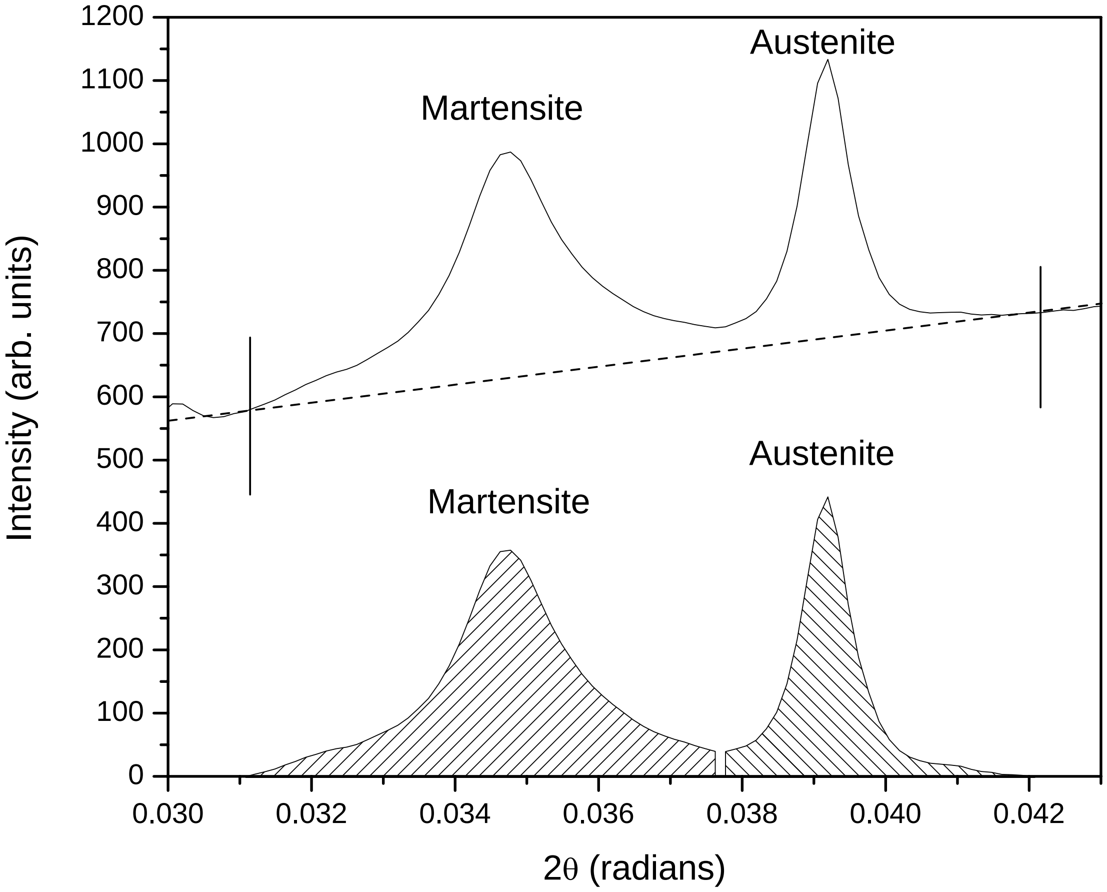

Figure 4.33. Plot of (010) martensite and (110) double lattice austenite peaks at 450 MPa. Dashed line indicates the background, solid vertical lines indicate the area of interest, and the lower hashed areas indicate the areas of each of the peaks.

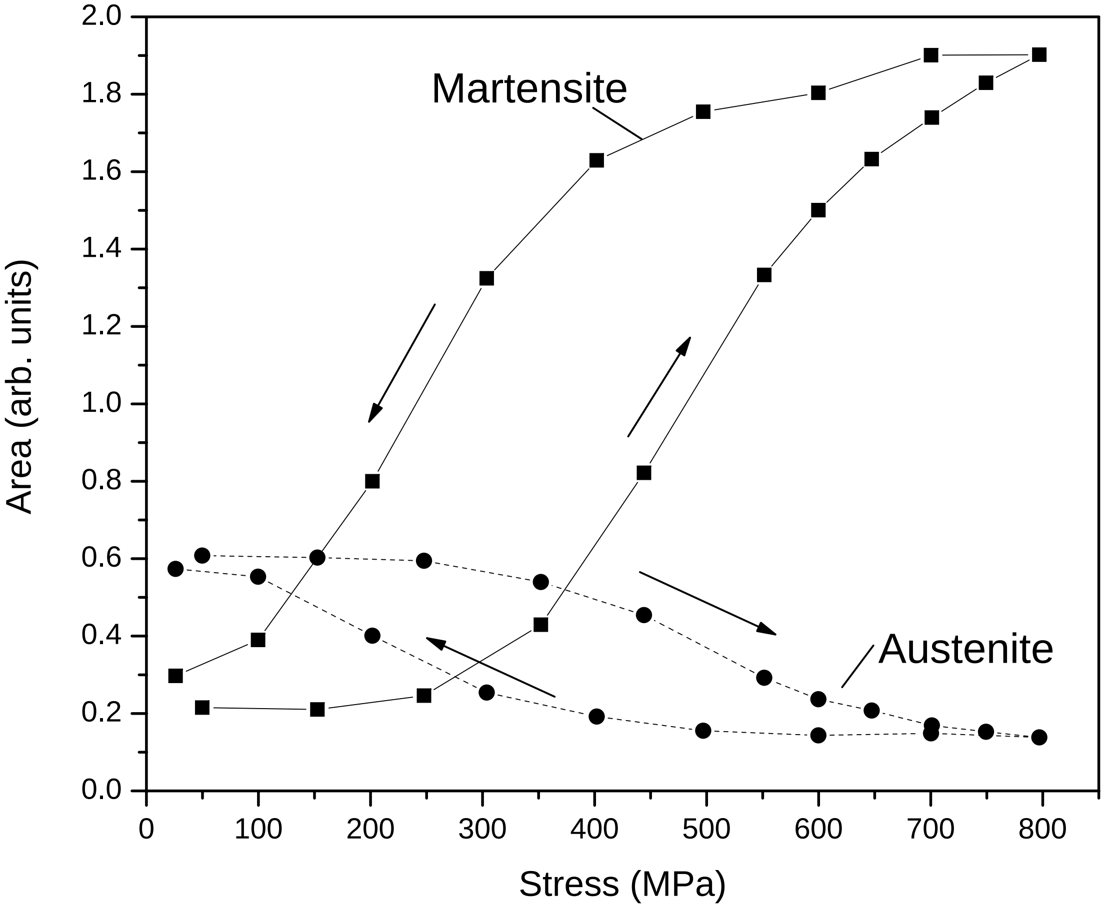

Figure 4.34. Peak areas for austenite and martensite phases as a function of stress for 17.1% porous NiTi (arrows indicate loading and unloading).

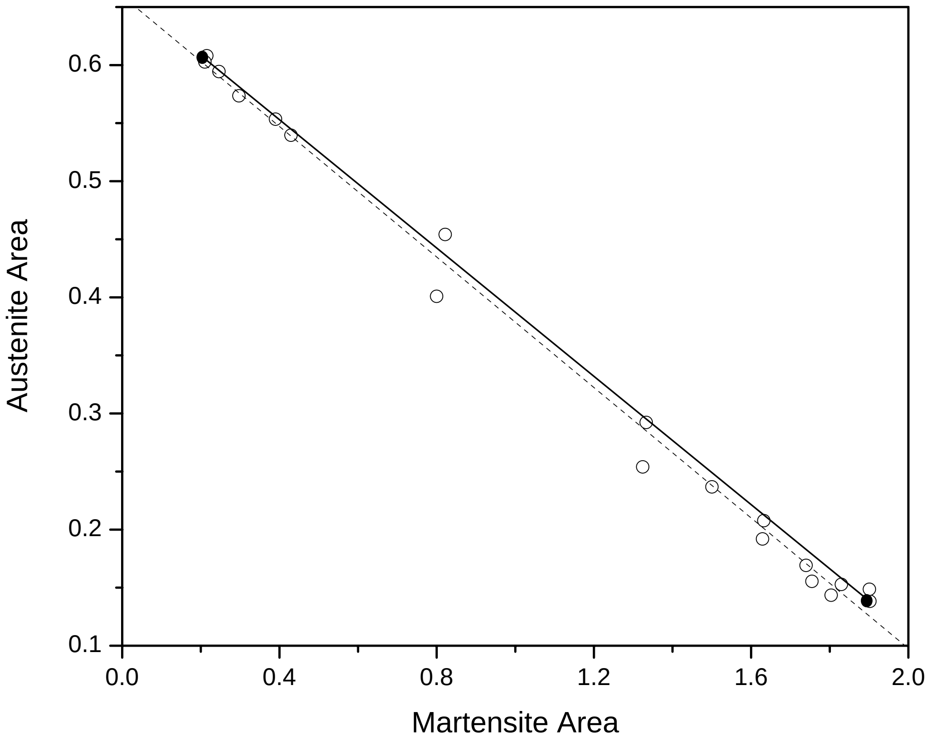

Figure 4.35. Peak area of austenite vs. peak area for martensite with symbols representing synchrotron data collected at various stresses. Dotted line is a best fit to the data, the solid symbols and line represent the highest and lowest stresses and are used in phase fraction analysis.

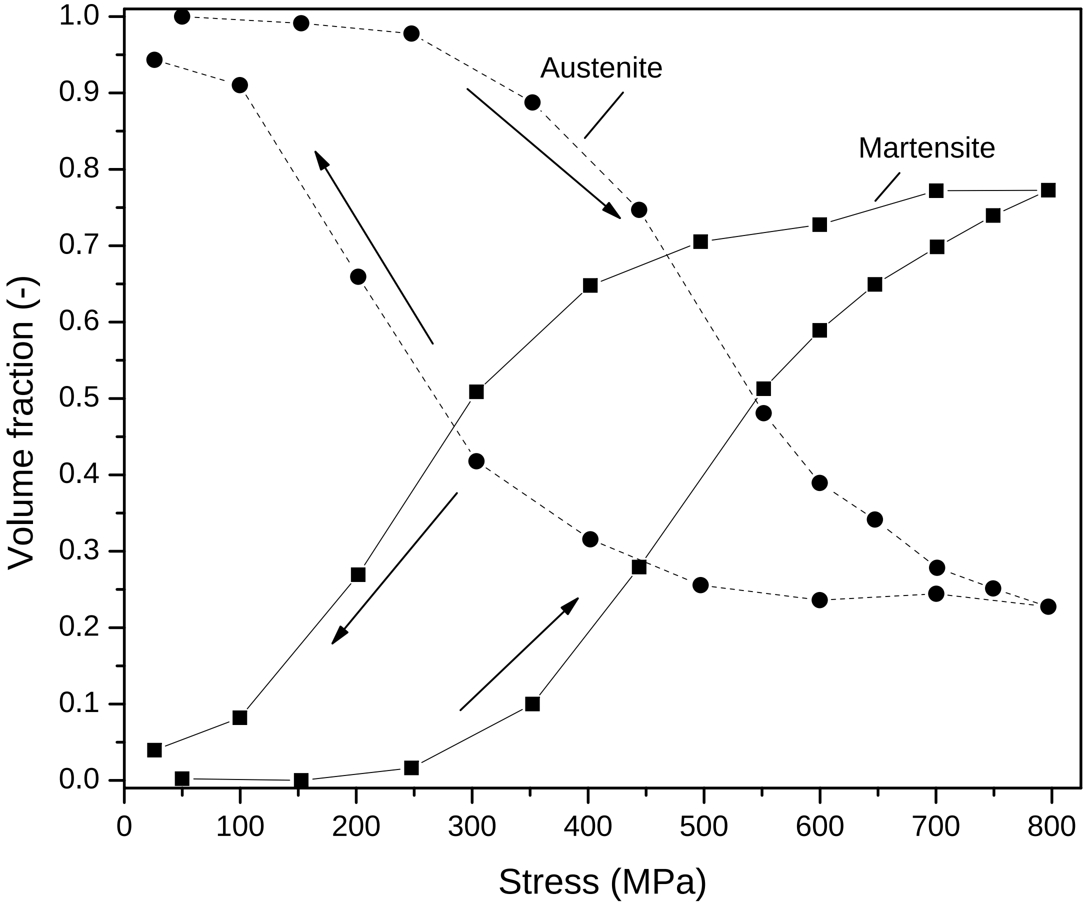

Figure 4.36. Volume fraction for austenite and martensite phases as a function of stress for 17.1% porous NiTi (arrows indicate loading and unloading).

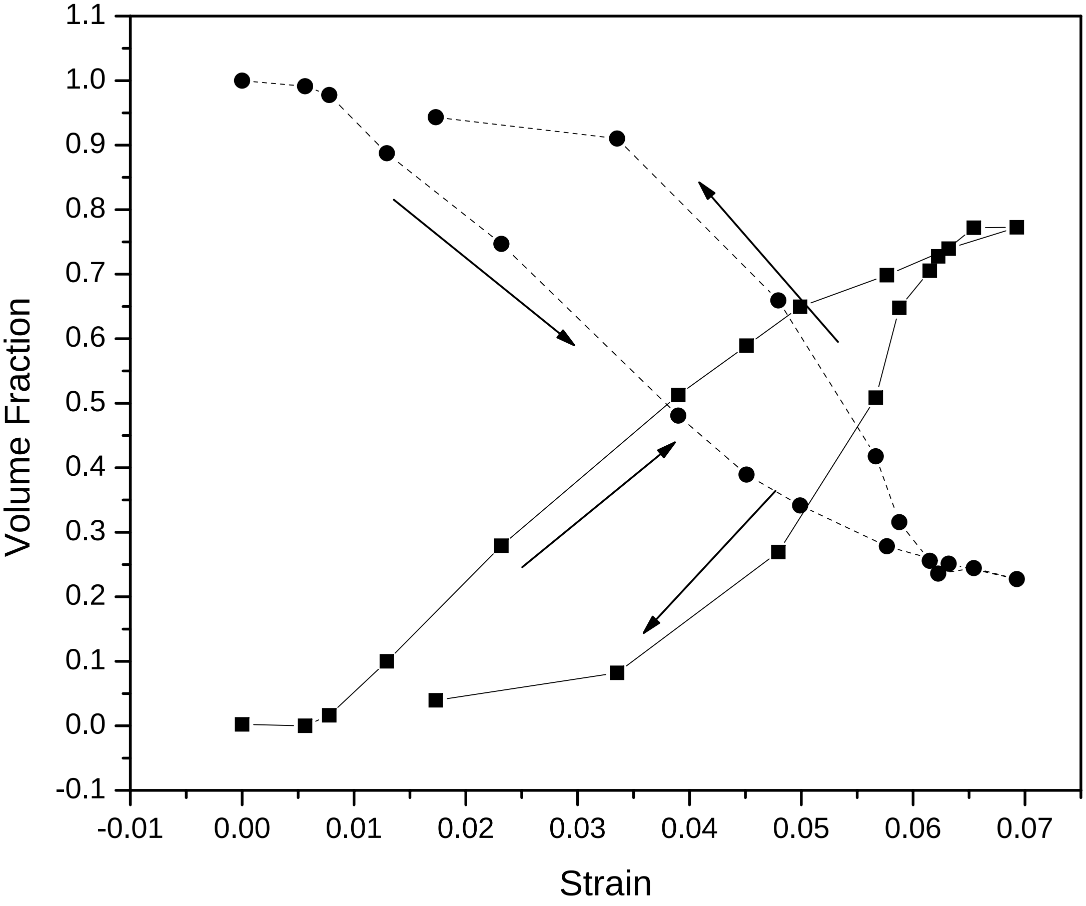

Figure 4.37. Volume fraction for austenite and martensite phases as a function of total compressive strain for 17.1% porous NiTi (arrows indicate loading and unloading).

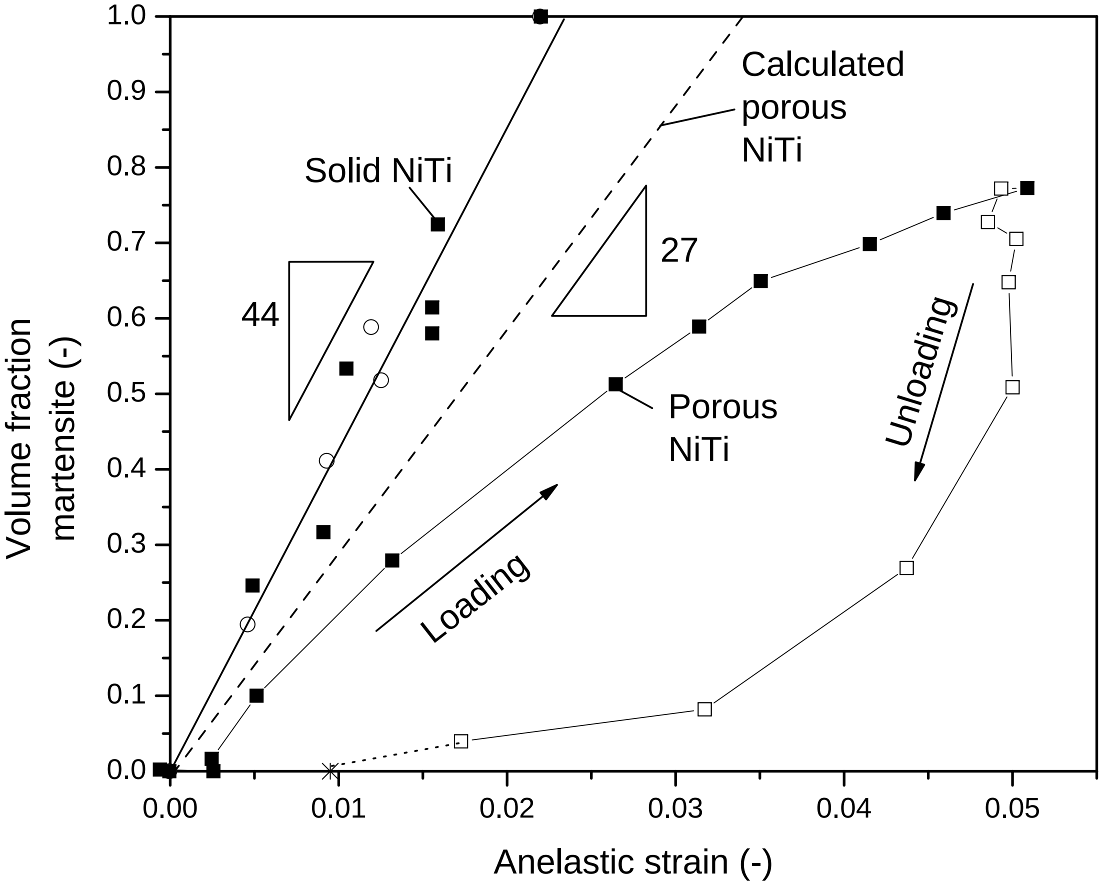

Figure 4.38. Plot of the degree of transformation as a function of anelastic strain for 17.1% NiTi. The solid line is a best fit to solid NiTi data [78], the dotted line shows the solid transformation modified by the Wanner equation (η=2.57).

CHAPTER 5

Modeling of Pore Expansion

5.1. Introduction

To achieve a greater understanding of the foaming of Ti-6Al-4V and NiTi, it is useful to simulate the growth of pressurized pores. Having accurate simulations also predicts ways in which the processing can be improved. In the case of porous metals created by the Kearns process, an obvious place to start is with a single pore and its growth in the creeping metal matrix.

To determine the way in which the pore expands, the creep nature of the metal matrix becomes very important. For this reason, the first step in the simulation of porosity growth is to determine the basic creep parameters of the materials used. Previous work [**71**, **80**] shows that in general, creep follows a typical pattern with three stages. First, there is an initial fast primary creep where many dislocations are created and the sample deforms rapidly. The creation rate of dislocations is much faster than their movement and annihilation rate in this first stage, which leads to a buildup and a slowing of the creep rate. Eventually the second stage is reached, where the rate of creation of dislocations equals the rate at which they move and leave the sample. This secondary creep can be described by the power-law creep equation:

$$\dot{\epsilon} = A'\sigma^n exp\left(\frac{-Q}{RT}\right) \tag{5.1}$$

where $\dot{\epsilon}$ is the uniaxial creep rate, σ is the uniaxial stress, n is the stress exponent, Q is the activation energy, T is the temperature, R the gas constant, and A′ is a material dependent constant. Due to the rapid drop in gas pressure as the pore expands, the system should very quickly reach a dislocation equilibrium and secondary, power-law creep. As can be seen in the equation, there is a strong exponential response in temperature, resulting from the diffusion needed for dislocation movement.

In the temperature ranges given, the fundamental creep properties of Ti-6Al-4V had already been experimentally determined [**81**]. In the case of NiTi, creep experiments were performed and the results are reported in section 4.2.1. It was easier to solve the Arrhenius part of the equation and use a modified creep equation for the simulations performed:

$$A = A'exp\left(\frac{-Q}{RT}\right) \tag{5.2}$$

leading to a power-law equation of the form:

$$\dot{\epsilon} = A\sigma^n \tag{5.3}$$

Material	*A'*(MPa^{-n})	*Q(kJ/mol)*	n
Ti-6Al-4V [**49**]	0.72	153	2.8
Superplastic Ti-6Al-4V [**49**]*	$2.645 \cdot 10^{-6}$	NA	1.1
NiTi	0.05	155	2.7
CP-Ti [**82**]	$7.544 \cdot 10^{-3}$	153	4.2

*cycled from 840-1030^{o}C, at 8 minutes per cycle

Table 5.1. Creep parameters used in simulations.

For the isothermal runs, a single temperature is all that is needed for both the creep properties as well as accurate gas pressure prediction. For the thermally cycled runs, there are two separate temperatures of interest. The first is the effective temperature for isothermal creep which is calculated in the same way as in section 4.4. A second temperature is used to determine the internal pressure of the gas, for the thermally cycled runs this was set at temperature at which 50% of the Ti-6Al-4V phase transformation is complete (954^{o}C). Due to limitations in the current simulation code only one temperature could be used, but as there is very little creep outside of the transformation, the 50% transformation was chosen. The parameters used in the creep models can be found in table 5.1.

5.2. Single Pore Models

The next step in creating a model was to model the stresses (and therefore deformations) in the matrix caused by the pressurized pore. There were three approaches that were used in modeling the system. The first was to use a full three dimensional finite element model which included the stresses from neighboring pores. The second was to use a two-dimensional, axi-symmetric, finite element model that would not truly fill space, but could simulate space-filling and neighbor interactions. The third was to use an analytic formula for the growth of a single pore in a matrix.

5.2.1. 3D Finite Element Model

In the case of the full three-dimensional model, a finite element (FE) mesh was created using Abaqus CAE 6.3, and solved using Abaqus Standard 6.3. Due to symmetry, only 1/8th of a cube was modeled. All of the faces were held flat and parallel, which creates a mirror symmetry in all directions; this has the effect of creating an infinite number of expanding spheres on a cubic lattice. Figure 5.1 shows a representation of the model.

Figure 5.2 shows the FE model itself at 1% and 13% porosity. In this specific model, full integration, linear elements were used for the bulk material (Abaqus specific element C3D8). The geometry supported cubic elements, and the full integration was needed for the large deformation encountered. To simulate the gas, 2D fluid elements were chosen for their ability to automatically adjust pressure with volume increase (F3D4). The ideal gas law was used internally for all of the finite element simulations. The volume of the gas and the total system volume were output at each time interval. The Abaqus visco solution method was used due to the large, time-dependent creep deformations.

5.2.2. 2D Finite Element Model

Two dimensional, finite element, axi-symmetric models were also created in Abaqus CAE 6.3, and run in Abaqus Standard 6.3. In this case, it is assumed that a close-packed array of cylinders is a good representation of space filling hexagonal prisms. This assumption was found to be acceptable in previous work [**39**]. In this case, a representative volume

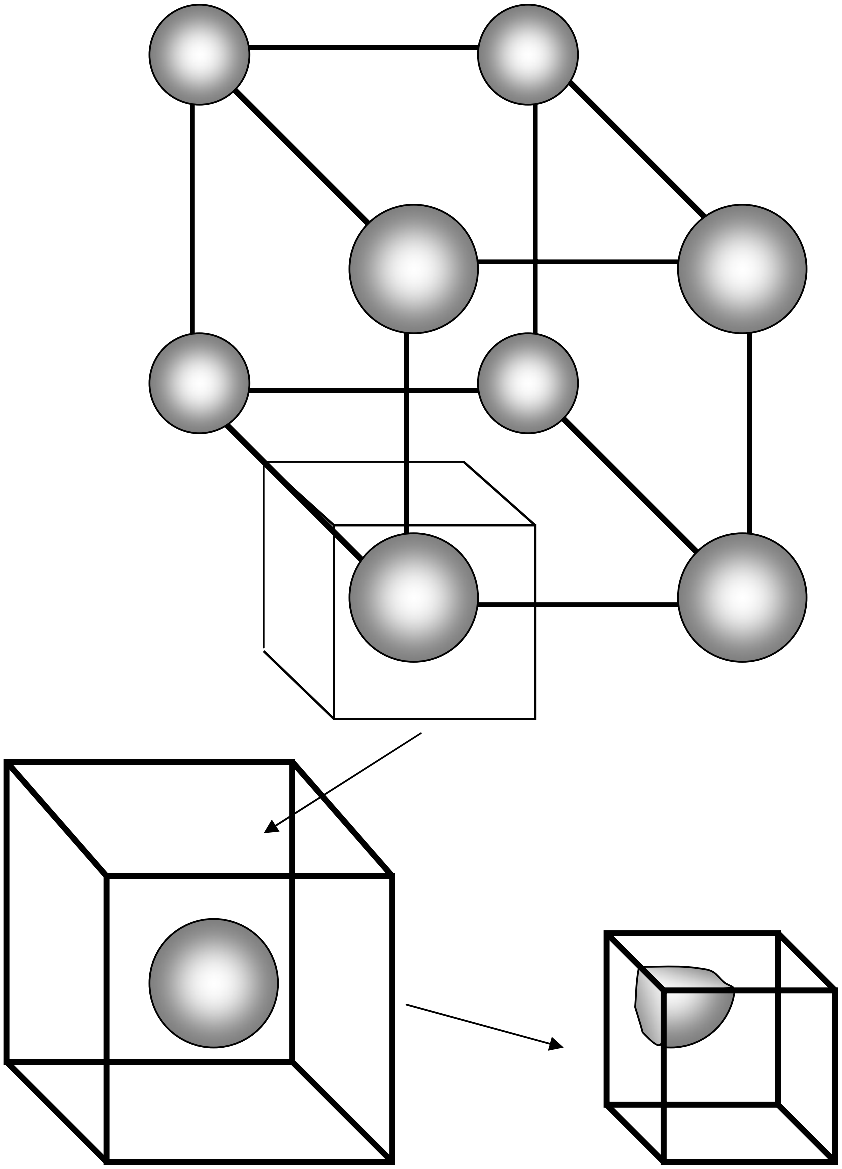

Figure 5.1. 3D model system for pore growth, lighter shades represent higher Von Mises stresses. 1% starting porosity (left), and 13% porosity (right).

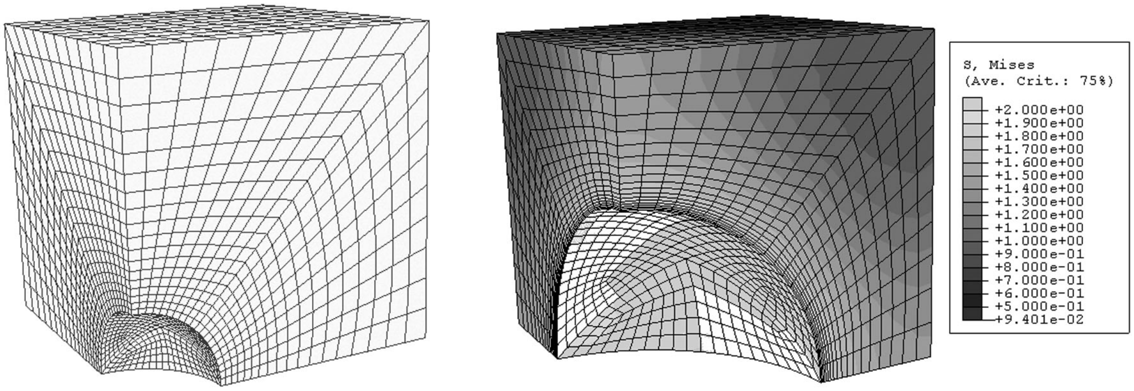

Figure 5.2. Three-dimensional finite element model used for pore growth.

element of a single pore in a cylinder was used. As was true in the 3D case, the full model is not needed but instead one half of the axi-symmetric pore was used. Figure 5.3 shows the representative volume and axi-symmetric approximation.

The specific implementation of the axi-symmetric model can be seen at 1% and 13% total porosity in figure 5.4. As in the 3D model, full integration linear elements (CAX4) were used to deal with the large deformations, while two dimensional fluid elements (FAX2) were used for their ability to actively update the pressure of the expanding gas.

5.2.3. Analytical model

Lastly the most abstract model created was a closed-form solution of a spherical pressure vessel expansion [**83**]. This model is the simplest, as it does not take into account neighbor stress, but instead considers a single pore growing in isolation. This model uses the ideal gas law, conservation of volume of the creeping matrix, and a creep rate given by equation 5.2, which are then combined into [**39**]:

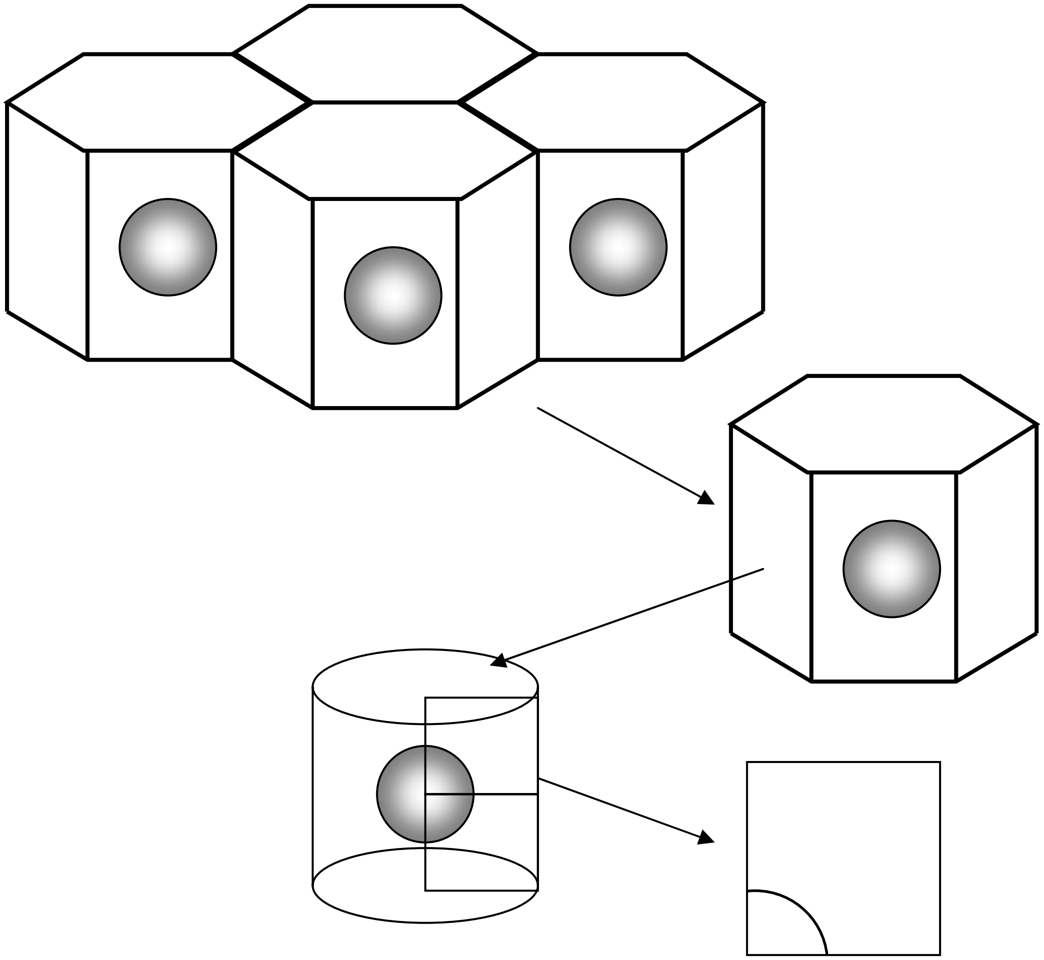

Figure 5.3. Series of approximations used in the axi-symmetric model.

$$\dot{f} = \frac{3A_{creep}}{2}\frac{f(1-f)}{[1-f^{\frac{1}{n}}]^n}(\frac{3}{2n}P)^n \tag{5.4}$$

where $\dot{f}$ is the rate change of porosity, f is the current porosity, and P is the driving pressure. Equation 5.4 can be solved by taking a small time step, updating all of the

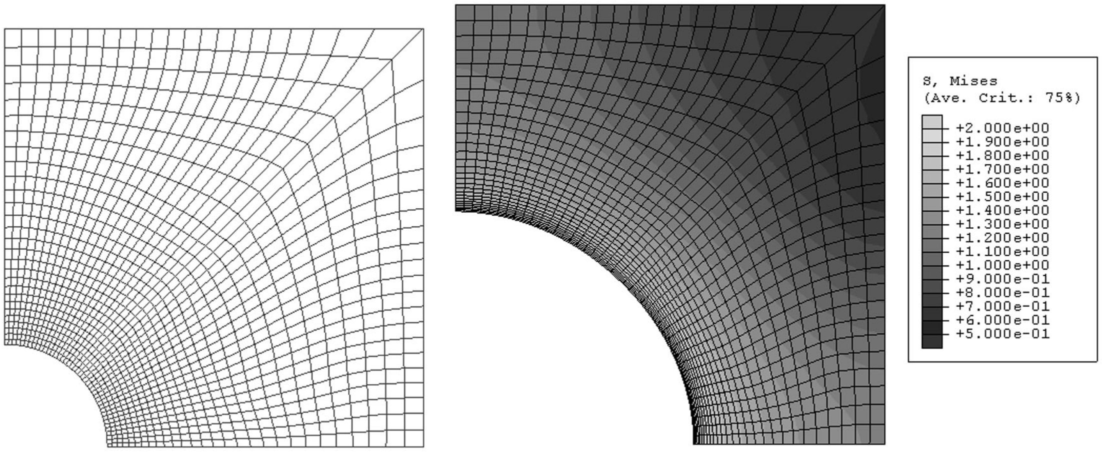

Figure 5.4. Axi-symmetric 2D finite element model, lighter shades represent higher Von Mises stresses. 1% starting porosity (left), and 13% porosity (right).

variables, and proceeding to take another time step. By using sufficiently small time steps, the system converges. By monitoring the amount of change at each step, the time of future steps can is modified to balance computation time with low error. Figure 5.5 shows the effect of initial time step and maximum time step on the results. The specific java code used is described in the appendix (section 0.1).

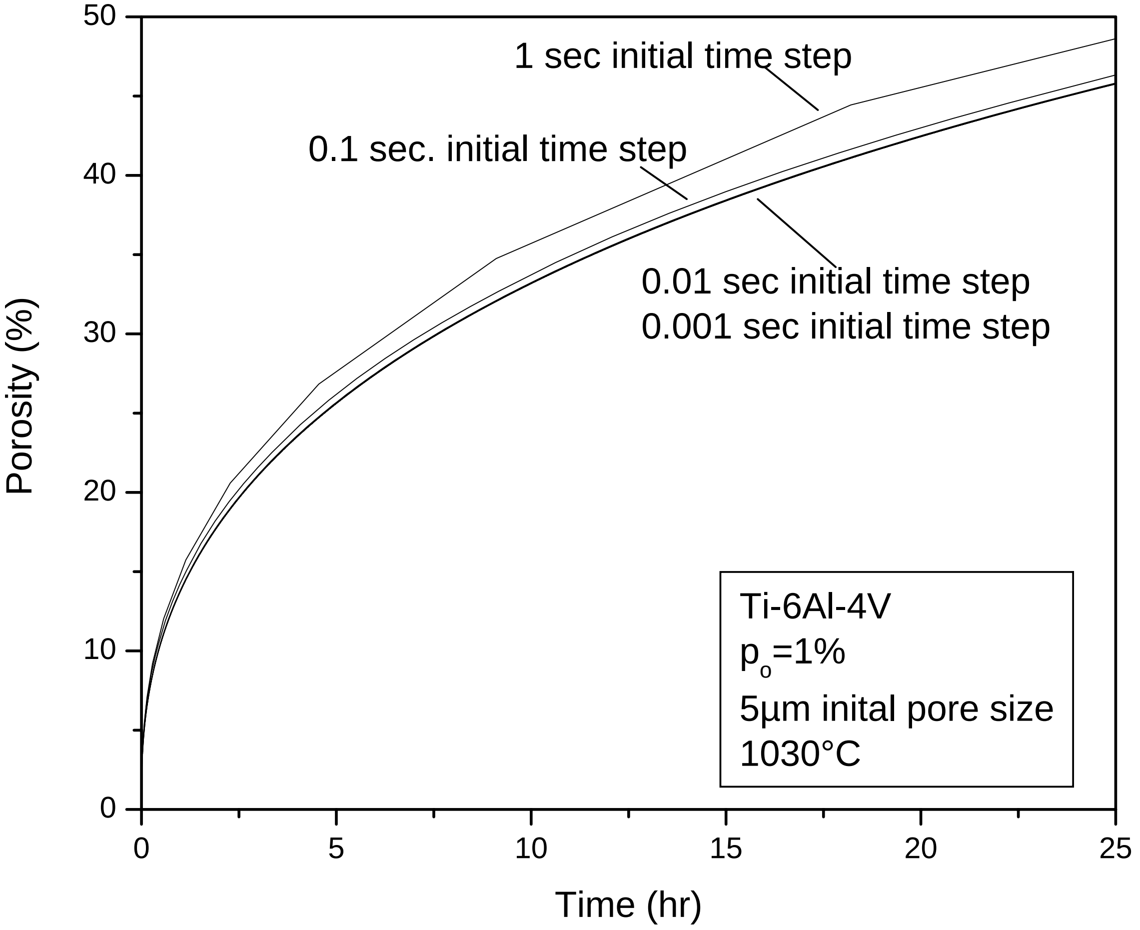

Figure 5.5. Changes in porosity vs. time with timestep showing convergence for Ti-6Al-4V.

5.2.4. Single Pore Model Comparison

Figure 5.6 shows a typical time vs. porosity curve for isothermal aging of Ti-6Al-4V comparing all three models, which are nearly identical to each other. Despite the simple nature of the pressure vessel model, it shows nearly the same results as the more complex finite element models. This is not nearly so surprising once one examines the output of the finite element models (figure 5.4 and 5.2) and sees the nearly spherical stress distribution. The same equivalence between the 2D axi-symmetric model and the analytic model had been seen before by Murray in CP-Ti aged at 955^{o}C [**39**]. Due to the equivalence of the approaches, and the relative ease and speed of the analytic approach, it was used for the rest of the experiments.

5.2.5. Analytical Model Extensions

As done by Murray [**39**], the basic analytic model described above can be modified with the addition of a superplastic expansion term for the thermally cycled samples. The basic analytic equation was modified with n=1 and a new pre-exponential A$_{TSP}$ was substituted. By the nature of the simulation each individual heating and cooling of the cycle is not examined, but rather a time averaged A$_{TSP}$ is calculated that is dependent on how fast the system is cycled. By taking the stress exponent as 1 and solving equation 5.4 the superplastic foaming equation is then:

$$\dot{f}_{TSP} = \frac{9A_{TSP}}{4} f \cdot P \tag{5.5}$$

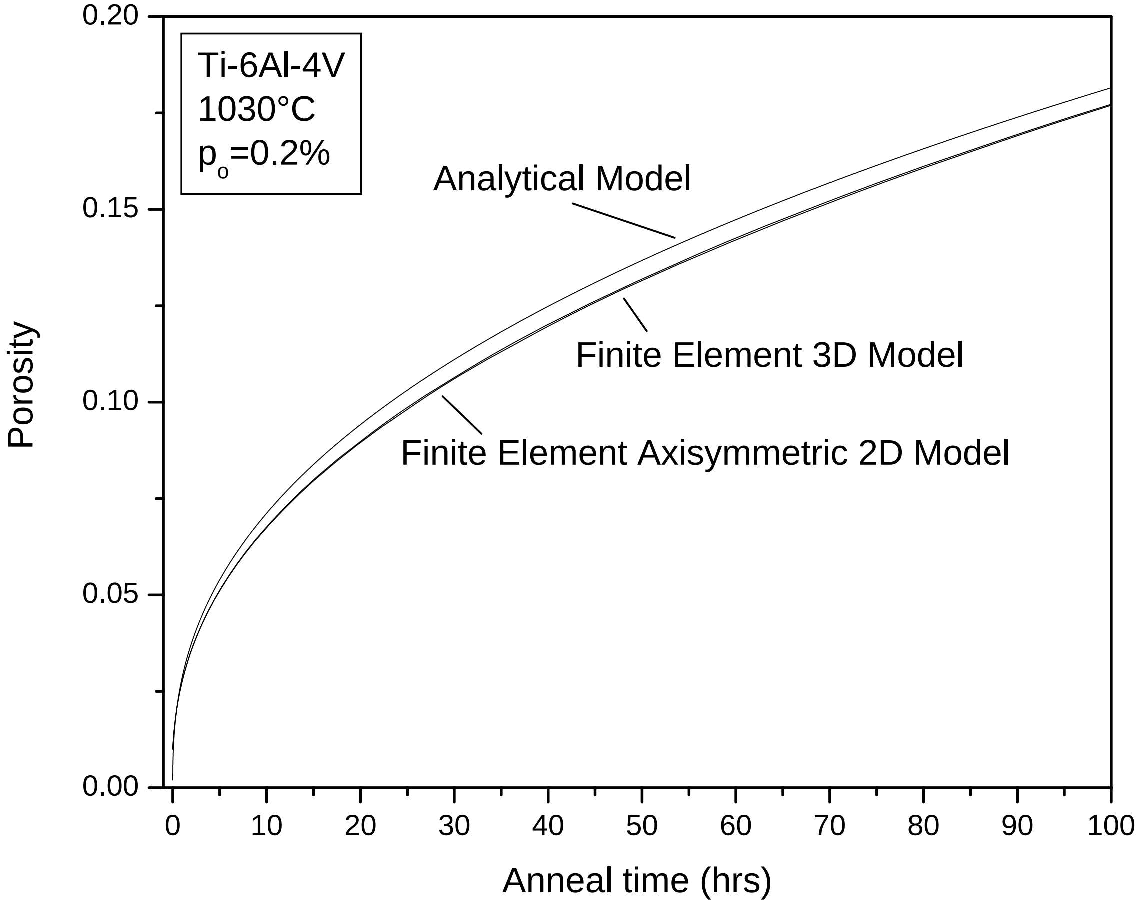

Figure 5.6. Porosity vs. time for the different models tested.

A more fundamental shift in the results of the simulation comes from the extra porosity that is found when one takes into account the argon density. This has the effect of raising the initial porosity and speeding up the calculated foaming.

The first major change in the analytic equation used previously by Murray takes into account the density of argon which had been previously neglected. This changes the initial porosity as described in section 3.1. Once it was found through a solution of the ideal gas law that the room temperature density of the argon inside the as-HIP'ed samples would be nearly half that of water (0.4g/cc), the validity of using the ideal gas law was questioned. Further research showed that, above 100 atmospheres of pressure, there is significant deviation from the ideal gas law. In order to take into account the non-linearities of high pressure gas, the Virial gas equation was used:

$$\frac{PV_m}{RT} = 1 + \frac{B}{V_m} \tag{5.6}$$

where P is the pressure, V_m is the molar volume, R is the gas constant, T is the absolute temperature, and B is a fitting parameter. B is determined by a Taylor type expansion and depends on three experimentally determined parameters:

$$B = a_1 + a_2\left(\frac{T_o}{T} - 1\right) + a_3\left(\frac{T_o}{T} - 1\right)^2 \tag{5.7}$$

For argon the following parameters were used a_1=-16 m^3, a_2=-60 m^3, and a_3=-10 m^3 [**84**]. These parameters, along with the Virial equation of state equation 5.6, were input into a Maple program. The series of equations was then solved for the pressure in the pore, as a function of the initial pressure, initial porosity, final porosity, HIP temperature and testing temperature. The equation is reported, along with the Maple code in appendix 0.4.

The effect of the change in initial porosity and the Virial gas equation on the porosity time curve can be seen in figure 5.7. When the non-corrected equation (eq. 3.1) was used a porosity of 0.54% was found for the 5.5 atmosphere backfill sample, but when the modified equation (eq. 3.2) is used 0.59% porosity is calculated.

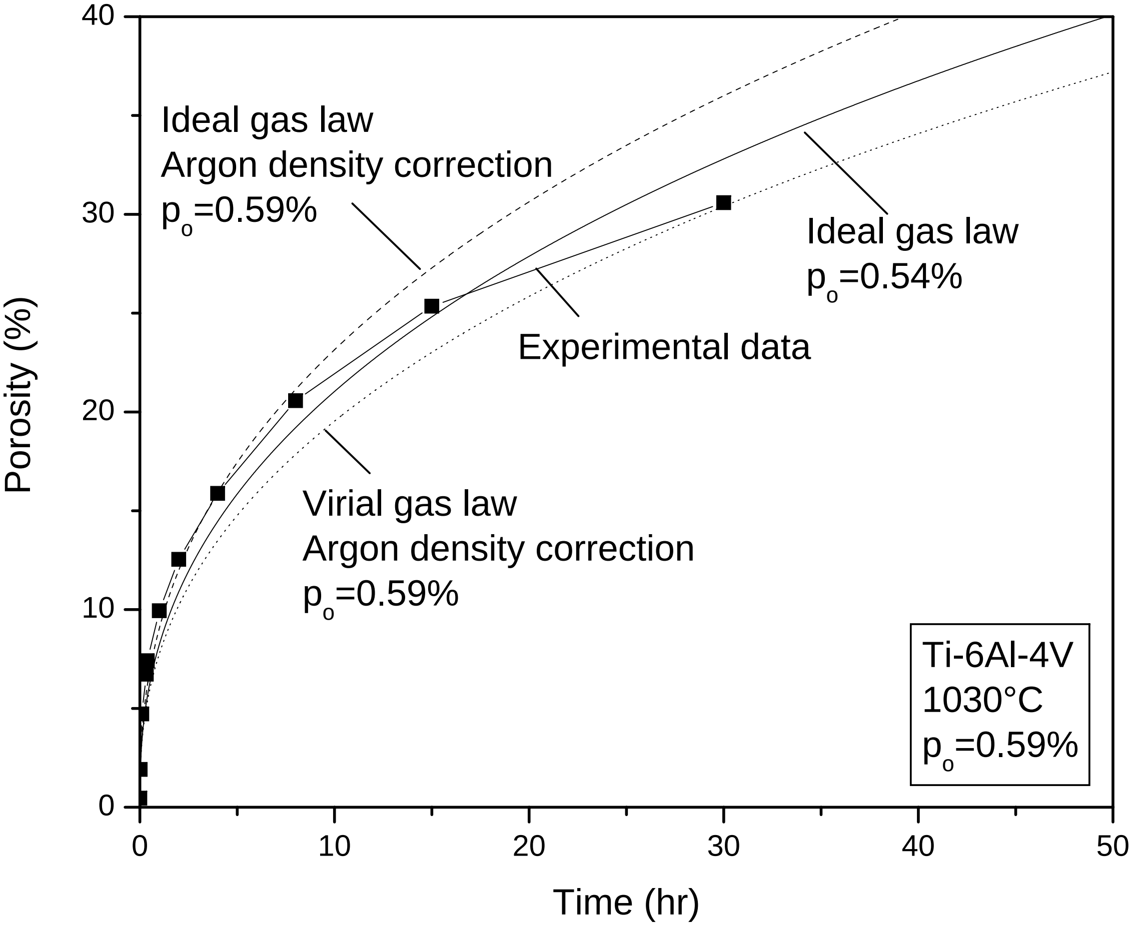

Figure 5.7. Graphs of porosity vs. time showing data for Ti-6Al-4V and predicted curves.

5.2.6. Simulation results

All of the previously described thermal foaming runs (shown in figures 4.3, 4.6, and 4.19) were simulated and the simulations are within a factor of 5 of the experimental in the worst case. The Ti-6Al-4V isothermal foaming simulations can be seen in figure 5.8, and simulations for thermally cycling can be seen in 5.9. Simulations for NiTi isothermally aged at 900^oC can be seen in figure 5.10. Each sample is labeled by its initial porosity, the initial pressure is taken as the HIP pressure (found in section 3.4), and unless otherwise stated uses the virial gas law equation. Experimental data are plotted only up to the point where porosity opens to the surface and gas is lost.

The simulations all give correct order of magnitude results, but they do not accurately reflect the experimental data. In particular, it was noticed that the smaller the initial backfill pressure (and therefore the smaller initial porosity), the more the simulation deviated from the experimental results. This implies that there is a non-linear effect based on the initial porosity, which leads to a model that depends on the length-scale of the simulations. This led to research on a size dependent effect identified as surface tension, which is discussed in the next section.

While the agreement between the models and the experiments are good for NiTi, it is reasonable in light of previous discussions on the highly clustered nature of NiTi porosity growth to question its validity (section 4.2.4). For this reason, foamed was modeled for the case of pore clustering through the finite element method, and it was found that clustering had little effect on the overall porosity. A full discussion of these modeling results is found in section 5.3.

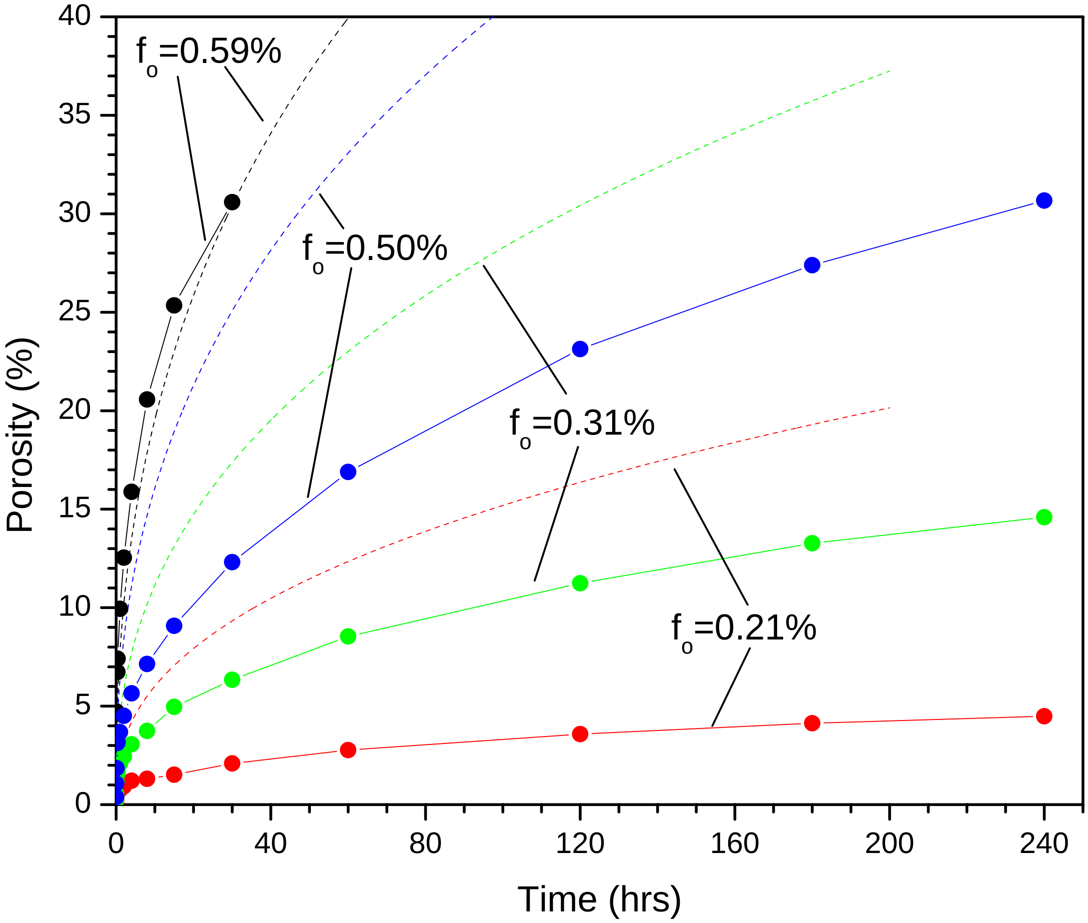

Figure 5.8. Simulated porosity (with Virial and Ar density corrections) vs. time of Ti-6Al-4V samples isothermally foamed at 1030^{o}C compared to experimental data.

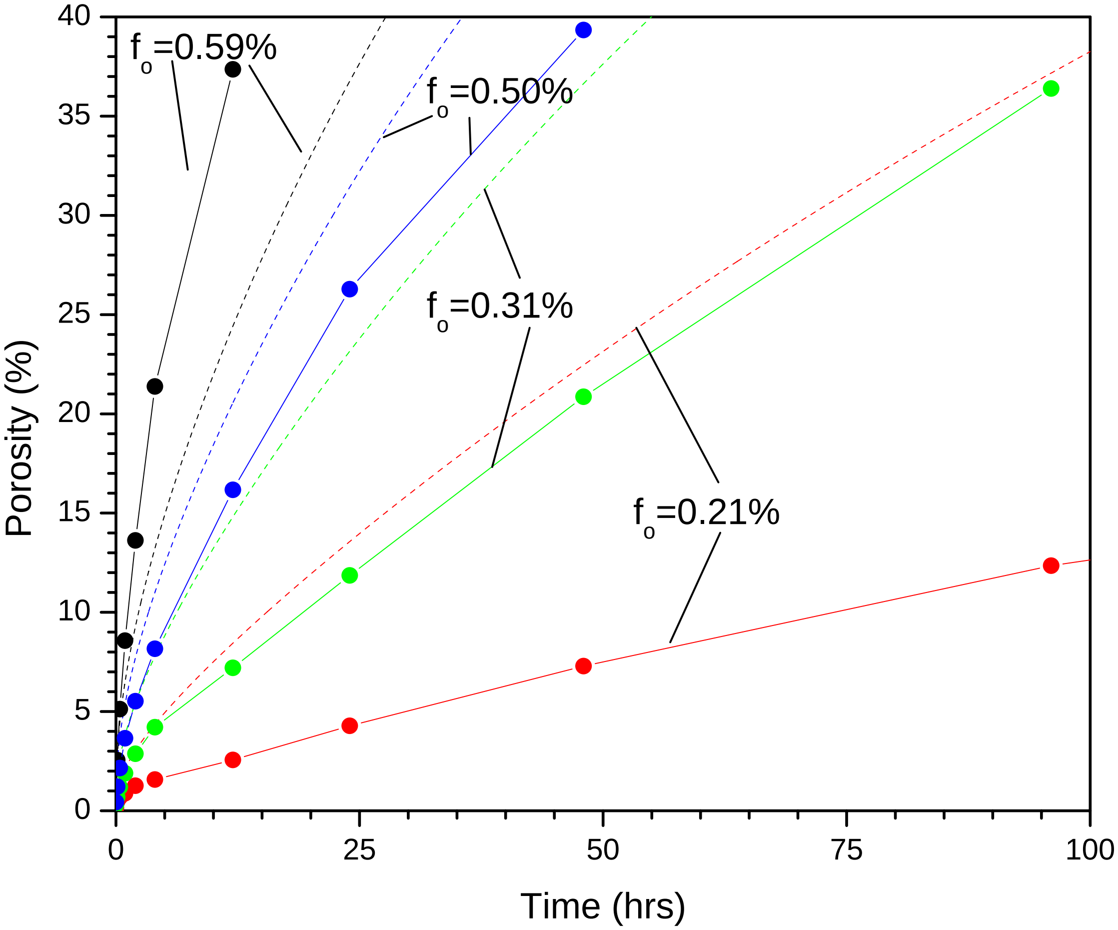

Figure 5.9. Simulated porosity (with Virial and Ar density corrections) vs. time of Ti-6Al-4V samples thermally cycled in 8 minute cycles between 840 and 1030^{o}C compared to experimental data.

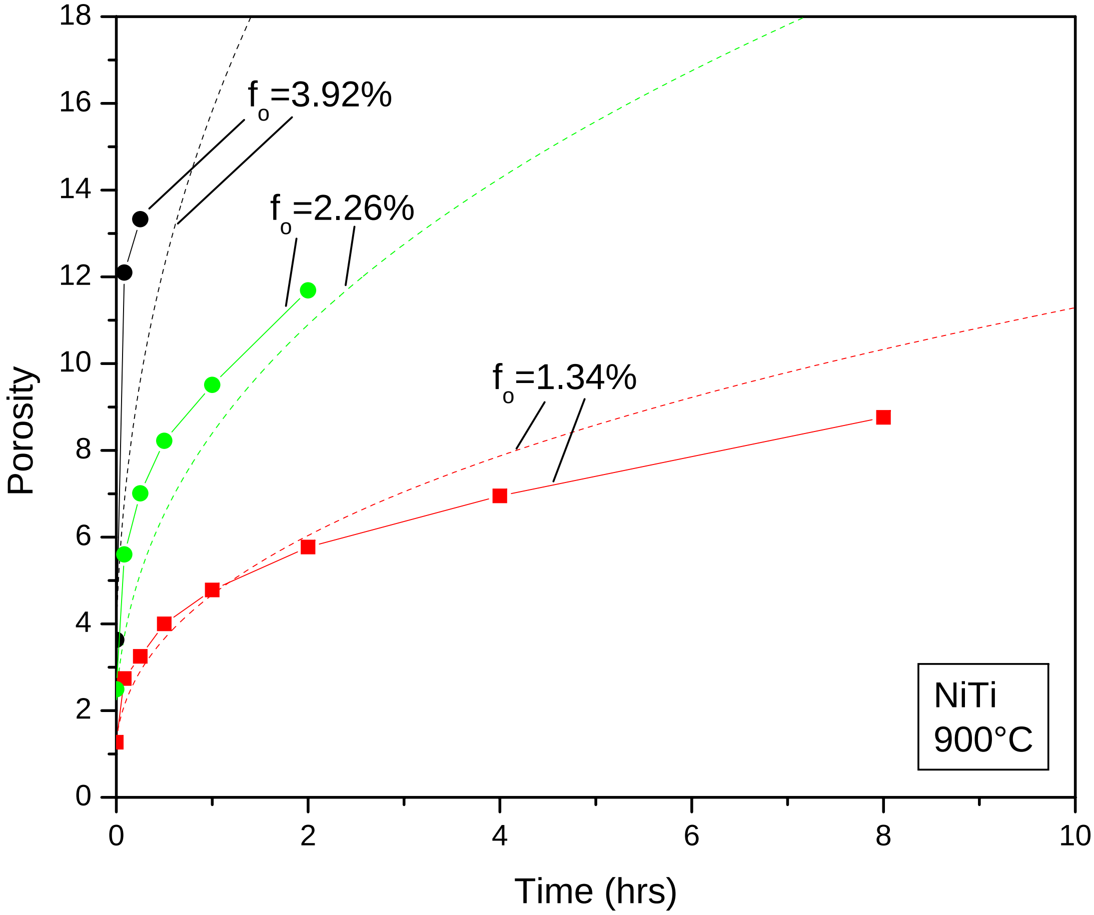

Figure 5.10. Simulated porosity (with Virial and Ar density corrections) vs. time of NiTi samples isothermally foamed at 900^{o}C compared to experimental data.

5.2.7. Surface Tension

The last major change made to the analytic model was to add a term for surface tension. It has been long known that materials can only sinter to a certain minimum porosity if there is entrapped gas. The sintering stops when the surface tension equals the internal pressure of the pore [**85**]. A related problem is found when using ion-implantation, or sputtering, which can insert helium, leading to blistering of the surface [**86**,**87**]. A similar situation is found in nuclear materials research, where helium is produced by the nuclear decay of tritium that has diffused in a metal (so-called tritides) [**88**, **89**]. In this case, as more helium is created in the material, internal pores will begin to grow and connect. In both the current study of trapped argon in pores and that of helium produced in-situ in metals, there is a pressurized gas trapped in a metal matrix that expands until it is balanced by the surface tension. As a spherical pore with radius r expands, its internal gas pressure drops off as a function of $1/\mathrm{r}^3$ while the surface tension drops as a function of 1/r, which means that there will always be a final equilibrium size of the pores (see figure 7.2), which must be accounted for in order to accurately simulate these systems.

In the current study, the additional surface tension term appears in two important places. It first appears in the internal gas pressure of the samples in the HIP, where the pressure of the gas within the pore is the sum of the HIP pressure and surface tension pressure term. The addition of this term means that the same volume has higher pressure, and therefore more gas, than previously assumed. The second place the surface tension appears is in the growth of the pore. The net driving force for growth is no longer just the internal pressure minus the external pressure, but now the pressure due to the surface tension must also be subtracted. For a spherical pore embedded in matrix, the equation for the pressure P_s due to surface tension is [**90**]:

$$P_s = \frac{2T}{r} \tag{5.8}$$

where T is the surface line tension term, and r is the radius of the pore.

The exact surface energy (which is equivalent to surface energy) of solids is difficult to measure experimentally, and there are often large errors associated with such measurements [**91**]. Even where data on surface tension in solids has been collected, it is most often pure metals that are examined [**92**, **93**]. It is much easier to experimentally measure the surface tension of materials in the liquid state, and there is a significant amount of data on pure metals and alloys in liquid form [**84**, **94**]. It is generally found that the solid surface tension is higher than the liquid surface tension [**91**]. Data for pure liquid titanium (1680^{o}C) was found to be 1.51 N/m, while the surface energy of solid titanium at 90K below the melting point was 1.70 N/m, or around 13% greater [**92**]. An even further complication is that of alloy composition and contamination. For example, just 1.5 monolayers of oxygen on aluminum can decreace the liquid surface tension by 20% [**94**]. As no data were found for Ti-6Al-4V, the data for pure Ti, 1.70 N/m, were used. No experimental data were found for NiTi either, and in this case there is no simple pure metal to use. Instead a series of approximations was used to create an order of magnitude estimation. The surface energy in liquids generally scales with melting point, and based on published surface tension and melting point trends [**94**], the liquid surface tension of NiTi would be 1.05 N/m. Further approximating the solid surface energy by using the previously found 13% liquid to solid surface tension correction yields a surface tension of 1.19 N/m for solid NiTi.

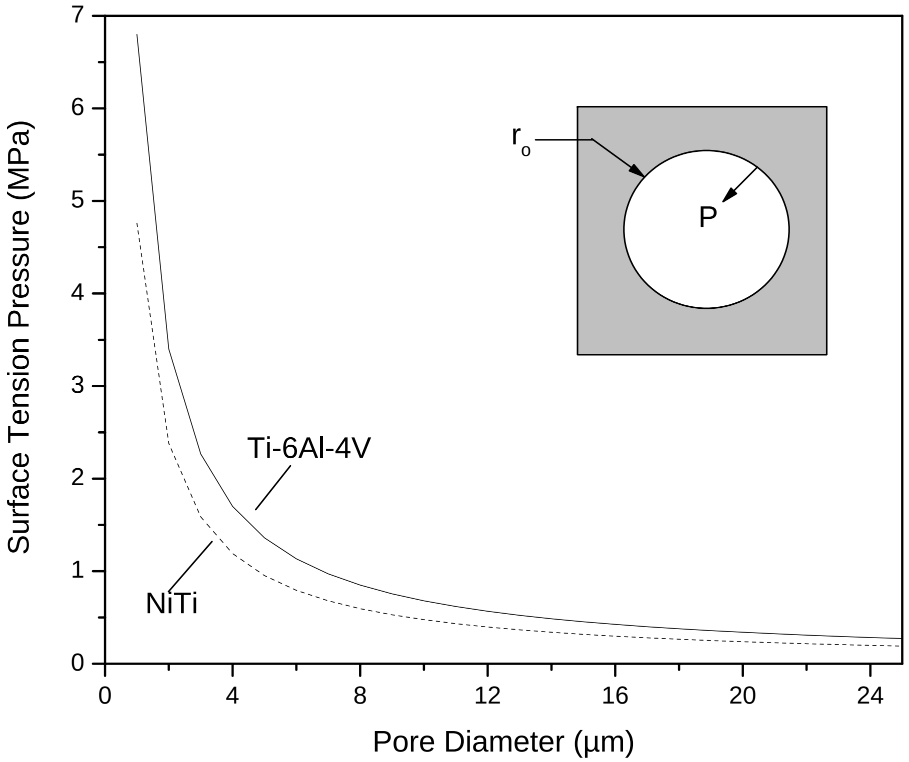

Figure 5.11. Plot of eq. 5.8 showing the surface tension pressure as a function of initial pore diameter.

The non-linear effects of very small droplets (or in our case small pores) can be ignored, as it is significant only in the nanometer regime [**95**]. With all of the approximations, the current study is mainly looking at the effects of surface tension on the overall growth of the pores. The pressure due to surface tension calculated from equation 5.8 for both Ti-6Al-4V and NiTi can be seen in figure 5.11. For pore diameters below about 6 μm, the surface tension pressure is significant, as compared to the HIP pressure of 100 MPa.

This consideration introduces a length-scale dependence, where previously, this was a dimensionless model whose output was independent of pore size. The effect of the addition of the surface tension term on the evolution of porosity can be significant for small initial

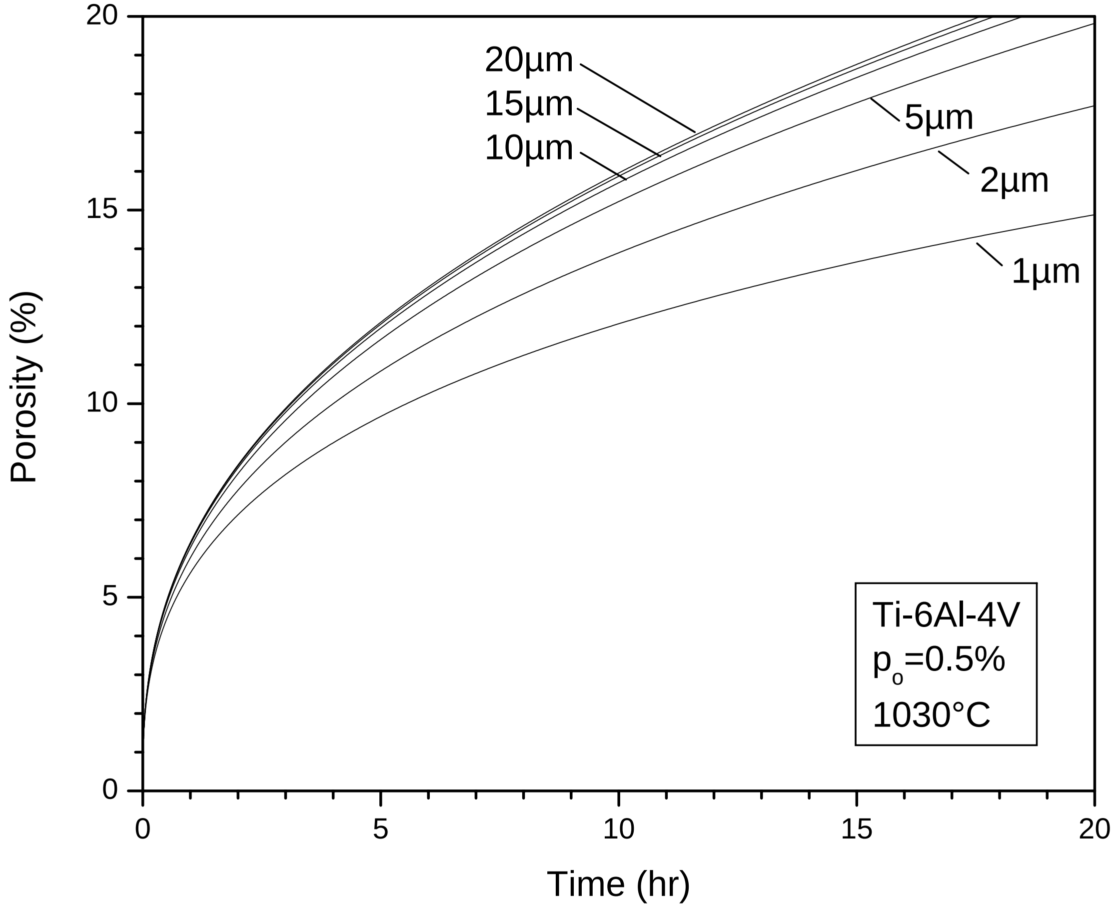

Figure 5.12. Simulated porosity vs. time for Ti-6Al-4V with 0.5% initial porosity, at 900^oC with varying initial pore sizes.

pore sizes. Figure 5.12 shows how changes in initial pore size change the foaming rate for Ti-6Al-4V, with 0.5% initial porosity and 100 MPa HIP pressure.

In section 4.1.2, each of the four high pressure Ti-6Al-4V samples were sectioned at around 10% porosity in order to determine the pore distribution. Pressure vessel simulations of the four 10% samples used for image analysis were preformed, and a relationship between the final radius (r_f) and the initial radius (r_i) was found. The relationship is linear in all of the cases, as shown in figure 5.13. Outside of the smallest pores (pores

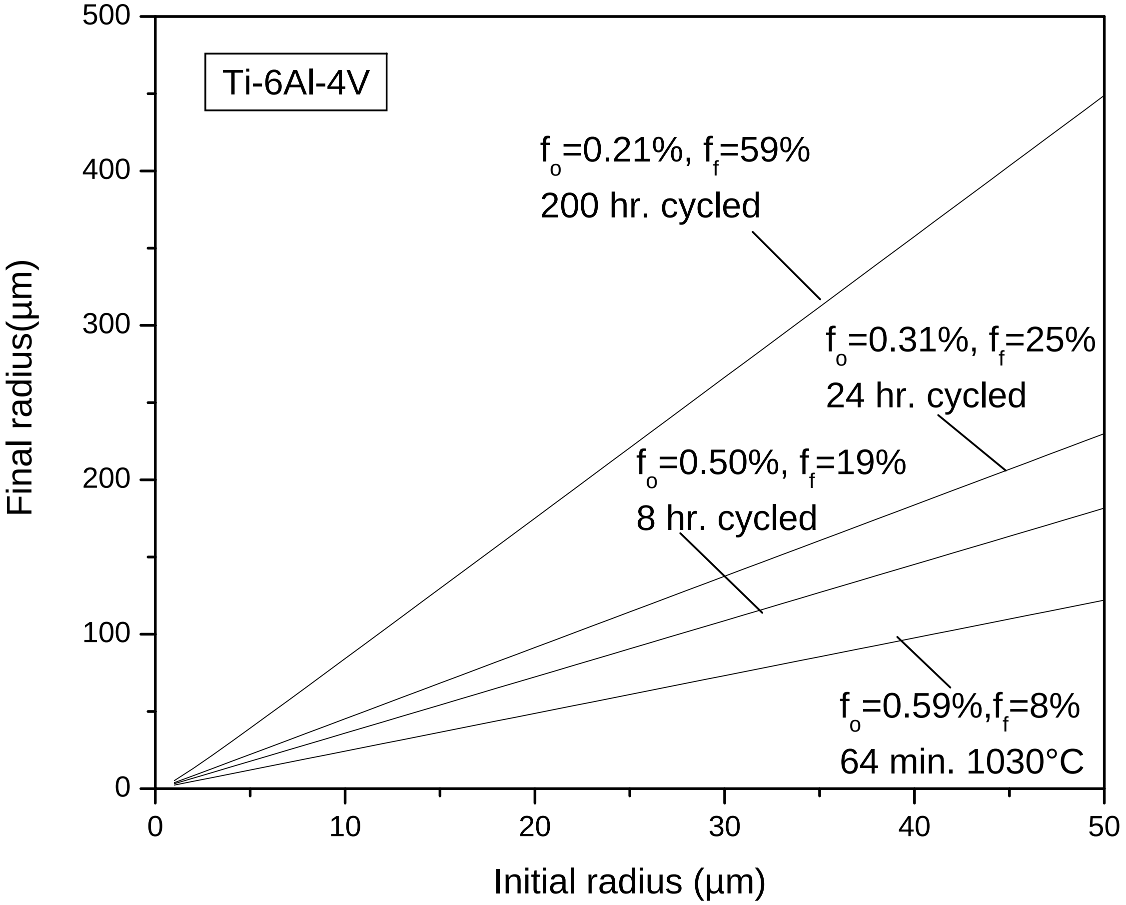

Figure 5.13. Simulated final pore radius vs. initial pore radius for the four imaged 10% samples. Cycled samples were 8 minutes per cycle, from 840-1030^{o}C.

less than 1 μm have large surface tensions) the linearity is perfectly reasonable as the porosity is proportional to the pore volume, and therefore pore size increase is directly proportional to initial and final porosity. The distributions of pore sizes in the as-HIP'ed state were then calculated for each of the four initial pressure samples. The as-HIP'ed normalized number density distributions can be seen in figure 5.14.

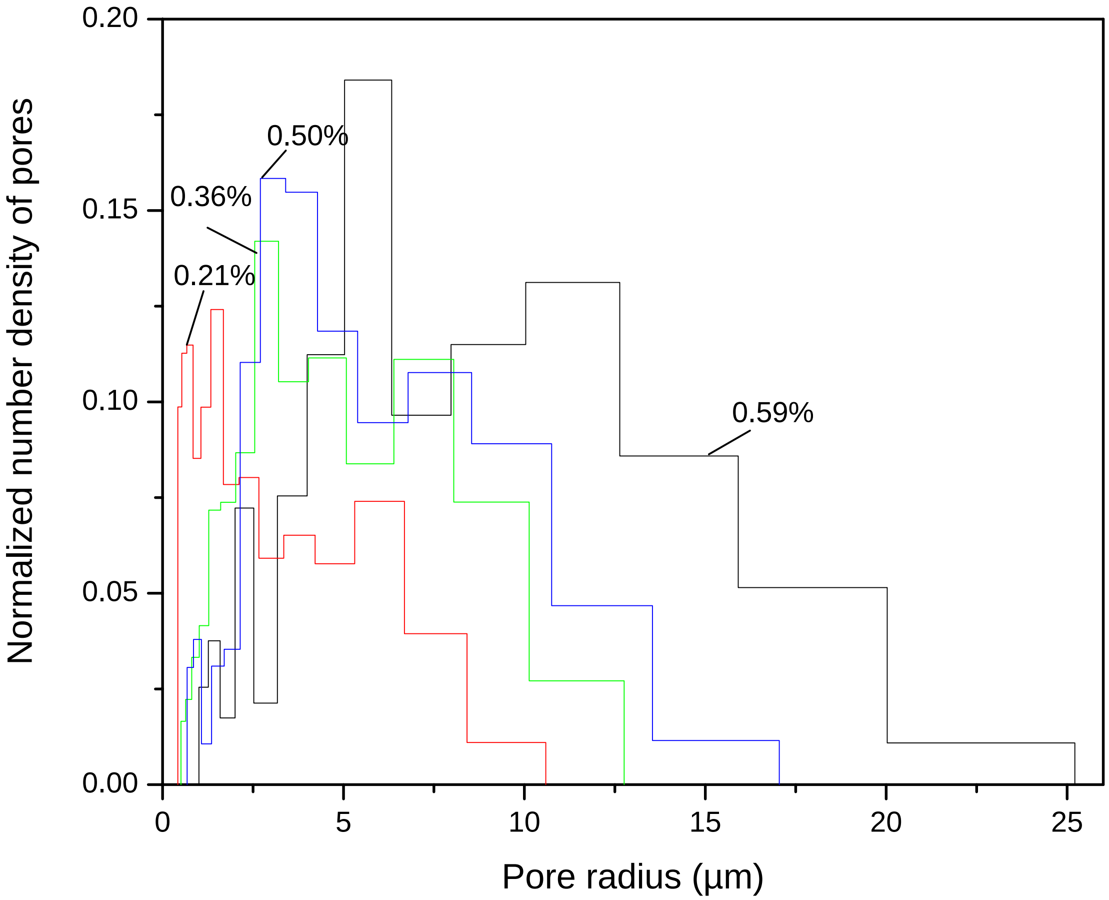

Figure 5.14. Calculated distribution of pores before foaming HIP for the four Ti-6Al-4V samples.

Next the volume fractions of each pore group were found through image analysis and Saltykov analysis as described in 3.9. This normalized volume fraction as a function of pore radius can be found in figure 5.15.

Using this as a starting point, simulations were run forward from the expected sizes of the pores in the as-HIP'ed state. A series of these curves for an initial porosity of 0.36% can be seen in figure 5.16. They show each of the different initial pore sizes and their

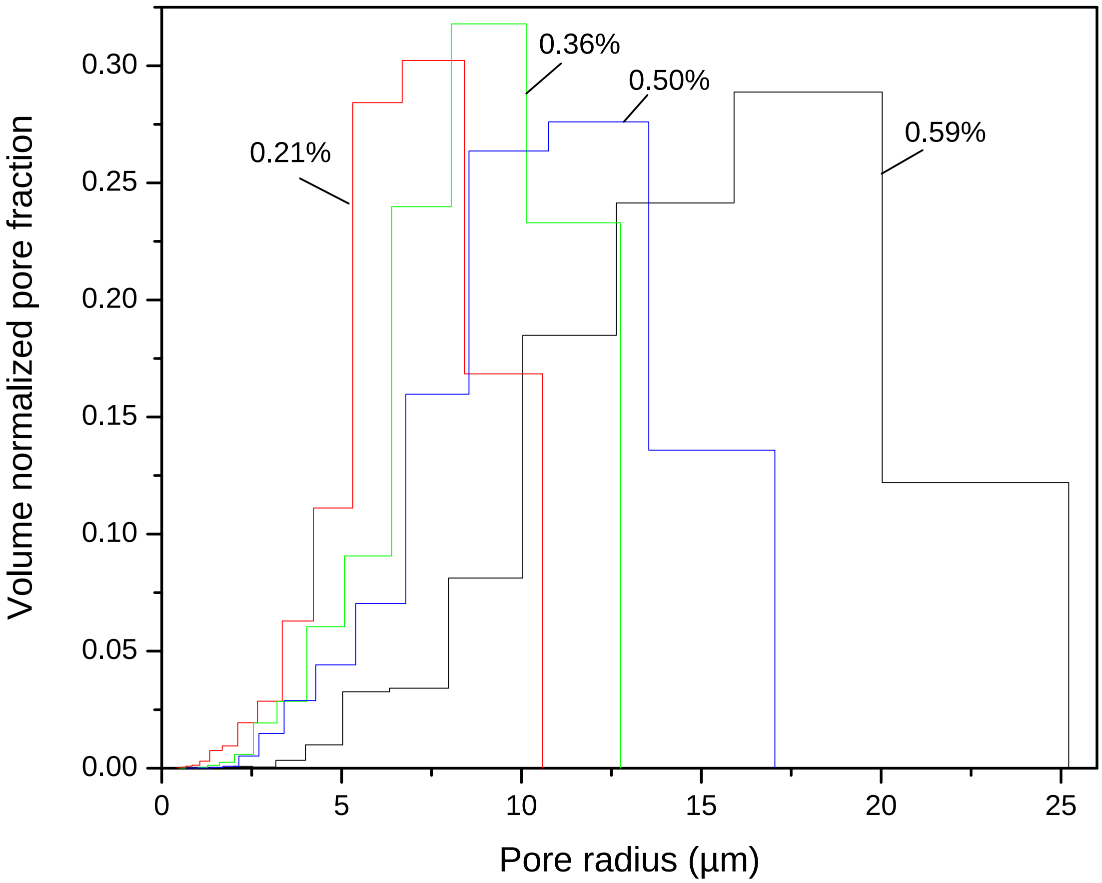

Figure 5.15. Normalized volume distribution of pores after HIP for the four Ti-6Al-4V samples.

growth rates. Each curve was then multiplied by the initial volume fraction as per:

$$\dot{f}_{tot} = \sum \dot{f}_i \left(\frac{f_{i_o}}{f_o} \right) \tag{5.9}$$

where $\dot{f}_{tot}$ is the foam porosity increase rate, i is the bin number, $\dot{f}_{i_o}$ is the porosity of bin i at the start, and f_o is the initial porosity of the whole foam. It was then assumed that the growth in total porosity was proportional to the initial volume fraction. Each of

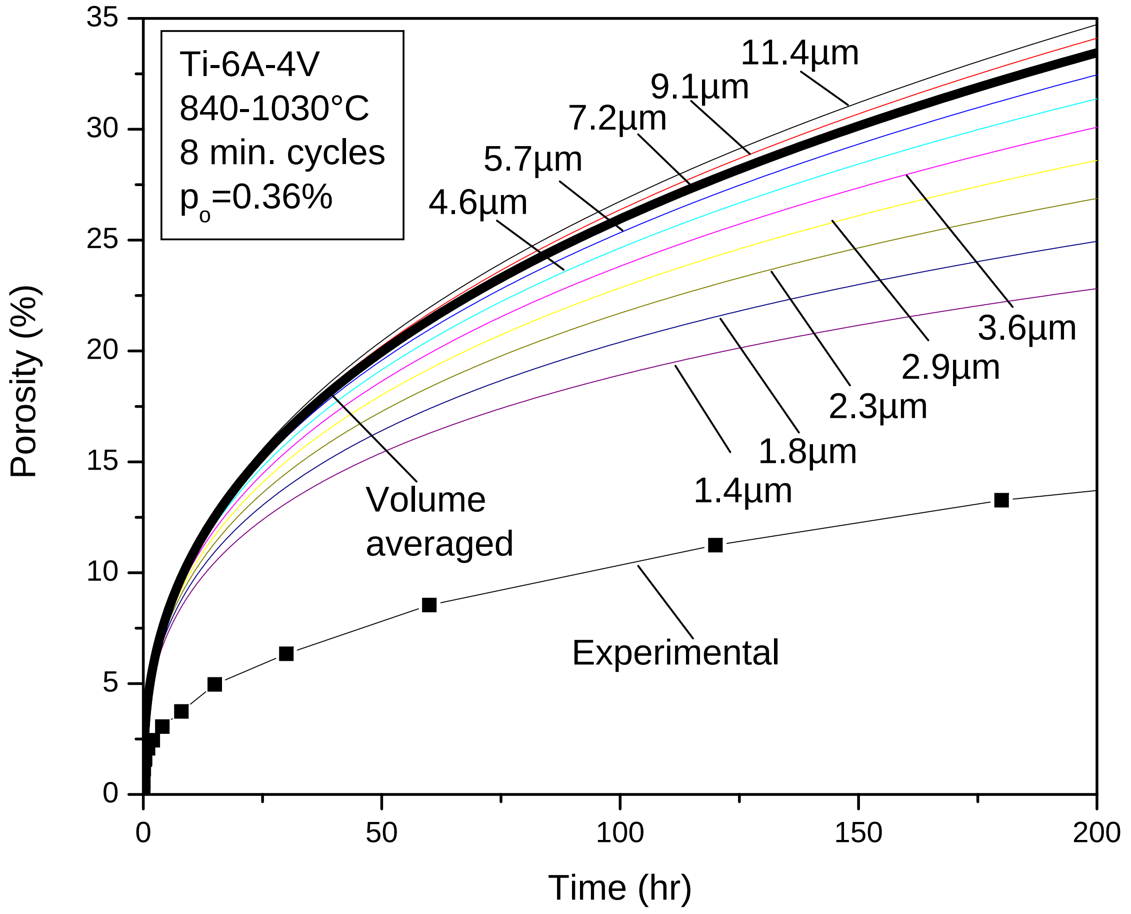

Figure 5.16. Series of porosity vs. time curves for the radii found in the pore analysis for f_o=0.36%. The bold line is the volume averaged creep rate.

the pore bins was then normalized and summed. The bold line in figure 5.16 shows the expected foaming for whole sample.

The simulation still does not accurately reflect the porosity increase observed in experiments. This could be due to an internal error, or to other effects such as early connecting of pores. The lack of agreement for the smallest porosities is poorly understood.

5.2.8. Graded Porosity NiTi through Rapid Cycling

Thermally cycled NiTi was discussed briefly in section 4.2.3, but simulation allows the ideas presented there to be explored further. The average temperature was found earlier to be 761^{o}C, but due to the exponential nature of creep with temperature, a second measure of temperature is needed. By integrating the Arrhenius part of the creep equation, the effective temperature can be calculated as:

$$T_{eff} = \frac{1}{\Delta t} \int_{t_1}^{t_1+\Delta t} exp - \frac{Q}{RT(t)} dt \tag{5.10}$$

where Δt is the time per half cycle, t_1 is the starting time, Q is the activation energy (155 kJ/mol for NiTi), and T(t) is the time-temperture function show in figure 4.20.

For the specific thermal cycle used in the experiments described in section 4.2.3, the effective temperature was found to be 861^{o}C by numerical integration of equation 5.10. These two temperatures with their associated creep rates can then be used to simulate the creep expansion of the material. Figure 5.17 shows the porosity evolution that would be expected for the top part of the sample which is subjected to the effective temperature, and the bottom which creeps at the average temperature. Assuming that the whole sample was isothermally foamed at the effective temperature, the predicted time to foam to 4.36% would be 34 hours, while foaming to 5.35% would take 59 hours. The bottom is foaming faster than would be expected if it were at the average temperature. This is probably due to the sample is not being long enough, or the cycling rate not fast enough for the bottom to be at the average with the thermal diffusion of NiTi. Rather it is seeing

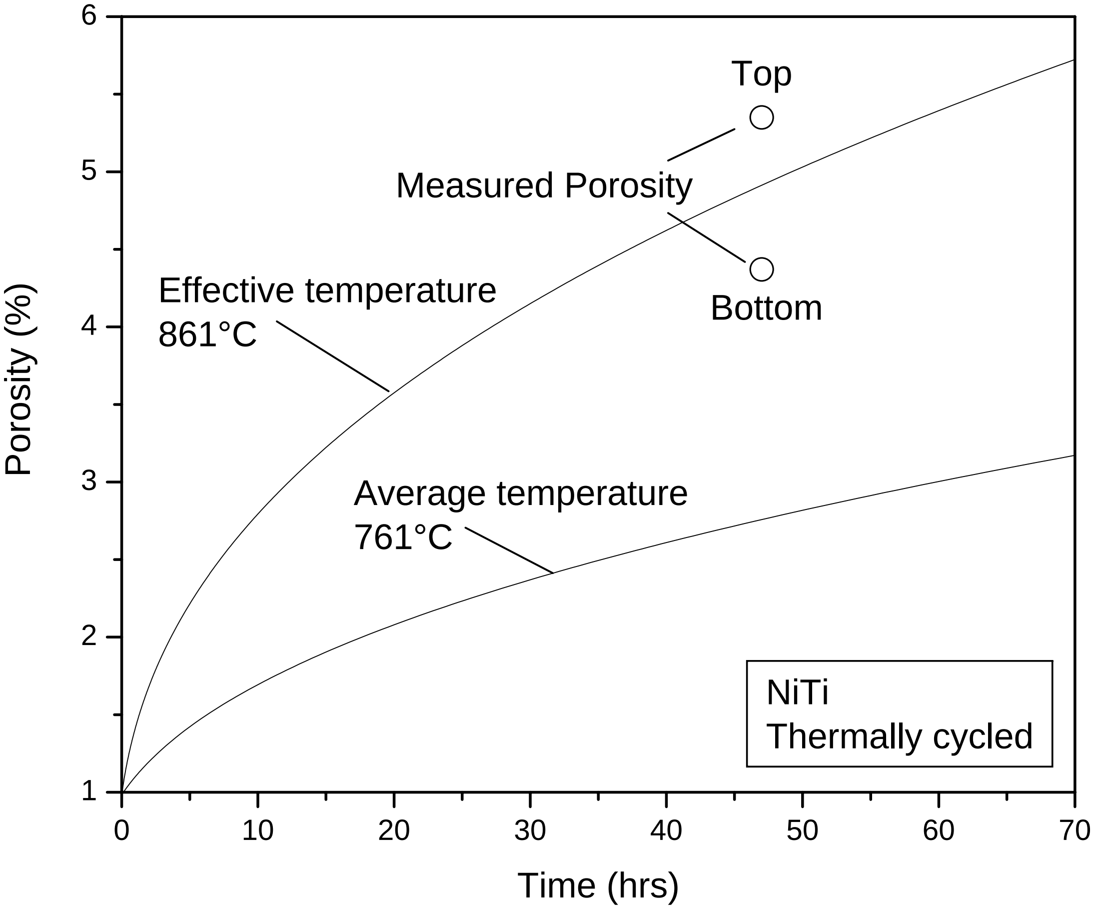

Figure 5.17. Simulated porosity vs. time of NiTi for both the effective and average temperatures in the thermally cycled sample. Open circles represent the porosities of the bottom and top of the sample.

a dampened cycle that is lowering the overall creep rate, but not the lowest possible average temperature creep rate.

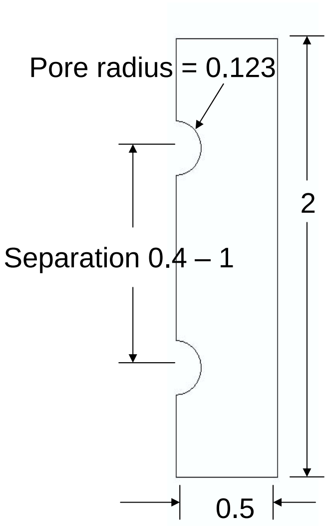

Figure 5.18. Model system for the 2-pore interaction model.

5.3. Multiple Pore

Even with all of the additions, the analytical model does not fully match the experimental data, and one possible explanation is that local pore clustering around primary powder particles could lead to a change in the foaming rate. By clustering two pores, there should be larger overlapping stress fields which may influence the pore growth. This effect was examined in simulations using the finite element method. Axi-symmetric models were created with the same elements described in section 5.2.2, the actual mesh is not shown as nearly 20,000 elements were used and individual elements can not be visually discerned. In this case, a 2-pore vertical model of Ti-6Al-4V, with varying distances between pores was used. A diagram of the model can be seen in figure 5.18.

In order to look at just the pore clustering effects, the analytical enhancements to the model were not used (Virial gas equation and surface tension). Probing the effect of local pore clustering was performed by reducing the distance between 2 pore pairs that were situated in a repeating structure (described more fully in 5.2.2). Figure 5.19 shows the growth of the smallest and largest separations. Overall, there is not much change in the appearance of the expansion. In the simulation with the smallest separation, the two pores have strong overlapping stress fields. The 2 pores have a stress distribution that is very similar to that of one larger pore. Figure 5.20 shows the simulated expansion curves. The slightly faster foaming rate of the closest spacing is most likely due to the highly ordered “sheet” of pores expanding in the vertical direction. This exaggerated growth in one dimension due to ordered planer structures has been seen in previous simulation studies on CP-Ti under isothermal and TSP creep conditions [**60**].

Even with the unrealistic high stretching in one dimension, there is little difference in the foaming rates between clustered and non-clustered pores. For this reason, the previous results on simulation of NiTi foaming can be believed. While the pores are undoubtedly clustered around the previous powder particles the overall porosity should increase in much the same way as for the case where the pores are non-clustered, at least up to the point where connection between pores occurs. Such connections are expected to occur at a lower overall porosity in the clustered case, since the local strain in the wall separating two clustered pores is very high.

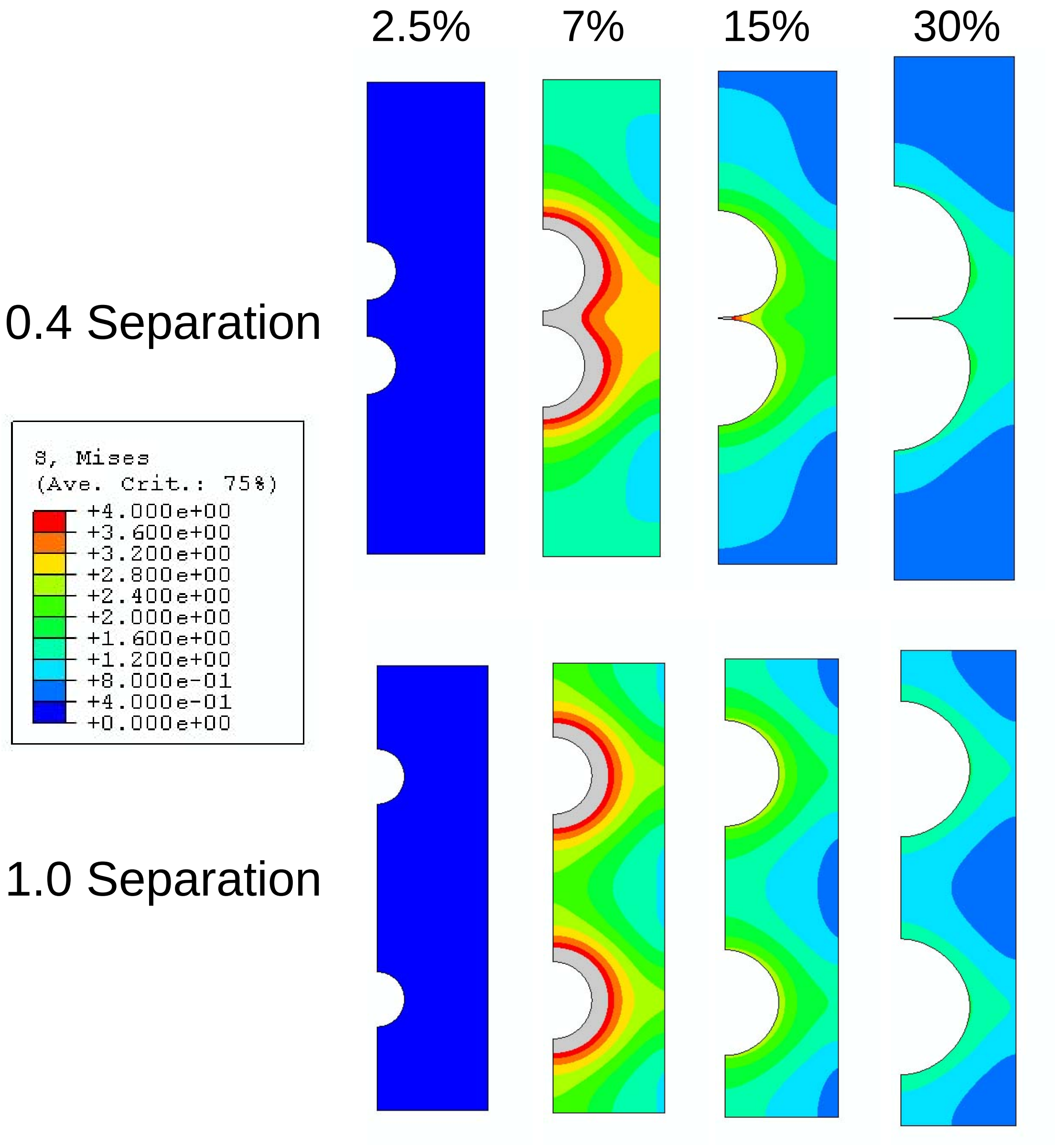

Figure 5.19. Axisymmetric finite element models of Ti-6Al-4V showing the differing stress fields for different separations. Separations are in terms of unit cells, of which 2 are simulated.

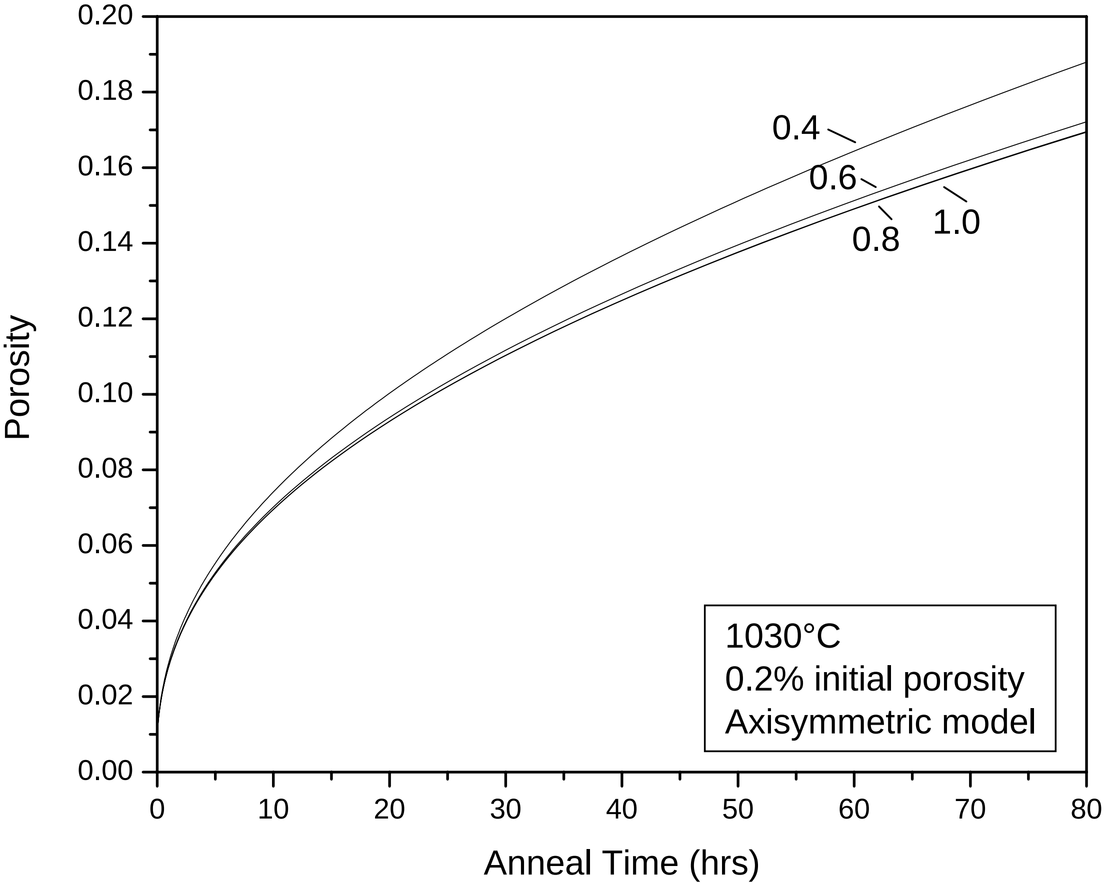

Figure 5.20. Foaming curves of Ti-6Al-4V for different pore separations, shown in terms of pore unit cell.

CHAPTER 6

Conclusions

Gas entrapment through HIP of a powder and argon created a foamable perform in both Ti-6Al-4V and NiTi. Through use of liquid nitrogen to cool and condense the argon, high pressure backfill of argon was made possible, which in turn lead to high initial porosities. Foaming of the pores was accomplished with a high temperature heat-treatment that allowed the pores to expand through creep of the matrix.

For both materials studied, increasing the initial porosity by increasing the entrapped argon, led to faster foaming rates. Even further increases in foaming rates were achieved in Ti-6Al-4V through the use of transformation superplasticity, but the enhancement is not as high as previously seen with unalloyed titanium [**60**] due to the more sluggish transformation kinetics of Ti-6Al-4V.

The maximum porosity achieved in Ti-6Al-4V and NiTi were 52 and 16%, respectively. The much lower value achieved for NiTi was explained by the inability to use transformation superplasticity and by the presence of oxide within the preform, allowing early connection of pores to the surface and subsequent escape of the gas. Despite the low pore fraction and size, unsuitable for bone ingrowth, NiTi foams had very low moduli useful for implants. Also, graded porosity could be achieved through thermal cycling.

The simulations of the foaming process, considering a single pore expanding in a creeping or superplastic matrix, were improved as compared to prior studies ref by taking into account the argon density, non-ideal gas equation, and surface tension effects. While these improvements should provide more accurate results, modeling was successful only for NiTi foaming and for Ti-6Al-4V foams at high initial porosity Ti-6Al-4V. This discrepancy for low-porosity Ti-6Al-4V foams may be due to pore connecting effects and errors in the surface tension determination.

Compression of NiTi foams performed simultaneously with synchrotron x-ray diffraction showed that it is possible to determine the phase fraction of stress-induced martensite as function of applied stress on the foam. The samples showed a large recoverable strain of 5%. On loading the transformation was nearly linear in the beginning, but dropping away as more plastic deformation accumulated. On unloading, a large hysteresis was found in the transformation vs. strain plot, unlike what was found previously for solid NiTi [**78**]. This hysteresis was attributed to both plastic deformation at stress concentrations in the foam and the intrinsic tension-compression asymmetry in NiTi transformation properties.

CHAPTER 7

Suggestions for Future Work

7.1. Surface tension determination

As discussed in section 5.2.7, the surface tension of solids is difficult to experimentally determine. However, there exists a simple and powerful way to do exactly that using the growth of pores. By making a foam with small amounts of porosity that are widely distributed (using large powders), individual pores could be measured using x-ray imaging. Since the size and HIP pressure are known, the pore can be allowed to grow and the terminal size calculated by solving the exponentially decreasing pore size vs. time function. This allows for the calculation of the surface tension on the pressurized pore. This only works if the pores are well separated and can be measured before and after growth (or even in-situ). By examining a larger section, many independent pore growth measurements can be conducted at once, which would allow a much more accurate surface tension to be calculated. A further bonus is that this can be used for nearly any solid that can be densified and crept. Such single pore experiments would be a good approach to both examine the growth process in more depth as well as to explore other fundamental material properties.

Using the above method to determine the surface tension allows one more important determination. In the above, the creeping material is treated as just a very viscous liquid, and it is the exponential asymptote that is important. Using the known driving forces and experimentally measuring the time constant of the growth, the fundamental creep parameters can also be solved for. Again with the number of simultaneous experiments that could be conducted by using samples with a multitude of pores, whole deformation maps could be generated with a series of experiments preformed at various temperatures using this method.

7.2. Multi-pore simulation

While early results indicate that in most respects multiple pores do not interact significantly, a high number density of pores might act differently than a lower number density. Small, slow growing pores have much higher pressure than their large counterparts due to surface tension. If a number of small pores connected, the resulting larger pore would overcome the local surface tension and grow faster than if they were separate. Such simulations would by necessity need to include both sintering closure of pores as well as growth.

Also, even after such simulations are accomplished, the overlapping stress fields could also be more important than expected. A partial finite element model with surface tension and the modified equation of state would be a good way to simulate the coalescence of the pores, which may lead to a more accurate description of the overall growth of the material.

7.3. Cladding

One way to improve the performance of the foams would be to achieve higher porosities. Since it is the escape of the argon that ends the foaming process, delaying the final connecting of the pores to the surface could help increase the total porosity.

Two approaches to achieve this goal are presented. First, limiting the path of the pores should make it more difficult for them to connect to the surface. This could be done by introducing foils into the powder compact before HIP'ing. This would create a much more tortuous path for the gas to escape, and possibly delay connecting with the surface.

Second, the argon might be delayed from connecting to the surface by enclosing the surface of the expanding compact in a thick layer of metal. As already proposed by the Low Density Core (LDC) approach [**96**], the canning material can be made of the material to be foamed (or a double canning if contamination is an issue). In this case the system is foamed with its cladding still intact which would keep the argon in the compact for a much longer time. This could be very useful for making higher porosity NiTi foams, since pores tend to connect early in the foaming process. A second way to achieve the same outcome would be to insert a small section of as-HIP'ed material into a well machined tube. The initial expansion would push against the walls of the tube and diffusion bond, and the whole compact would then expand as one.

7.4. Fatigue testing

For use as a bone replacement material, the fatigue properties of porous Ti-6Al-4V with and without bone become very important. Corrosion fatigue may become a major problem in the lifetime of bone implant materials, as foaming introduces pores that act as crack initiation sites. One possible mitigation of the enhanced cracking is that the material is meant to be used as a composite with bone which would carry stress. For this reason, tests would need to be preformed both with and without the second phase.

7.5. Alternate foaming agents

This dissertation has focused solely on using entrapped argon to foam materials, but there is no reason that other blowing agents could not be used. One idea in specific is to use, as blowing agents, alkaline metals that have no solubility in Ti, NiTi and many other metals. By using Mg, Na, K, or Rb, large amounts of material could be put into the compact as a powder and heated to the boiling point of the alkali metal, which would then push open pores. This idea is similar to using argon but is improved because the pressure in the pore will remain constant, as long as solid alkali metal exists, instead of dropping as the radius increases. Figure 7.1 shows calculated foaming curves for CP-Ti at 1200^{o}C of the above mentioned metals with the given vapor pressures [**84**].

A problem with this method is that the small initial pores have a high surface tension pressure that could cancel the pressure of the alkali metal blowing agent. A possible solution might be to use a dual approach and have argon as well as the metal in each pore. The high pressure argon would give an initial boost in the porosity and lower the surface tension pressure. Once the metal vapor pressure is larger than the surface tension, the solid (or liquid) metal vaporizes. Since there is a reservoir of solid or liquid metal the pressure never drops even as the pore expands, which could allow for foaming to higher porosities than would be possible for just argon. A schematic of the pressures as a function of pore radius can be seen in figure 7.2.

7.6. Rapid cycle foaming

As discussed in section 4.2.3, rapid cycling could be used to generate graded structures. This method shows promise, and better materials, times, and heating rates could be used

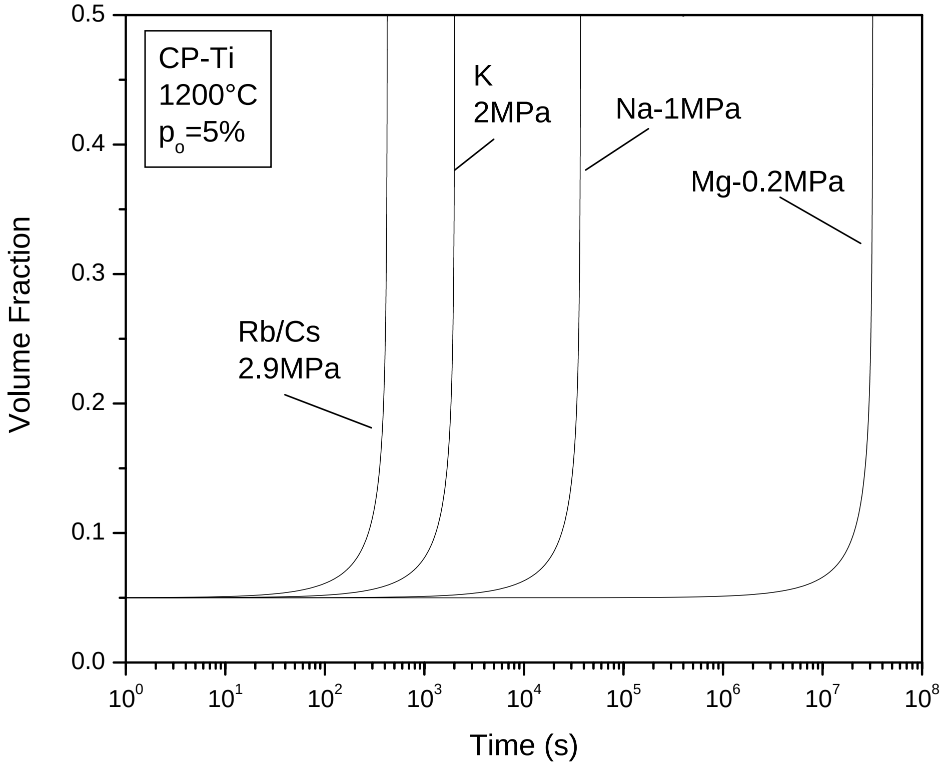

Figure 7.1. Alkali metal blowing agents showing simulated porosity vs. time curves.

to enhance the process. Other ideas such as cladding could be used together with rapid cycling to get larger total porosity, and more significant gradients in the porosity.

Another way to achieve graded porosity would be directly through application of a temperature gradient. Such a gradient could be created through natural gradients in a furnace, or more directly imposed by inserting some sort of active cooling into a sample (such as a liquid or gas cooled center of a long rod).

7.7. Porosity through hydrogen chemical reaction

Hydrogen has a high diffusivity in most metals that could be used to react a second phase to liberate a gas. Having an oxide that reacted to form water is one example. By

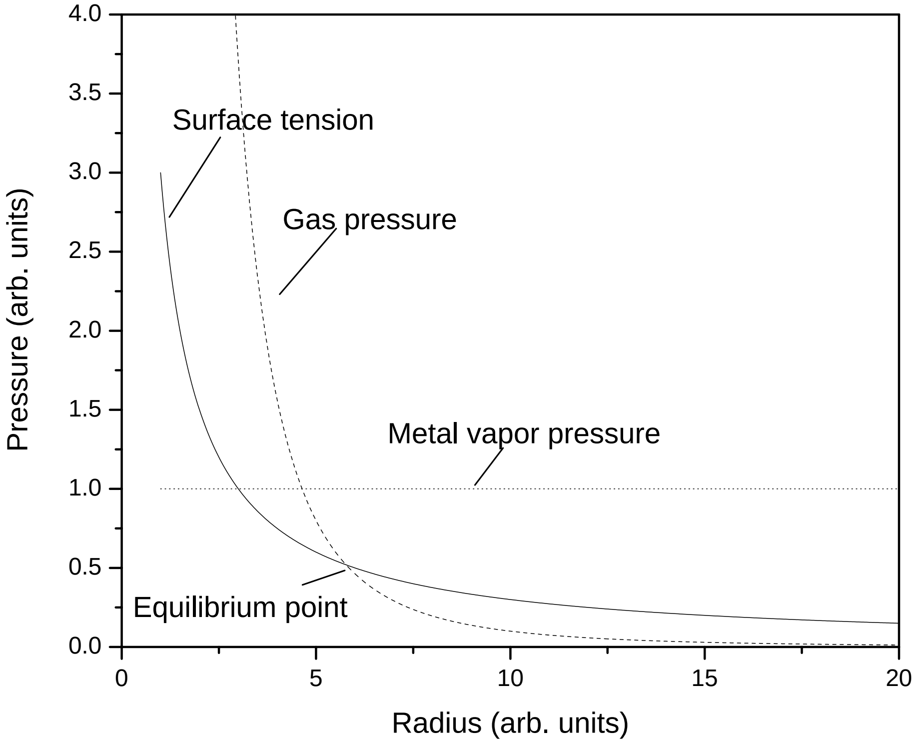

Figure 7.2. Pressure vs. pore radius schematic showing the pressure of surface tension, argon gas, and alkali metal gas (the equilibrium point is where foaming would stop without alkali metal gas).

including the oxide and then adding hydrogen at high temperature, water vapor would form inside the material, creating a pressurized pore that could then grow. An example is Cu containing small CuO inclusions. CuO is reduced to form H_2O that grows a bubble. This effect is known as "hydrogen sickness" in oxygen-rich copper that forms blisters upon exposure to hydrogen [**97**].

References

[1] L.J. Gibson and M.F. Ashby. *Cellular Solids*. Cambridge University Press, Cambridge, 1997.

[2] A. G. Evans, J. W. Hutchinson, and M. F. Ashby. Cellular metals. *Current Opinion in Solid State & Materials Science*, 3(3):288–303, 1998.

[3] AerospaceNotes. Porous titanium structures. *Aircraft Engineering and Aerospace Technology*, 71(3):269–269, 1999.

[4] MRSBulletin. Quick notes section. *MRS Bulletin*, 2002.

[5] A. Bhattacharya and R. L. Mahajan. Finned metal foam heat sinks for electronics cooling in forced convection. *Journal of Electronic Packaging*, 124(3):155–163, 2002.

[6] P. S. Liu, B. Yu, A. M. Hu, K. M. Liang, and S. R. Gu. Development in applications of porous metals. *Transactions of Nonferrous Metals Society of China*, 11(5):629–638, 2001.

[7] G. A. W. Murray and J. C. Semple. Transfer of tensile loads from a prosthesis to bone using porous titanium. *Journal of Bone and Joint Surgery-British Volume*, 63(1):138–141, 1981.

[8] C. E. Wen, Y. Yamada, K. Shimojima, Y. Chino, H. Hosokawa, and M. Mabuchi. Novel titanium foam for bone tissue engineering. *Journal of Materials Research*, 17(10):2633–2639, 2002.

[9] K. Asaoka, N. Kuwayama, O. Okuno, and I. Miura. Mechanical-properties and biomechanical compatibility of porous titanium for dental implants. *Journal of Biomedical Materials Research*, 19(6):699–713, 1985.

[10] K. Asaoka and M. Kon. Sintered porous titanium and titanium alloys as advanced biomaterials. *Thermec'2003, Pts 1-5*, 426-4:3079–3084, 2003.

[11] I. H. Oh, N. Nomura, and S. Hanada. Microstructures and mechanical properties of porous titanium compacts prepared by powder sintering. *Materials Transactions*, 43(3):443–446, 2002.

[12] E. Maine and M. F. Ashby. Cost estimation and the viability of metal foams. *Advanced Engineering Materials*, 2(4):205–209, 2000.

[13] D. C. Dunand. Processing of titanium foams. *Advanced Engineering Materials*, 6(6):369–376, 2004.

[14] Y. H. Li, G. B. Rao, L. J. Rong, and Y. Y. Li. The influence of porosity on corrosion characteristics of porous niti alloy in simulated body fluid. *Materials Letters*, 57(2):448–451, 2002.

[15] M. Es-Souni, M. Es-Souni, and H. F. Brandies. On the transformation behaviour, mechanical properties and biocompatibility of two niti-based shape memory alloys: Niti42 and niti42cu7. *Biomaterials*, 22(15):2153–2161, 2001.

[16] F. Miura, A. Ishizaki, Y. Ohura, I. Miura, H. Hamanaka, and K. Watanabe. Studies on mechanical-properties of new superelastic niti wire. *Journal of Dental Research*, 62(4):471–471, 1983.

[17] D. S. Grummon, J. A. Shaw, and A. Gremillet. Low-density open-cell foams in the niti system. *Applied Physics Letters*, 82(16):2727–2729, 2003.

[18] V. I. Itin, V. E. Gyunter, S. A. Shabalovskaya, and R. L. C. Sachdeva. Mechanical-properties and shape-memory of porous nitinol. *Materials Characterization*, 32(3):179–187, 1994.

[19] J. Banhart. Manufacturing routes for metallic foams. *Jom-Journal of the Minerals Metals & Materials Society*, 52(12):22–27, 2000.

[20] M.F. Ashby, A. Evans, N.A. Fleck, L.J. Gibson, J.W. Hutchinson, and H.N.G. Wadley. *Metal Foams-A Design Guide*. Butterworth-Heinemann, Woburn, MA, 2000.

[21] R. Cirincione, R. Anderson, J. Zhou, D. Mumm, and W.O. Soboyejo. An investigation of the effects of sintering duration and powder sizes on the porosity and compression strength of porous ti-6al-4v. In A. Ghosh, T. Sanders, and D. Claar, editors, *Third Global Symposium on Materials Processing and Manufacturing: Processing and Properties of Lightweight Cellular Metals and Structures*, pages 189–198, Seattle, WA, 2002. The Minerals, Metals and Materials Society.

[22] I. H. Oh, N. Nomura, N. Masahashi, and S. Hanada. Mechanical properties of porous titanium compacts prepared by powder sintering. *Scripta Materialia*, 49(12):1197–1202, 2003.

[23] R. Ricceri and P. Matteazzi. Porous nano-crystalline ti-alloy implants. *International Journal of Powder Metallurgy*, 37(4):61–66, 2001.

[24] David J. Sypeck, Phillip A. Parrish, and Haydn N.G. Wadley. Novel hollow powder porous structures. *Mat. Res. Soc. Symp. Proc.*, 521:205–210, 1998.

[25] V. G. Chuprina and I. M. Shalya. Reactions of tini with oxygen. *Powder Metallurgy and Metal Ceramics*, 41(1-2):85–89, 2002.

[26] T. W. Duerig, K.N. Melton, D. Stockel, and C. M. Wayman. *Engineering Aspects of Shape Memory Alloys.* Butterworth-Heinemann Ltd., 1990.

[27] B. Y. Li, L. J. Rong, and Y. Y. Li. Porous niti alloy prepared from elemental powder sintering. *Journal of Materials Research*, 13(10):2847–2851, 1998.

[28] J. S. Kim, J. H. Kang, S. B. Kang, K. S. Yoon, and Y. S. Kwon. Porous tini biomaterial produced by self-propagating high-temperature synthesis: Pore structure, mechanical properties and application. *Materials Science Forum*, 449(4):1097–1100, 2004.

[29] X. M. Zhang, W. H. Yin, and X. C. Wang. Shs high-porosity tini shape memory alloys. *Rare Metal Materials and Engineering*, 29(1):61–63, 2000.

[30] B. Y. Li, L. J. Rong, Y. Y. Li, and V. E. Gjunter. Synthesis of porous ni-ti shape-memory alloys by self-propagating high-temperature synthesis: Reaction mechanism and anisotropy in pore structure. *Acta Materialia*, 48(15):3895–3904, 2000.

[31] Y. H. Li, L. J. Rong, and Y. Y. Li. Porous niti alloy prepared from combustion synthesis. *Progress in Self-Propagating High-Temperature Synthesis*, 217:137–141, 2002.

[32] M.W. Kearns, P.A. Blenkinsop, A.C. Barber, and T.W. Farthing. Manufacture of a novel porous metal. *Metals and Materials*, 3(2):85–88, 1987.

[33] M.W. Kearns, P.A. Blenkinsop, A.C. Barber, and T.W. Farthing. Novel porous titanium. In *Sixth World Conference on Titanium*, pages 667–672, France, 1988.

[34] D. T. Queheillalt, B. W. Choi, D. S. Schwartz, and H. N. G. Wadley. Creep expansion of porous ti-6al-4v sandwich structures. *Metallurgical and Materials Transactions a-Physical Metallurgy and Materials Science*, 31(1):261–273, 2000.

[35] N.G. Davis and D.C. Dunand. Enhancement of solid-state foaming by superplasticity. In *Superplasticity and Superplastic Foaming*, Indianapolis, 2001. ASM-International.

[36] N.G. Davis, J. Teisen, C. Schuh, and D.C. Dunand. Solid-state foaming of titanium by superplastic expansion of argon-filled pores. *Journal of Materials Research*, 16(5):1508–1519, 2001.

[37] J. Teisen. *Superplastic Foaming of CP-Titanium and Ti-6Al-4V*. Diplomierter werkstoffingenieur, Eidgenossische Technische Hochschule Zurich, 1997.

[38] N. G. D. Murray. Solid-state foaming of titanium by hydrogen-induced internal stress superplasticity. *Scripta Materialia*, 49:879–883, 2003.

[39] N. G. D. Murray and D. C. Dunand. Effect of thermal history on the superplastic expansion of argon-filled pores in titanium: Part ii modeling of kinetics. *Acta Materialia*, 52:2279–2291, 2004.

[40] N. G. D. Murray and D. C. Dunand. Effect of initial preform porosity on solid-state foaming of titanium. *Journal of Materials Research*, 21(5):1175–1188, 2006.

[41] D. C. Lagoudas and E. L. Vandygriff. Processing and characterization of niti porous sma by elevated pressure sintering. *Journal of Intelligent Material Systems and Structures*, 13(12):837–850, 2002.

[42] G.W. Greenwood and R.H. Johnson. The deformation of metals under small stresses during phase transformations. *Proceedings of the Royal Society of London*, 283A:403–422, 1965.

[43] C. A. Schuh and D. C. Dunand. Transformation superplasticity of water ice and ice containing sio2 particulates. *Journal of Geophysical Research-Planets*, 107(E11), 2002.

[44] P. Zwigl and D. C. Dunand. Internal-stress plasticity in titanium by cyclic alloying/dealloying with hydrogen. *Journal of Materials Processing Technology*, 117(3):409–417, 2001.

[45] M. Frary, C. Schuh, and D.C. Dunand. Strain ratchetting of titanium upon reversible alloying with hydrogen. *Philosophical Magazine A*, 81(1):197–212, 2001.

[46] T.G. Nieh, J. Wadsworth, and O.D. Sherby. *Superplasticity in Metals and Ceramics*. Cambridge Solid State Science Series. Cambridge University Press, Cambridge, UK, 1997.

[47] T.W. Duering and A.R. Pelton. *Materials properties Handbook: Titanium alloys.* ASM International, The materials information society, 1994.

[48] W. Szkliniarz and G. Smolka. Analysis of volume effects of phase-transformation in titanium-alloys. *Journal of Materials Processing Technology*, 53(1-2):413–422, 1995.

[49] C. Schuh and D.C. Dunand. Non-isothermal transformation-mismatch plasticity: Modeling and experiments on ti-6al-4v. *Acta Materialia*, 49(2):199–210, 2001.

[50] C. Schuh and D.C. Dunand. Transformation superplasticity of ti-6al-4v and ti-6al-4v/10 volcomposites at high applied stresses. *Materials Science Forum*, 357-359:177–182, 2001.

[51] C. Schuh, P. Noel, and D.C. Dunand. Enhanced densification of metal powders by transformation-mismatch plasticity. *Acta Materialia*, 48(8):1639–1653, 2000.

[52] Mark Winter. www.webelements.com. Internet.

[53] Jr. Green, R.E. Introduction to ultrasonic testing. In P. McIntire, editor, *Nondestructive Testing Handbook: Ultrasonic Testing*, volume 7, pages 1–22. American Society for Nondestructive Testing, 2nd edition, 1991.

[54] E. II. Henneke. Fundamental principles of ultrasonic wave propagation. In P. McIntire, editor, *Nondestructive Testing Handbook: Ultrasonic Testing*, volume 7, pages 33–64. American Society for Nondestructive Testing, 1991.

[55] Discussions with members of the achenbach group. 2006.

[56] E. E. Underwood. *Quantitative Stereology.* Addison Wesley, 1970.

[57] H. Shen, S. M. Oppenheimer, D. C. Dunand, and L. C. Brinson. Numerical modeling of pore size and distribution in foamed titanium. *Mechanics of Materials*, 38(8-10):933–944, 2006.

[58] N. G. D. Murray, C. A. Schuh, and D. C. Dunand. Solid-state foaming of titanium by hydrogen-induced internal-stress superplasticity. *Scripta Materialia*, 49(9):879–883, 2003.

[59] N. G. D. Murray and D. C. Dunand. Microstructure evolution during solid-state foaming of titanium. *Composites Science and Technology*, 63(16):2311–2316, 2003.

[60] N. G. D. Murray and D. C. Dunand. Effect of thermal history on the superplastic expansion of argon-filled pores in titanium: Part i kinetics and microstructure. *Acta Materialia*, 52(8):2269–2278, 2004.

[61] N. G. Davis. *Enhancement of solid-state foaming of titanium by transformation superplasticity*. PhD thesis, Northwestern University, 2002.

[62] T.A. Bateman, S.J. Simske, and R.A. Ayers. Porous materials for bone engineering. *Materials Science Forum*, 250:151–182, 1997.

[63] A. Wanner. Elastic modulus measurements of extremely porous ceramic materials by ultrasonic phase spectroscopy. *Materials Science and Engineering*, 248A(1-2):35–43, 1998.

[64] Jr. Donachie, M.J. *Titanium a Technical Guide*. ASM International, Materials Park, OH, 2000.

[65] A. K. Mukherjee. High-temperature-creep mechanism of tini. *Journal of Applied Physics*, 39(5):2201–&, 1968.

[66] H. Kato, T. Yamamoto, S. Hashimoto, and S. Miura. High-temperature plasticity of the beta-phase in nearly-equiatomic nickel-titanium alloys. *Materials Transactions Jim*, 40(4):343–350, 1999.

[67] E. Kobus, K. Neuking, G. Eggeler, and I. Wittkamp. The creep behaviour of a niti-alloy and the effect of creep deformation on it's shape memory properties. *Praktische Metallographie-Practical Metallography*, 39(4):177–186, 2002.

[68] G. Eggeler, J. Khalil-Allafi, K. Neuking, and A. Dlouhy. Creep of binary ni-rich niti shape memory alloys and the influence of pre-creep on martensitic transformations. *Zeitschrift Fur Metallkunde*, 93(7):654–660, 2002.

[69] C. Lexcellent, P. Robinet, J. Bernardini, D. L. Beke, and P. Olier. High temperature creep measurements in equiatomic ni-ti shape memory alloy. *Materialwissenschaft Und Werkstofftechnik*, 36(10):509–512, 2005.

[70] R. R. Hasiguti and K. Iwasaki. Internal friction and related properties of tini intermetallic compound. *Journal of Applied Physics*, 39(5):2182–&, 1968.

[71] J. Cadek. *Creep in Metallic Materials*. Elsevier, Amsterdam, 1988.

[72] S. V. Raj. Tensile creep fracture of polycrystalline near-stoichiometric nial. *Materials Science and Engineering a-Structural Materials Properties Microstructure and Processing*, 381(1-2):154–164, 2004.

[73] S. Frank, S. V. Divinski, U. Sodervall, and C. Herzig. Ni tracer diffusion in the b2-compound nial: Influence of temperature and composition. *Acta Materialia*, 49(8):1399–1411, 2001.

[74] U. Reimann and G. Sauthoff. Effects of deviations from stoichiometry on the deformation behaviour of feal at intermediate temperatures. *Intermetallics*, 7(3-4):437–445, 1999.

[75] S. Suh, M. Dollar, and P. Nash. Creep in mechanically alloyed nial. *Materials Science and Engineering a-Structural Materials Properties Microstructure and Processing*, 193:691–697, 1995.

[76] D. L. Turcotte and G. Schubert. *Geodynamics*. Cambridge, second edition, 2002.

[77] C. Greiner, S. M. Oppenheimer, and D. C. Dunand. High strength, low stiffness, porous niti with superelastic properties. *Acta Biomaterialia*, 1(6):705–716, 2005.

[78] R. Vaidyanathan, M. A. M. Bourke, and D. C. Dunand. Texture, strain, and phase-fraction measurements during mechanical cycling in superelastic niti. *Metallurgical and Materials Transactions a-Physical Metallurgy and Materials Science*, 32A:777–786, 2001.

[79] G.R. Zadno and T.W. Duerig. *Engineering Aspects of Shape Memory Alloys*. London: Butterworth-Heinemann, 1990.

[80] H.J. Frost and M.F. Ashby. *Deformation-Mechanism Maps: The Plasticity and Creep of Metals and Ceramics*. Pergamon Press, Oxford, UK, 1982.

[81] C. Schuh and D. C. Dunand. Transformation superplasticity of ti-6al-4v and ti-6al-4v/tic composites at high stresses. In *Superplasticity in Advanced Materials, Icsam-2000*, volume 357-3 of *Materials Science Forum*, pages 177–182. TRANS TECH PUBLICATIONS LTD, Zurich-Uetikon, 2001.

[82] C. Schuh and D. C. Dunand. An overview of power-law creep in polycrystalline beta-titanium. *Scripta Materialia*, 45(12):1415–1421, 2001.

[83] L. Finnie and W.R. Heller. *Creep of Engineering Materials*. McGraw-Hill Book Company, Inc., New York City, 1959.

[84] David R. Lide, editor. *Handbook of Chemistry and Physics 81st Ed.* CRC, 2000/2001.

[85] Randall M. German. *Powder Metallurgy Science.* Metal powder industries federation, 1984.

[86] M. I. Baskes and W. D. Wilson. Theory of production and depth distribution of helium defect complexes by ion-implantation. *Journal of Nuclear Materials*, 63(1):126–131, 1976.

[87] Milton Ohring. *Materials Science of Thin Films.* Academic Press, 2002.

[88] W. D. Wilson, C. L. Bisson, and M. I. Baskes. Self-trapping of helium in metals. *Physical Review B*, 24(10):5616–5624, 1981.

[89] T. Schober and K. Farrell. Helium bubbles in alpha-ti and ti tritide arising from tritium decay - a tem study. *Journal of Nuclear Materials*, 168(1-2):171–177, 1989.

[90] Laidler and Meiser. *Physical Chemistry.* Houghton Mifflin, 1999.

[91] Bikerman. *Surface Chemistry.* Academic Press Inc., 1958.

[92] H. Jones. The surface energy of solid metals. *Metal Science Journal*, 5(15):15–18, 1971.

[93] D.A. Porter and K.E. Easterling. *Phase Transformations in Metals and Alloys.* Nelson Thornes, 1981.

[94] B. J. Keene. Review of data for the surface tension of pure metals. *International Materials Reviews*, 38 (4):157–191, 1993.

[95] Hai Ming Lu and Qing Jiang. Size-dependent surface tension and tolman's length of droplets. *Langmuir*, 21 (2):779–781, 2004.

[96] D.T. Queheillalt, H.N.G. Wadley, and D.S. Schwartz. Elastic properties of low density core (ldc) ti-6al-4v sandwich cores. *Mat. Res. Soc. Symp. Proc.*, 521:237–242, 1998.

[97] HH Hsu, KH Lin, SJ Lin, and JW Yeh. Electroless copper deposition for ultralarge-scale integration. *Journal of the electrochemical society*, 148(1):C47–C53, 2001.

APPENDIX

Simulation Code

0.1. Analytic java code

```
// ***
// Purpose: This program simulates the pressure vessel equation
//   fdot=3A/2 * f(1-f)/(1-f^1/n)^n * (3P/2n)^n
// Input: all of the constants at the top
//          Everything is in MPa, msec, gram, mm, newton, K
// Output: simulation.data with time, porosity, and pressure cols
//
// Scott Oppenheimer 8/23/04
// ***

import java.io.*;
import java.util.*;

public class PressVesSim {
public static double curfdot=0;
public static double curfdotTSP = 0;
public static double f0=.0059;//initial porosity
public static double f=0; //internal use
public static double P0=100;// HIP pressure
public static double PExt=0; //External pressure 0 for vacuum,
public static double P=0;    //   ~.1 for atmospheric
public static double r0=.005; // in mm
public static double r=0;
public static double Tension = 1.51e-3; // pure Ti in N/mm from Keene et. al.

public static double THIP=1163;//Hip temp
public static double TRun=1303;//Run temp
//******
//Creep equation stuff edot = A(sigma)^n
//******
// public static double A=6.882e-10; //CpTi 903C,n=4.3 (Naomi's stuff)
// public static double n=4.3; //Cp Ti - from Naomi
// public static double ATSP=9.583e-9; //Cp Ti
// public static double nTSP=1; //Cp Ti
```

```
public static double A=5.292e-7; //Ti64 at 1030 C */sec*
public static double n=2.8; //Ti64
// public static double ATSP = 1.058e-5; // 2 min cycles */sec*
// public static double ATSP = 5.290e-6; // 4 min cycles */sec*
// public static double ATSP = 2.645e-6; // 8 min cycles */sec*
public static double ATSP = 1.411e-6; // 15 min cycles */sec*
public static double nTSP = 1.1;

//*****
public static double t=0;
public static double delt=0.0001;

public static double fdot(double curf) {
double tempfdot=0;

double term1=3*A/2;
double term2=( (f-f*f) / Math.pow((1-(Math.pow(f,(1/n)))), n) );
double term3=Math.pow( (3*(P-PExt)/(2*n)), n);

tempfdot = term1*term2*term3;
return(tempfdot);
}

public static double fdotTSP(double curf) {
double tempfdot=0;

double term1=3*ATSP/2;
double term2=f;
double term3= (3*(P-PExt)/(2));

tempfdot = term1*term2*term3;
return(tempfdot);
}

public static double pVirial(double f) {
double tempP=0;

double top=.191e-7*f0*(.5e10*f- //***split for display only***
             .672e10*f*f0-.5e10*f*f+.586e10*f*f*f0+.859e9*f0);
double bot=f*f*(1-2*f0+f0*f0);

tempP=top/bot;
return(tempP);
}
```

```
public static double pTension(double r) {
double press = 2*Tension/r;
return(press);
}

public static double calcklin(double f) {
double tempk = 1;
double startpop = 0.25;
double endpop = 0.375;
if (f < startpop)
tempk=1;
else if (f>endpop)
tempk=0;
else
tempk=(endpop-f)/(endpop-startpop);
return(tempk);
}

  public static void main(String[] args) throws IOException {
FileWriter out = new FileWriter("iso59p5um.data");
out.write("Time Porosity poppedPor Pressure tenPress");
out.write('\r');
out.write('\n');
double realf=f0; // actual porosity knowing that some pop
double k=1; // fraction of pores that have not popped
f=f0;
P=P0;
r=r0;
double V0 = 4/3*3.14159*r0*r0*r0;
double matV = V0*(1-f0);
double poreV = f*matV/(1-f);
double tenPress = pTension(r);
P=P0+tenPress;
out.write(Double.toString(t)+' '+Double.toString(f)+' '+Double.toString(P));
out.write('\r');
out.write('\n');
while (t <= 7.2e5) {
k = calcklin(f);
poreV = f*matV/(1-f);
r = Math.pow(poreV*3/(4*3.14159),0.333333333);
tenPress = pTension(r);
curfdot=fdot(f);//Isothermal
// curfdot = fdotTSP(f);//TSP for Ti64... no creep
```

```
// curfdot = fdot(f) + fdotTSP(f);//TSP and creep
f=f+delt*curfdot;
realf = realf+delt*k*curfdot;
// P=P0*(f0/(1-f0))*(1-f)/f*(TRun/THIP);
P=pVirial(f)-tenPress;
t=t+delt;
if (curfdot*delt < .0001)
delt=2*delt;
if (curfdot*delt > .001)
delt = delt/2;
out.write(Double.toString(t/3.6e3)+' '+ //**SplitForDisplay**
      Double.toString(f*100)+' '+Double.toString(realf*100)+
      ' '+Double.toString(P)+' '+Double.toString(tenPress));
out.write('\r');
out.write('\n');
System.out.println((t/3.6e3)+" "+f+" "+P+" "+tenPress);
}
out.close();
}
}
```

0.2. 2D Abaqus code

```
*Heading
** Job name: 2DAxi1P-2 Model name: Model-1
*Preprint, echo=NO, model=NO, history=NO, contact=NO
**
** PARTS
**
*Part, name=Part-1
*End Part
**
** ASSEMBLY
**
*Assembly, name=Assembly
**
*Instance, name=TheMesh, part=Part-1
**---All nodes, and elements removed to save space---**
*Node, nset=all
*Element, type=CAX4, elset=FlatMat
*Element, type=FAX2, elset=fluid
*Nset, nset=Top
*Nset, nset=Left
*Nset, nset=Axi
*Nset, nset=Bot
```

```
*Nset, nset=Tpt
3
*Nset, nset=Lpt
3
*Nset, nset=PressNode
9999
*Solid Section, elset=FlatMat, material=CPTi
1.,
*FLUID PROPERTY, ELSET=fluid, REFNODE=9999, TYPE=PNEUMATIC, AMBIENT=0
*FLUID DENSITY, PRESSURE=1.013E-1, TEMPERATURE=300.
4.1391e-8,
** Random test of equ to make things work
*Equation
2,
Left, 1, 1.0, Lpt, 1, -1.0
2
Top, 2, 1.0, Tpt, 2, -1.0
*End Instance
*End Assembly
*PHYSICAL CONSTANTS, ABSOLUTE ZERO=0
*INITIAL CONDITIONS, TYPE=FLUID PRESSURE
themesh.9999, 6.542
*INITIAL CONDITIONS, TYPE=TEMPERATURE
themesh.All, 1263
**
** MATERIALS
**
*Material, name=CPTi
*Creep
 7.544e-6, 4.2, 0.
*Elastic
110000., 0.33, 300.
107000., 0.33, 350.
103000., 0.33, 400.
100000., 0.33, 500.
 96000., 0.33, 550.
 90000., 0.33, 600.
 86000., 0.33, 650.
 83000., 0.33, 700.
 79000., 0.33, 750.
 76000., 0.33, 800.
 72000., 0.33, 850.
 69000., 0.33, 900.
 66000., 0.33, 950.
```

```
 62000., 0.33,1000.
 59000., 0.33,1050.
 55000., 0.33,1100.
 53000., 0.33,1150.
 41000., 0.33,1200.
 40000., 0.33,1250.
** ------------------------------------------------------------------
*Boundary
TheMesh.Bot, 2, 2, 0.
TheMesh.Axi, 1, 1, 0.
**
** STEP: Step-1
**
*Step, name=Step-1, nlgeom=YES, inc=1500
*Visco, cetol=0.01
.1, 3.6e5, 1e-8, 3.6e2
**
** OUTPUT REQUESTS
**
*Restart, write, frequency=1
**
** FIELD OUTPUT: F-Output-1
**
*Output, field
*Node Output
u,
*Element Output
S,
**
** HISTORY OUTPUT: H-Output-1
**
**
*Output, history
*Node Output, nset=themesh.PressNode
PCAV, CVOL
*El Print, freq=999999
*Node Print, freq=999999
*End Step
```

0.3. 3D Abaqus code

```
*Heading
** Job name: EighthCube1P-2 Model name: Model-1
*Preprint, echo=NO, model=NO, history=NO, contact=NO
**
```

```
** PARTS
**
*Part, name=Part-1
*End Part
**
** ASSEMBLY
**
*Assembly, name=Assembly
**
*Instance, name=TheMesh, part=Part-1

**----All the nodes, elements are removed to save space----**
*Node, nset=all
*Element, type=C3D8, elset=BulkMat
*Element, type=F3D4, elset=fluid
*Nset, nset=Top
*Nset, nset=Left
*Nset, nset=Right
*Nset, nset=Back
*Nset, nset=Front
*Nset, nset=Bot
*Nset, nset=Lpt
 1,
*Nset, nset=Bpt
 1,
*Nset, nset=Tpt
 1,
*Nset, nset=PressNode
99999,
*Solid Section, elset=BulkMat, material=CPTi
1.,
*FLUID PROPERTY, ELSET=fluid, REFNODE=99999, TYPE=PNEUMATIC, AMBIENT=0
*FLUID DENSITY, PRESSURE=1.013E-1, TEMPERATURE=300.
4.1391e-8,
** Constraint: Back
*Equation
2
Back, 3, 1.
Bpt, 3, -1.
** Constraint: Left
*Equation
2
Left, 1, 1.
Lpt, 1, -1.
```

```
** Constraint: Top
*Equation
2
Top, 2, 1.
Tpt, 2, -1.
*End Instance
*End Assembly
**
*PHYSICAL CONSTANTS, ABSOLUTE ZERO=0
*INITIAL CONDITIONS, TYPE=FLUID PRESSURE
themesh.99999, 13.032
*INITIAL CONDITIONS, TYPE=TEMPERATURE
themesh.all, 990
** MATERIALS
**
*Material, name=CPTi
*Creep
 7.544e-6, 4.2,  0.
*Elastic
110000., 0.33, 300.
107000., 0.33, 350.
103000., 0.33, 400.
100000., 0.33, 500.
 96000., 0.33, 550.
 90000., 0.33, 600.
 86000., 0.33, 650.
 83000., 0.33, 700.
 79000., 0.33, 750.
 76000., 0.33, 800.
 72000., 0.33, 850.
 69000., 0.33, 900.
 66000., 0.33, 950.
 62000., 0.33,1000.
 59000., 0.33,1050.
 55000., 0.33,1100.
 53000., 0.33,1150.
 41000., 0.33,1200.
 40000., 0.33,1250.
** ----- Boundary ---------
*Boundary
TheMesh.Right, 1, 1, 0.
TheMesh.Bot, 2, 2, 0.
TheMesh.Front, 3, 3, 0.
*Step, name=Step-1, nlgeom=YES, inc=500
```

```
*Visco, cetol=0.01
1e-4, 1e11., 1e-8, 1e11.
**
** OUTPUT REQUESTS
**
*Restart, write, frequency=1
**
** FIELD OUTPUT: F-Output-1
**
*Output, field
*Node Output
u,
*Element Output, elset=themesh.BulkMat
S,
**
** HISTORY OUTPUT: H-Output-1
**
*Output, history
*El Print, freq=999999
*Node Print, freq=999999
**
*Output, history
*Node Output, nset=themesh.PressNode
PCAV, CVOL
*El Print, freq=999999
*Node Print, freq=999999
*End Step
```

0.4. Maple Virial Code

Taken from Virial2.mws:

```
Units are abaqus vars (mpa, msec, mm), Virial
Coefficient B for argon are from CRC

> restart:
Virial equations for as HIP state and expanding state
> Vir1:=Po*Vmo/(R*THip)=1+B/Vmo;
> Vir2:=P1*Vmi/(R*TRun)=1+B/Vmi;
Bcc is B in cubic centimeters, and is converted below
> Bcc:=a1*((Tob/Tb)-1)^0+a2*((Tob/Tb)-1)^1+a3*((Tob/Tb)-1)^2;
> a1:=-16:
> a2:=-60:
> a3:=-10:
```

```
> Tob:=298.15:
> Tb:=890:
> B:=Bcc*1000;
Volume changes due to increasing porosity
> volumeDelt:=Vmo/Vmi=fo/(1-fo)*(1-f1)/f1;
> R:=8.314e3:
Solving for volume
> Vmos:=solve(Vir1,Vmo);
> Vmo:=Vmos[1];
> Vmi:=solve(volumeDelt,Vmi);
> Vir1;
> Vir2;
solve for pressure at new volume
> Press:=solve(Vir2,P1);
> NewPress:=simplify(Press);
Figure out initial pressure based on temperature
difference in HIP and creep furnace
> THip:=890+273;
> TRun:=1030+273;
> Po:=100;
> Press;
This is the equation used in the simulation
> simplify(Press);
Put in test values to check
> fo:=.01;
> f1:=.02;
> Press;
```